

**ANALYTICAL AND NUMERICAL
MODELING OF ORGANIC
PHOTOVOLTAIC DEVICES**

ANALYTICAL AND NUMERICAL MODELING OF ORGANIC PHOTOVOLTAIC DEVICES

BY

MOHAMMAD JAHED TAJIK

Master's of Applied Science

Sharif University of Technology

A THESIS
SUBMITTED TO THE SCHOOL OF GRADUATE
STUDIES IN PARTIAL FULFILLMENT OF THE
REQUIREMENTS FOR THE DEGREE OF
MASTER'S OF SCIENCE

McMaster University
Hamilton, Ontario, Canada

© Copyright by Mohammad Jahed Tajik, September 2010

MASTER OF APPLIED SCIENCE (2010)
(Electrical and Computer Engineering)

McMaster University
Hamilton, Ontario

TITLE: Analytical And Numerical Modeling Of Organic
Photovoltaic Devices

AUTHOR: Mohammad Jahed Tajik, Master's of Science
(Sharif University of Technology)

SUPERVISORS: Prof. M. Jamal Deen and Prof. W. Ross Datars
NUMBER OF PAGES: LXXXIX, 89

Abstract

The energy crises, along with the recent global warming trends, demand an immediate cut in the use of fossil fuel. Therefore, renewable sources of energy and especially solar power, have gained tremendous attention from the consumer countries as a possible candidate to replace the carbon-based energy supplies. Among all different types of solar cells, flexibility, cost-effective fabrication processes, combined with low-price materials and most importantly a great potential for improvement make organic solar cells an interesting topic for research. On the other hand, modeling provides a valuable opportunity to study device properties that experimentally are out of reach, expensive or need a long time to measure. These mentioned reasons motivated us to choose modeling of organic solar cells as the subject of our research.

In this research, we tried to provide a complete study of the power generating procedure in organic solar cells by modeling all of the following processes: in-coupling of the photons, absorption of the photons, formation of the excitons, diffusion of the excitons, dissociation of the excitons, transportation of the charges and collection of the charges at the electrodes.

To get a better understanding and also because of basic physical differences, the modeling is divided into two parts: the optical section and the electrical section. Each section is also divided into two separate segments, analytical and numerical analysis.

Using the optical models with different designs to improve the performance of the solar cells, the effect of the layer thickness and two- and three-dimensional light focusing apertures on the intensity of light at the junction of n-type and p-type materials (for bilayer heterojunction organic solar cells) are studied. Results show that for a certain design of the light focusing aperture, a 98% increase in the light absorption in a bilayer heterojunction solar cell can be obtained.

The electrical performance of organic solar cell is also studied by using analytical modeling of exciton diffusion for bilayer heterojunction solar cells and numerical models based on drift-diffusion procedures by using COMSOL multiphysics software for bulk heterojunction solar cells. Based on the mismatch between the calculated results and measurement (counterdiode effect), a tunneling current correction is introduced. Finally, using the tunneling current model, the energy diagram of the organic active layer at the metallic contact is characterised.

In summary, five different models are described in five separate sections, and at the end of each section, results are reported and compared with the literature that prove that the presented models can be used for a new design of organic solar cell characteristics to improve the performance of the device. Also, by introducing the tunneling current to model the counterdiode effect, we have contributed to the literature.

Acknowledgements

I would like to start by his mane the compassionate the merciful that all good things start with his name. Next, I would like to express my sincere gratitude to my supervisors, Prof. M. Jamal Deen and Prof. Ross W. Datars, for giving me the opportunity to work on this subject and for their continuous support and guidance throughout my work. It is indeed an honour to have the opportunity to follow into the footsteps of such a great mentors. I have learned, and I continue to learn so much from them and I hope that my future achievements meet and exceed the expectations of being one of their students.

I would also like to thank my good friends and colleagues in the Microelectronics research Laboratory, Mohammad Reza Dadkhah, Mohammad Waleed Shinwari, Salman Safari, Munir M. El-Desouki, Darek Palubiak, Dr. Ognian Marinov, Dr. Mehdi Kazemeini and especially Mr. Hossein Kassiri Bidhendi and his lovely wife “Maryam” and also Mohammad Hassan Sobhani and his lovely wife “Vista”, Dr. Peyman Setoodeh and everybody else whom I have forgot to mention, for their sincere friendship and supports.

I would like to thank Prof. Xun Li and Dr. Shiva Kumar for taking the time to review my thesis and for being in my committee. I would also like to thank other faculty members at McMaster University, such as Dr. Yaser M. Haddara, Dr. Chin-Hung Chen, Dr. A. Patriciu, Dr. S. Shirani, Also, not forgetting the administrative staff at the ECE department, especially Cheryl Gies, Terry Greenlay, Cosmin Coroiu , Helen Jachna and Steve Spencer.

And of course, I wish to thank my family for their limitless love, support, and encouragement. They will be in my heart for ever and I couldn’t miss them anymore.

List of Contents

ABSTRACT	iii
ACKNOWLEDGEMENTS	iv
LIST OF CONTENTS	v
LIST OF TABLES	x
LIST OF SYMBOLS AND ACRONYMS	xi
CHAPTER 1	1
1. INTRODUCTION.....	1
1.1. PHOTOVOLTAIC OVER THE PASSAGE OF TIME.....	2
1.2. ORGANIC SOLAR CELLS	6
1.2.1. WHY ORGANIC SOLAR CELL?	6
1.2.2. DIFFERENCES BETWEEN ORGANIC AND INORGANIC SOLAR CELLS	7
1.2.3. DIFFERENT TYPES OF ORGANIC SOLAR CELL.....	12
1.3. ORGANIZATION OF THE THESIS.....	15
CHAPTER 2	18
OPTICAL MODELING.....	18
2. OPTICAL MODELING.....	18
2.1. OPTICAL MODEL, ANALYTICAL ANALYSIS	20
2.1.1. TRANSFER MATRIX METHOD (TM).....	20
2.1.1.1. Description of the TM Model.....	20
2.1.1.2. TM Model, Results and Discussion.....	25
2.2. OPTICAL MODEL, NUMERICAL ANALYSIS.....	31
2.2.1. TWO DIMENSIONAL OPTICAL MODEL.....	32
2.2.1.1. Description of the Two Dimensional Model	32
2.2.1.2. Two Dimensional Model, Results and Discussion	36
2.2.2. THREE DIMENSIONAL OPTICAL MODEL	43
2.2.2.1. Description of the Three Dimensional Model	44
2.2.2.2. Three Dimensional Model, Results and Discussion	49
CHAPTER 3	55
3. ELECTRICAL MODELING	55
3.1. ELECTRICAL MODEL, ANALYTICAL ANALYSES.....	57
3.1.1. EXCITON DIFFUSION EQUATION.....	57
3.1.1.1. Description of the Exciton Diffusion Model	57
3.1.1.2. Exciton Diffusion Equation Results and Discussion:	60
3.2. NUMERICAL ANALYSIS, ELECTRICAL MODEL	61
3.2.1. DRIFT-DIFFUSION MODEL.....	62
3.2.1.1. Description of the Drift-Diffusion Model	62
3.2.1.2. Drift-Diffusion Model, Results and Discussion	72
3.3. THE CORRECTION OF ELECTRICAL MODEL USING TUNNELING CURRENT	74

CHAPTER 4.....	83
4. CONCLUSION AND RECOMMENDATION FOR FUTURE WORK.....	83
4.1. CONCLUSION.....	83
4.2. RECOMMENDATION.....	84
REFERENCES.....	86

List of Figures

Figure 1: Forecast of electrical power cost, supply, demand and cost of solar PV electricity for different technologies [3].	2
Figure 2: Best research cell efficiencies from 1975 up to now [4].	5
Figure 3: A reel to reel printing machine in CSIRO institution, Australia [6].	7
Figure 4: Chemical structure of two organic materials that are usually used in DSSCs [16].	8
Figure 5: Chemical structure of some of the famous molecules that are used in OSCs [16].	9
Figure 6: Chemical structures of some of the famous polymers that are used in OSCs [16].	10
Figure 7: Schematic of a inorganic SC (left) and an organic heterojunction SC (right) [18].	11
Figure 8: Schematic of a Schottky-type organic solar cell with its energy band diagram [16].	12
Figure 9: Schematic of a heterojunction organic solar cell with its energy band diagram [16].	13
Figure 10: Principle of exciton dissociation and charge separation in a heterojunction organic solar cell [17].	13
Figure 11: A very rudimentary illustration of bulk heterojunction SC and a bilayer heterojunction SC [18].	14
Figure 12: Schematic of the band structure in bulk heterojunction solar cell [19].	15
Figure13: A planar solar cell in the presence of ambient incident light [20].	20
Figure 14: Demonstration of the layer and interface matrices, the left side is the interface of two layers and the picture on the right side shows the propagation of light inside a layer [16].	21
Figure 15: The active layers interface.	24
Figure 16: Refractive indices as a function of wavelength. For the following material with their references Al refractive indices [34], PEOPT refractive indices [35], PtEOP refractive indices [36], C60 refractive indices [37], ITO refractive indices [38].	26
Figure 17: Pattern of the electromagnetic wave amplitude in the six layer solar cell for $\lambda=470\text{nm}$: (A) shows the pattern for a device for C60 layer thickness equal to 35nm, (B) shows the situation for a 80nm thick C60 layer.	27
Figure 18: Amplitude of the electromagnetic wave at the active area interface for a 60nm thick PEPOT layer and 60 different thicknesses of C60 layer, ranging from 5nm to 300nm. The result is compared the literature [28].	28
Figure 19: The second device configuration (shown below) and the refractive index of the polymer [poly(2,7-(9-(2'-ethylhexyl)-9-hexylfluorene)-alt-5,5-(4',7'-di-2thienyl-2',1',3'-benzothiadiazole))] [31].	29
Figure 20: Light absorption as a function of polymer thickness and C60 thickness. The thickness of Pedot:PSS is 100nm and of ITO 120 nm.	30
Figure 21: Accessing the Harmonic propagation package at the opening window of the COMSOL Multiphysics.	32
Figure 22: Meshing of a planar solar cell via adaptive meshing.	33
Figure 23: Spectrum of the sun (left) [32], Solar spectrum given to COMSOL (right).	34
Figure 24: Subdomain settings for the Harmonic propagation package.	35
Figure 25: Comparison of TM and COMSOL results.	37
Figure 26: Some capping structure and their effect on profile of light on the device.	38

Figure 27: Three dimensional equivalent geometries of the modeled solar cells with three different forms of light trapping structure at the first layer.	38
Figure 28: The intensity of light at the interface of C60 and PEOPT for wavelength between 300nm to 700nm, using triangular arrays at the first layer.	39
Figure 29: The intensity of light at the interface of C60 and PEOPT for wavelength between 300nm to 700nm, using rectangular arrays at the first layer.	40
Figure 30: The intensity of light at the interface of C60 and PEOPT for wavelength between 300nm to 700nm, using semicircular arrays at the first layer.	41
Figure 31: Meshing in COMSOL in two and three dimensions.....	43
Figure 32: Stationary analysis of PDE coefficient form of classical PDEs package.	45
Figure 33: results of a simple three dimensional two layered structure	49
Figure 34: Quantum well and a structure with different refractive indices.	50
Figure 35: Three different light focusing first layer structure: cones, semisphere and blocks	50
Figure 36: Concept of mirror boundary condition with a real source of light in the middle and two imaginary sources of light in its right and left. (imaginary rays are represented by dotted lines).....	51
Figure 37: The intensity of light at the interface of C60 and PEOPT for wavelengths between 325nm and 700nm, using blocks at the first layer.	52
Figure 38: The intensity of light at the interface of C60 and PEOPT for wavelengths between 300nm and 700nm, using cones at the first layer.	52
Figure 39: The intensity of light at the interface of C60 and PEOPT for wavelengths between 300nm and 700nm, using spheres at the first layer.	53
Figure 40: The structure of the solar cell that has been modeled in this section [28].	60
Figure 41: The IPCE (Incident monochromatic Photon to Current collection Efficiency) calculated for the first solar cell compared to the experimental result reported in [28].	61
Figure 42: The band diagram of a bulk heterojunction OSC.	63
Figure 43: Depiction of the Poisson equation package root in the first window of the COMSOL simulator for the one dimensional model.	65
Figure 44: Flowchart of the electrical model.	66
Figure 45: Picture of Steady-state analysis of convection and diffusion at the opening window of COMSOL.....	68
Figure 46: Comparison of my COMSOL simulation and simulation results from [41]. The curves with (+, ., Δ) are the result of my simulation and the ones with (Δ, o, □) at the background are the result of Glatthaar & et. al. [41]. The parameters for both of the cases are demonstrated in Table 9.....	72
Figure 47: Measurement result of I-V curve from [41] (left) compared to the numerical results (right).	73
Figure 48: I-V curve of a diode, a current source and their parallel combination that makes a solar cell.	74
Figure 49: The result of an ordinary solar cell and a parallel diode which will result into a I-V curve of a device similar to a BH-OSC by including the effect of tunneling current (the counterdiode effect).	74
Figure 50: Difference in the band diagram of the solar cell with (Right) and without taking the counterdiode effect into account (Left).	76

Figure 51: Band diagram of a solar cell for different biasing and the direction of the current. Blue arrows stand for the direction of the carrier due to the thermionic emission and the red arrows show the direction of electron tunneling the barrier at the interface (at the left). The experimental result from [41] with separated region in the bias for each one of the four conditions at the left.	77
Figure 52: The difference between the experimental I-V curve and numerical result that are shown in Figure 47	79
Figure 53: Modified tunneling current for three different barrier widths (3nm, 7nm and 10nm) with forty different barrier heights from 1eV to 2eV. The direction of the red arrows in the pictures indicates the increase in the barrier height.....	80
Figure 54: Comparison of calculated I-V corrected by tunneling current (circles) with measurement results reported by Glatthaar <i>et. al.</i> [41] (triangles).	81

List of tables

Table 1: Boundary conditions for the Harmonic propagation package	35
Table 2: Results of the simulation for the focusing apertures normalized to the flat surface results.....	42
Table 3: The Plethora of equations that can be modeled via PDE coefficient form (stationary analysis).....	46
Table 4: Parameters values for generating Helmholtz's equation.	46
Table 5: General boundary conditions, for electromagnetic waves	47
Table 6: Choosing of parameters to generate the needed boundary conditions.	48
Table 7: Results of the simulation for the focusing apertures normalized to the flat surface results.....	54
Table 8: Reported parameters of ITO.	56
Table 9: Parameters that have been used in Figure 46.	70
Table 10: Parameters that are used in Figure 54	81

List of Symbols and Acronyms

Symbols

E_i^+	Transmitted ray
E_i^-	Reflected ray
t	Fresnel complex transmission coefficients
r	Fresnel complex reflection coefficients
M	The transfer matrix
I	The interface matrices
L	The layer's matrix
M'	The prim-system
M''	The bis-system
S	Poynting's vector
B	The magnetic field
$Q(z, \omega)$	Dissipated power at point z and frequency ω
n	Refractive Indices
θ_1	Exciton's exchange efficiency
D	The diffusion constant
β	Inverse of the exciton's diffusion length
θ	Exchange rate
λ	Wavelength
J_{Photo}	Calculated photocurrent
μ_n	Electron's mobility
μ_p	Hole's mobility
G	Generation rate
R	Recombination rate
V_a	Applied voltage
E_G	Bandgap
N_{doping}	Dopants' density

n_i	Intrinsic carrier density
V_t	Thermal voltage
X	Electron affinity
p_{init}	Initial hole concentration at the interfaces of the active layer
n_{init}	Initial electron concentration at the interfaces of the active layer
Φ_m	Work function
V_{LUMO}	Location of the organic layer's LUMO
m_{eff}	Effective mass of the electron inside the metallic electrode
m_{diel}	Effective mass of electron inside the dielectric
t_{diel}	Width of the barrier layer
E_{diel}	Electrical field inside of the barrier
$J_{tunnelling}$	Tunneling current

Acronyms

PV	Photovoltaic
SC	Solar cell
OSC	Organic solar cell
OPV	Organic photovoltaic
CSIRO	Commonwealth Scientific and Industrial Research Organisation
ODSSC	Organic dye-sensitized solar cell
DSSC	Dye-sensitized solar cell
BHJOSC	Bulk heterojunction solar cell
LUMO	Lowest unoccupied molecular orbital
HOMO	Highest occupied molecular orbital
TM	Transfer matrix
IPCE	Incident monochromatic photon to current collection efficiency

FEM	Finite element method
FDTD	Finite-Difference Time-Domain
PFDTBT	Polymer [poly(2,7-(9-(2'-ethylhexyl)-9-hexylfluorene)- alt-5,5-(4',7'-di-2 thienyl-2',1',3'-benzothiadiazole))]
ITO	Indium thin oxide
TE	Transversal electric polarization
AM 1.5	Air mass
ASTM	American Society for Testing and Materials
P3HT	Poly(3-hexylthiophene)
PCBM	[6,6]-phenyl C61-butyric acid methyl ester
1D	One-dimensional
LED	Light emitting diode
FF	Fill Factor

CHAPTER 1

INTRODUCTION

1. INTRODUCTION

Energy crises, global warming, emission of greenhouse gases (water vapor, carbon dioxide, methane, nitrous oxide, *etc.*) are known to be the origin of one of the greatest threats for the future of life on earth. Also, the energy crisis, fragile markets due to the present economic recession as well as the insecure and unstable future of oil and gas production prospect encourage the consumers to search for and develop more stable and possibly less expensive new sources of energy.

Among all of the renewable resources, Photovoltaic (PV) energy seems to be one of the most promising and secure fields that can be adopted by the majority of the countries around the world as a safe and clean substitute for their existing fossil fuel power plants. As the records show [1], PV has the fastest growing rate among renewable energy sources and is actually one of the fastest growing industries among all of the green energies. Most of the growth (40% per year [2]) is in the crystalline silicon technology and the rest is divided between amorphous semiconductor based solar cells (SCs), thin film SCs, dye sensitized SCs, organic solar cells (OSCs) and other SCs. Figure 1 shows the forecast of the demand, supply and the estimated cost of electrical power and photo electrical power for the next ten years in the US energy market. As can be seen in the picture, solar power cannot be a competitive source of power any sooner than 2015 and by the end of 2019 it will be even cheaper than the most pessimistic estimate of the price of energy.

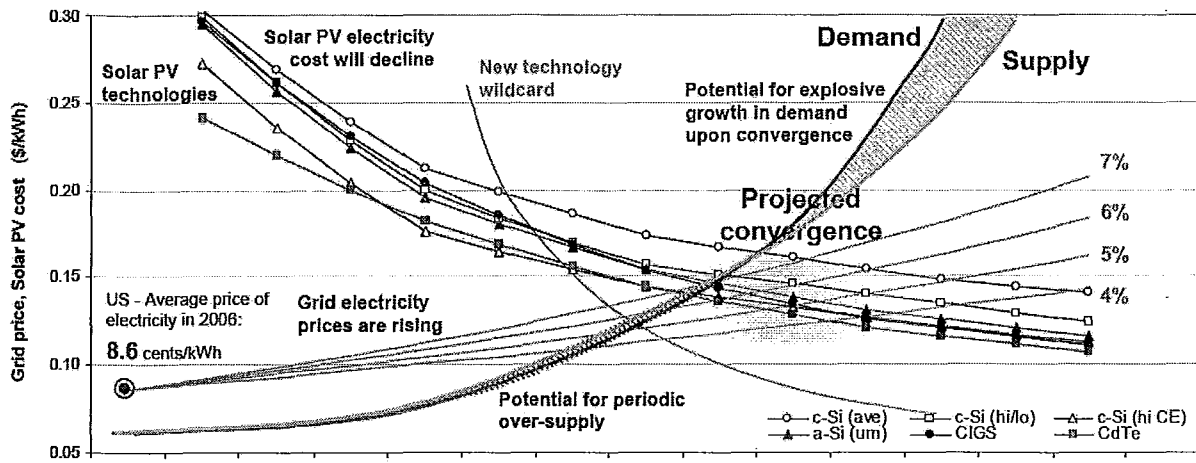


Figure 1: Forecast of electrical power cost, supply, demand and cost of solar PV electricity for different technologies [3].

1.1. PHOTOVOLTAIC OVER THE PASSAGE OF TIME

The first record of the “photovoltaic effect” is related to a French scientist back in 1839. Edmond Becquerel found that “*by the action of a beam of sunlight over two different liquids, chemically interacting and carefully superposed in a glass container, an electric current was developed, as indicated by a very sensitive galvanometer connected with two platinum plates dipping in the two different solutions*” [7]. Then in 1887 Hertz, while working on Maxwell’s electromagnetic theory, found an amazing connection between light and electric discharge that led to a paper entitled “*On an effect of ultraviolet light upon the electric discharge*” [8]. But the true understanding of the PV effect came about later by Albert Einstein’s paper on the photoelectric effect in 1905, which later led to him winning the Nobel Prize in 1921 [9].

Like many other electronic devices, a relatively efficient (6%) silicon based solar cell was discovered at Bell Laboratories in 1953 and like many other scientific innovations, its discovery was accidental. Gerald Pearson, Calvin Fuller and Daryl Chapin discovered photovoltaic while they were trying to improve silicon’s conductivity [10]. Previous photovoltaic research was based on selenium, which has less efficiency and is also more expensive. Therefore, this discovery was a breakthrough for bringing PVs into everyday life. In the next year, Bell Laboratories unveiled their very first solar cell and the next day the New York Times referred to the new invention by the following phrases: “*this may mark the beginning of a new era, leading eventually to the realization of one of mankind’s most cherished dreams—the harnessing of the*

almost limitless energy of the sun for the uses of civilization.'' It sure has an immense effect on the civilization, but it took more than half a century for solar cell to actually become a comparable opponent for the existing carbon based energy supplies.

Later in 1955, the United States' government announced that they had a plan to launch satellites. Because of the impossibility of providing power to the satellite from earth, there was a good opportunity for PVs to show their value. Therefore, suddenly there was an application with a wealthy sponsor to support the research on PVs. Most of the later innovations and development in the solar power field happened in the Cold War years and during the adversary between Soviet Union and United States over control of space, or in a better word in the famous "Space Race".

The next applications for SCs apart from the space application were related to oil rigs in the Gulf of Mexico. For security reasons it is needed for tall structures to have a blinking light on them, but once again the distance to the source of electricity made this the next job of SCs.

Time passed by for solar cell to find its place in history, but it was still far away from the house's roof. To become compatible with other electrical sources and to become a domestic power source, two major improvements had to happen, for the solar cells:

- 1- The size of each unit should shrink (improvement in efficiency)
- 2- The cost of manufacturing should have been reduced to improve the ratio of cost/k-watt

To improve the efficiency, the quality of the materials had to be improved (better crystal quality), fabrication methods had to be reformed and new structures had to be introduced (*i.e.* two and three stag solar cells). However, all of the mentioned changes would increase the cost of manufacturing. Therefore, at the same time, researchers were trying to make the total cost of the solar cells decrease by finding cheaper types of material (*i.e.* amorphous semiconductors, organic material and so on) or cheaper structures with lower manufacturing cost (*i.e.* planar SCs with printing technique as their fabrication method [5]).

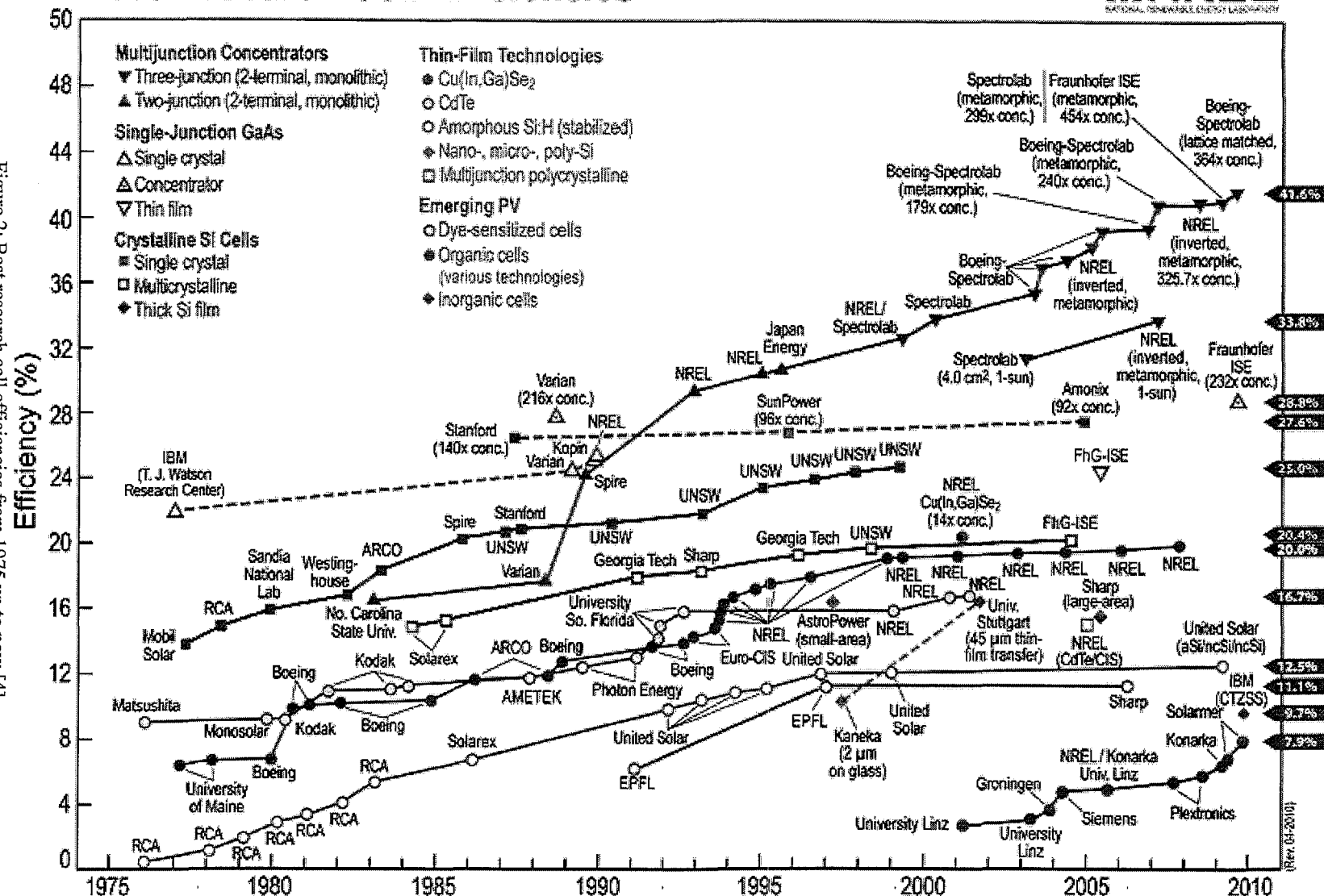
Figure 2 shows the history of PV's evolution since the beginning of the industrial production. In this picture, major improvements in the efficiencies of each type of SCs (Crystalline, Multiple-junction, Thin film, single junction and Organic photovoltaic) are shown by mentioning the time

and the name of the research group. As shown in the picture, the highest efficiency is for three-junction solar cells (from Boeing-Spectrolab R&D) with 41.6%.

For organic photovoltaic, it was in early years of 60's that researchers noticed the potential of organic materials in imaging systems [11]. During the next couple of years, investigation in the field of organic photovoltaic (or OPV) continued but efficiencies were really low. As an example, 0.001% efficiency reported by C. W. Tang *et.al.* in 1975 was the state of the art. In 1977 Heeger, MacDiarmid and Shirakawa discovered that by introducing doping such as halogen chlorine, bromine or iodine, the conductivity of the conjugated polymer can be increased by the range of eleven order of magnitude [12]. Later on, in 2000, they received a Nobel Prize in Chemistry because of their great works on conductivity and superconductivity in organic materials [13]. The first OSC with efficiency over 1% was reported in 1986 once again by C. W. Tang [14].

The latest development is related to Solarmer Energy Inc. On 27 July 2010, Forbes.com reported that Solarmer broke the 8% wall and reported an organic solar cell with 8.13% efficiency [15]. As Forbes reported, the president of the Solarmer Company referred to the 8% efficiency wall as the "psychological barrier for the OPV industry". Forbes predicted that by this discovery, the cost of energy production for OPVs will go down to 12-15 cents/kWh.

Best Research-Cell Efficiencies



1.2. ORGANIC SOLAR CELLS

1.2.1. WHY ORGANIC SOLAR CELL?

Compared to conventional solar cells, organic solar cells are relatively cheaper to produce. The obvious reason is that the type of materials used in organic solar cells are less expensive, needs less preparation and is more abundant than conventional crystalline solar cells.

Organic materials are polymers and oligomers as well as organic molecules very similar to the plastic bags that we use every day. Similar to plastic bag, they are products of oil. Therefore, in the case of mass production, their price can be really low.

On the other hand, unlike conventional solar cells that are based on crystalline semiconductors, which need high purity in material and therefore, costly preparation and purification processes, organic materials that are used in organic solar cells are easy to process with very cost effective processes.

Because of malleability of organic materials, organic solar cells are capable of getting into any shape during the process of fabrication and the final production can also be a flexible sheet that can be wrapped and packed for example into a soldier's backpack and in the case of necessity for recharging an electrical equipment be unwrapped and used.

Moreover, the fabrication methods for organic solar cells are much cheaper than conventional solar cells. As an example they do not need a clean room facility for their fabrication procedure. The deposition processes in the case of molecular and polymeric thin film are spin-coating, screen printing, spray coating and ink jet coating, reel to reel printing [5], which are low cost, simple and they are also suitable for large area and ultra thin layer fabrication, which in the case of mass production make the whole process of fabrication extremely cost effective.

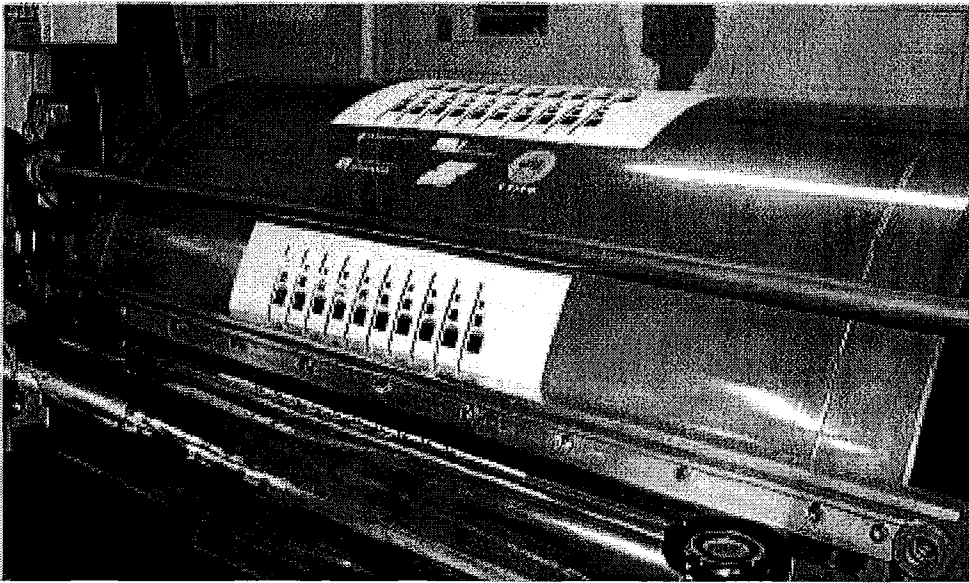


Figure 3: A reel to reel printing machine in CSIRO institution, Australia [6]

Figure 3 shows a reel to reel printing machine in Commonwealth Scientific and Industrial Research Organisation (CSIRO). This machine uses the same technique that is used in printing news papers. The machine in Figure 3 is capable of printing 200 meters of organic solar cells per minute in the full speed condition. This is equal to printing 100km of solar cells per day. Assuming that the efficiency of the printed solar cell is close to 10%, continuous printing at full speed for five months will provide enough solar cells to generate 1 G watt electrical power plant.

All of the mentioned reasons above plus this fact that their efficiency is still really low, compared to the conventional solar cells, make the organic solar cell a prospective and interesting research topic.

1.2.2. DIFFERENCES BETWEEN ORGANIC AND INORGANIC SOLAR CELLS

The first difference between organic and inorganic SCs is due to the materials that are used to make them. As it can be deduced from the names, in the inorganic SCs, inorganic materials such as crystalline materials (mostly silicon-based) are used. These SCs have good electrical properties, which are mostly because of their crystalline structure. On the other hand, they have a relatively low light absorption, which can be corrected using a multistage structure.

Once again as the name implies, organic SCs are made of organic materials. Organic SCs based on their materials can be divided to the following categories:

- 1- Dye-sensitized OSCs
- 2- Molecular SCs
- 3- Polymeric SCs
- 4- Mixed SCs

Organic dye-sensitized SCs (ODSSC) are made of a liquid electrolyte that transports generated carriers created by organic molecules inside the electrolyte. This type of OSC is very cheap but at the same time its external efficiency is really low (<1%). Figure 4 shows the chemical structure of two organic materials that are usually used in DSSCs.

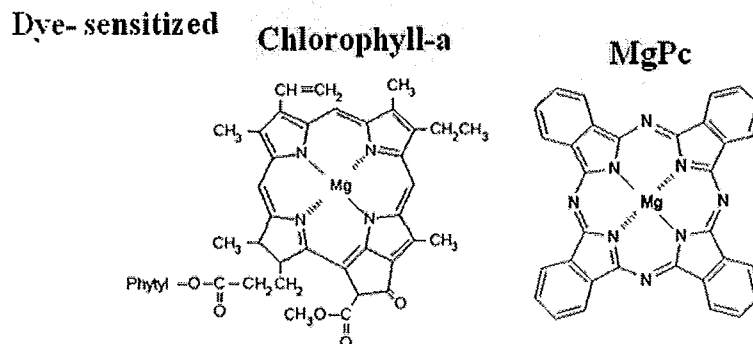


Figure 4: Chemical structure of two organic materials that are usually used in DSSCs [16].

Both molecular and polymeric SCs are made of non-crystalline amorphous molecules. The terms “molecular” and “polymeric” refer to the molecular weight. Usually, macro-molecules with molecular weight larger than 10,000amu are called polymers. The term “oligomers” is related to molecules lighter than that and for the very small molecules the term “molecule” is used [17].

Molecular and polymeric materials are usually used together to increase both absorption and electrical conductivity. The molecular section has better optical power absorption while polymers have a better electrical conductivity. Therefore, optical power is absorbed by the molecular section and electrical conductivity is provided by a network made of polymer strings.

Figure 5 and Figure 6 respectively show the chemical structures of some molecular and polymeric materials that are used in fabrication of OSCs with their abbreviated names.

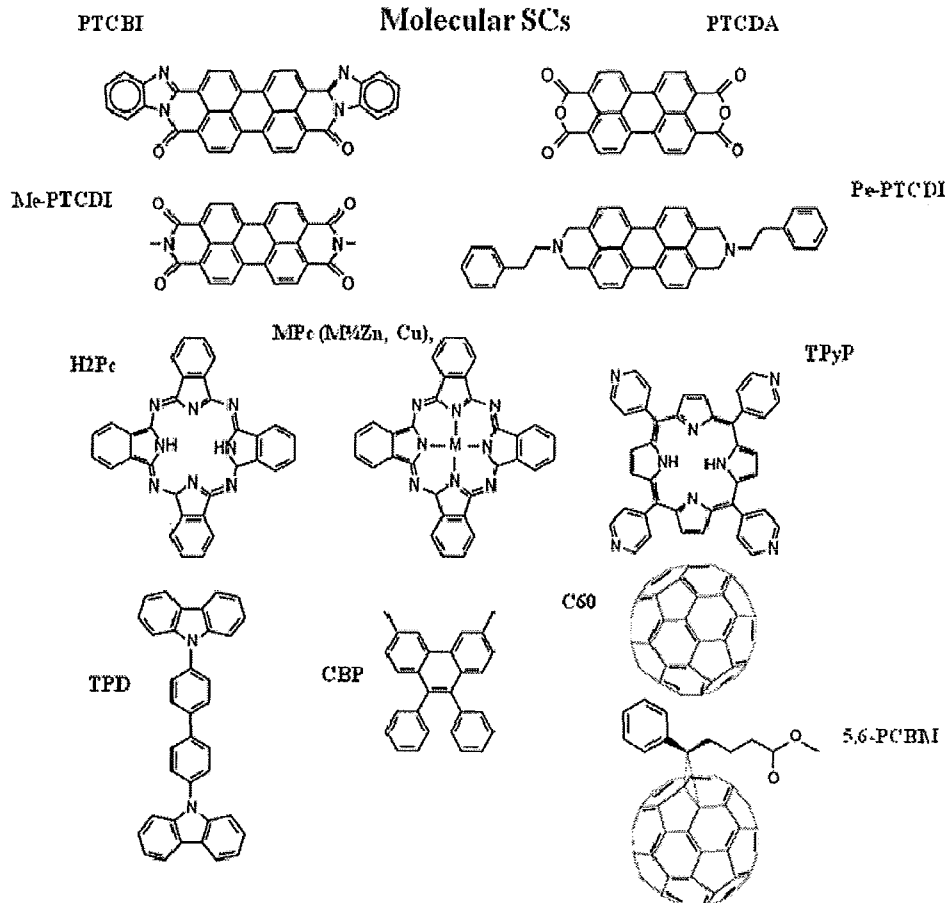


Figure 5: Chemical structure of some of the famous molecules that are used in OSCs [16]

Another major difference between conventional and organic SCs is due to the mechanism of charge generation and charge transport. In inorganic SCs, after the absorption of a photon, an electron is excited and an electron-hole pair is generated. Then, because of the built-in electrical field, which is due to the difference in anode and cathode work functions, inside the device they are separated from each other. After separation, because of electrostatic charges that each one of them has, they would be drifted towards anode (for electrons) and cathode (for holes). Figure 7 shows a schematic depiction of a conventional SC that mimics the mechanism of charge generation inside a conventional SC. In the case of organic SCs, electron and holes are tightly bound together and make an exciton (Figure 7).

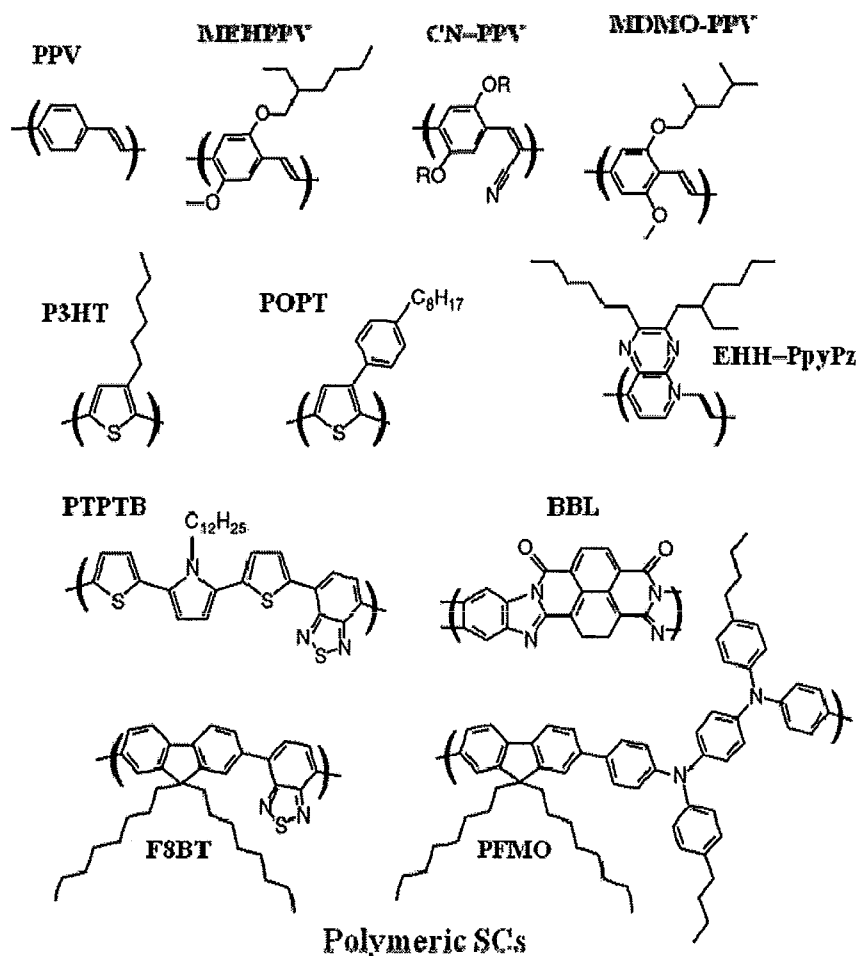


Figure 6: Chemical structures of some of the famous polymers that are used in OSCs [16]

The binding energy of organics' excitons and their separation energy is a little different than conventional semiconductor excitons. In both of them coulomb attraction between the electron and hole exist and to break the exciton that barrier of energy should be overcome. However, in the case of organic excitons, the situation is a little different. An exciton in an organic segment (a molecule or a string of a polymer) is equal to the excited state of that segment. It is one of the stable states in the discontinuous energy states of that segment and is related to a stable orbital form of electron cloud of that segment. Therefore, breaking an organic exciton is equivalent to a change in a stable state, which requires an amount of energy that is more than the coulomb attraction.

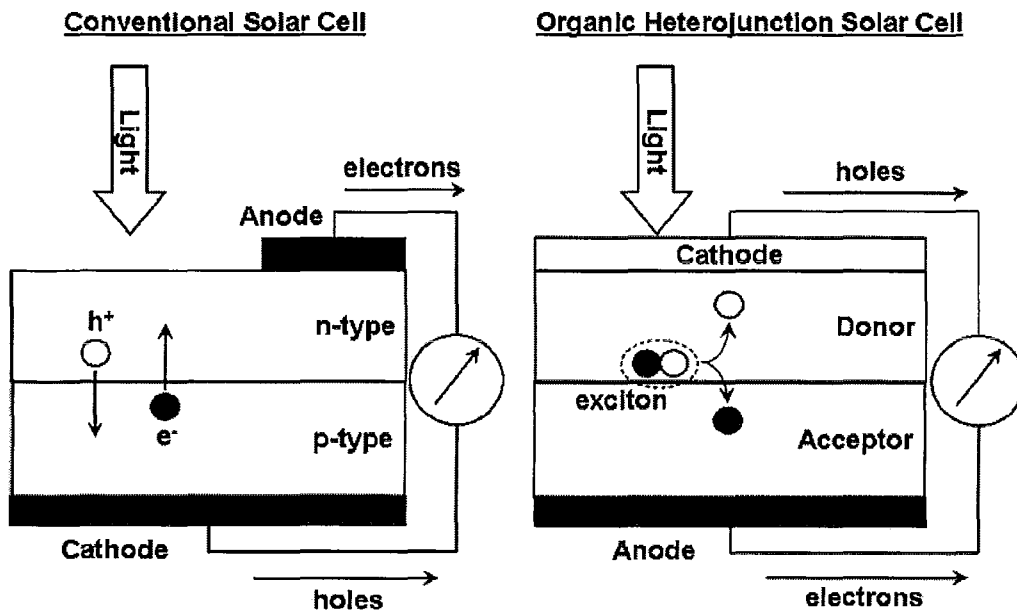


Figure 7: Schematic of a inorganic SC (left) and an organic heterojunction SC (right) [18]

On the other hand, unlike conventional semiconductors, there are no crystalline structures in organic materials for the separated charges. Single charges in an organic material are bound to a site and are called a polarons. Consequently, before the separation of charges, there should be a second molecule to carry one of the separated charges. This means that there is more energy that is required to break an exciton and therefore, one more phenomena other than the coulomb attraction to bind opposite charges inside an organic segment to make an exciton.

Since an exciton has both types of charges, it cannot be attracted towards any of the electrodes due to the internal build-in electrical field. However, like many other particles, they can diffuse. If an exciton gets to a conductive layer, electron and hole will be recombined at the surface of that conductive layer and as a result, no electrical power will be generated. Consequently, electrons and holes should be separated before that. To generate an electron-hole pair out of an exciton, one of the following conditions should exist:

- 1- High electrical fields
- 2- Interface of two materials with two different energy bands

Because of the low build-in potential in organic solar cells, using heterojunctions, the second condition is used in the structure of the OSCs to break up the excitons. In the next section, different structures of OSCs are discussed.

1.2.3. DIFFERENT TYPES OF ORGANIC SOLAR CELL

Similar to conventional solar cells, there is a type of organic solar cell with an active layer made of one of the n-type or p-type materials (mostly p-type). The name of this kind of organic solar cell is Schottky OSC because of a Schottky connection in one side of the device. Figure 8 shows a schematic structure and band diagram of a Schottky-type SC.

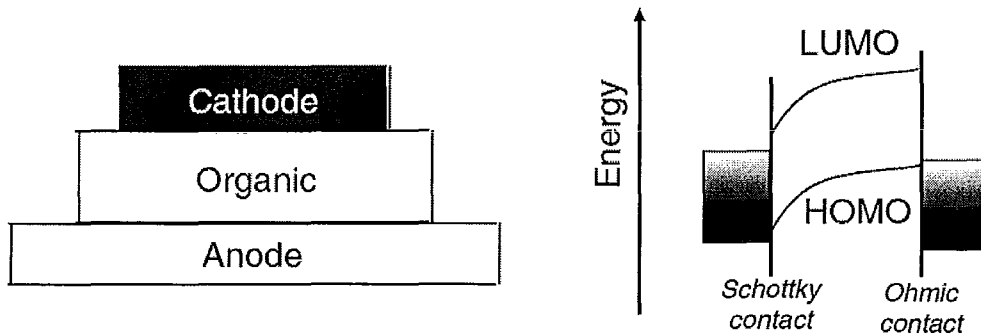


Figure 8: Schematic of a Schottky-type organic solar cell with its energy band diagram [16]

Since there is no interface in the design of this device, most of the generated excitons are going to be dissociated at the interfaces or inside the active layer without generating any power. Therefore, the next structure is proposed with two types of organic material as its active layer. This structure, due to the use of different layers, is named heterojunction organic solar cell (or bilayer heterojunction OSC). Figure 9 shows the schematic and band diagram of a heterojunction SC.

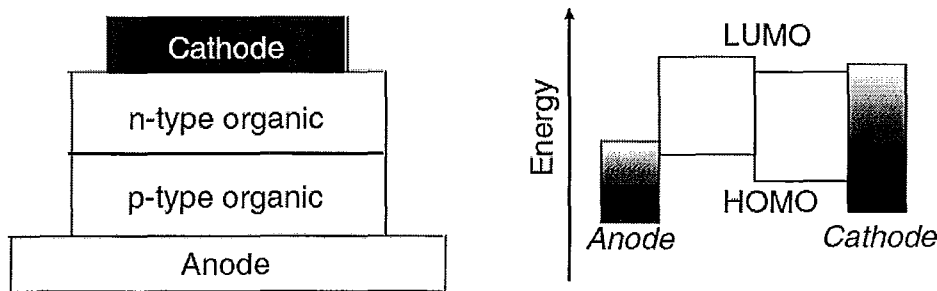


Figure 9: Schematic of a heterojunction organic solar cell with its energy band diagram [16]

In this structure, by incoming light from a transparent anode an exciton is generated and it will diffuse all the way (7-10 nm) to the interface of donor and acceptor layers where they are separated into a hole and an electron. Later, these generated charges will reach the electrodes by means of drift and diffusion, and will create electrical current. All of the explained processes are depicted in Figure 10.

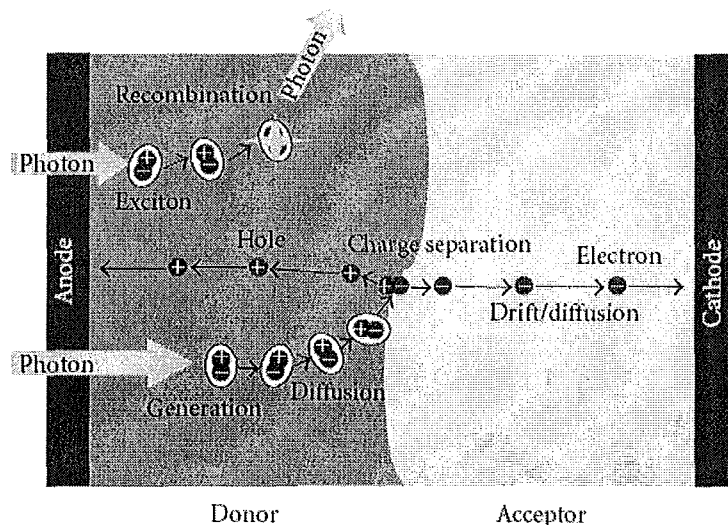


Figure 10: Principle of exciton dissociation and charge separation in a heterojunction organic solar cell [17]

As mentioned before, because of the exciton's short diffusion length, most of the excitons cannot make it all the way to the interface and (as shown in Figure 10) a recombination will happen. Therefore, the total amount of electrical power will be reduced and the efficiency will decrease. As a result, one way of increasing the efficiency is to fabricate very thin active layers but this may result in low optical power absorption.

One idea is to mix donor and acceptor molecules to increase the interface areas, so that excitons before recombination get the chance of being separated at an interface. This type of OSC is called bulk heterojunction OSC (BHJOSC). Figure 11 shows a very rudimentary comparison between bilayer heterojunction and bulk heterojunction structures. In this picture the black color represents acceptor layer and the white color stands for donor layer.

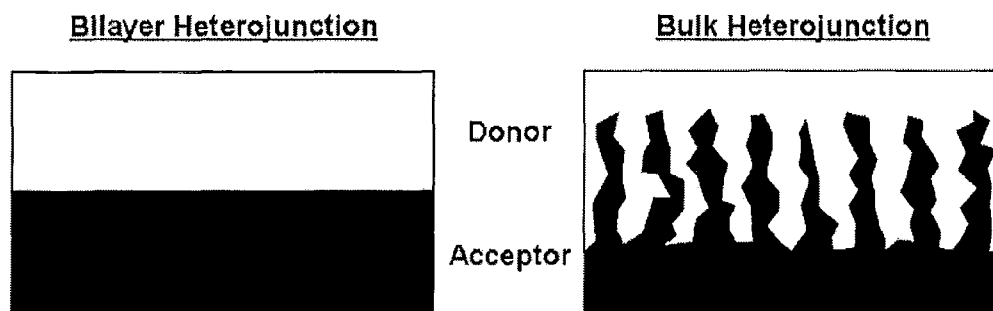


Figure 11: A very rudimentary illustration of bulk heterojunction SC and a bilayer heterojunction SC [18].

As it can be seen in the picture, in bulk heterojunction SCs these two materials are mixed together. Therefore, in bulk heterojunction SCs, the interface of the donor and acceptor layers is increased and as a result the number of excitons that get separated into electrons and holes is increased, which will lead to an increase in the ratio of generated carriers over the number of absorbed photons. This ratio is called the quantum efficiency and is one of the characteristic figures-of-merit that are used to evaluate the performance of a solar cell.

In bulk heterojunction OSCs, after the dissociation of the excitons, electrons will go to the lowest unoccupied molecular orbital (LUMO) of the acceptor, that is similar to the conduction band in conventional semiconductors, and holes will go to the highest occupied molecular orbital (HOMO) of donor, which is similar to the valence band of conventional semiconductors. In this case, the blend of donor and acceptor materials acts like a new organic material with a shorter band gap that is composed of acceptor's LUMO and donor's HOMO.

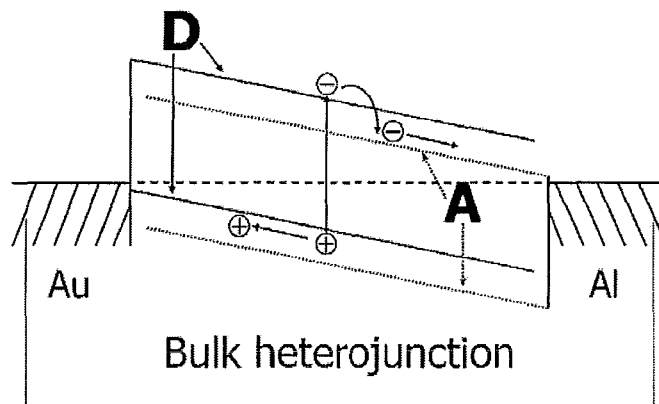


Figure 12: Schematic of the band structure in bulk heterojunction solar cell [19].

In this thesis, both the bilayer heterojunction and the bulk heterojunction are modeled. The next section describes the organization of the thesis, order of subjects and the reasoning behind them.

1.3. ORGANIZATION OF THE THESIS

The goal of modeling organic solar cells is to find new device designs, to enhance the understanding of the power generation in these devices and to improve the performance of these devices based on the understanding. Modeling provides an opportunity to examine properties that are out of reach or too expensive to measure. On the other hand, modeling is much faster and makes it possible to study numerous device structures and configurations. in a very short period of time, which can provide valuable information. These abilities are beyond what an experiment can do. By taking the device as a light-in current-out device the performance of solar cells can be divided into the following processes:

- 1- In-coupling of the photons
- 2- Absorption of the photons
- 3- Formation of the excitons
- 4- Diffusion of the excitons
- 5- Dissociation of the excitons
- 6- Transportation of the charges

7- Collection of the charges at the electrodes

In this research, all of the seven processes are studied. The rest of the thesis is organized as follows.

The thesis body is divided into two chapters:

- Optical model (chapter 2)
- Electrical model (chapter 3)

Each one of the mentioned chapters has two sections:

- Analytical analysis
- Numerical analysis

Each section consists of one or two models. Regardless of the type of the models, each model has two sections:

- Description of the model
- Results and discussion

The thesis starts with optical chapter (chapter 2). The analytical analysis of the optical properties of the organic solar cell is the first section of this chapter, which contains one model, Transfer Matrix (TM) model. The reason for studying TM model is to create a reliable mean to test the validity of the generated numerical models.

The next section is numerical analyses of the optical properties. This section's ultimate goal is to study the effect of focusing aperture at the top layer of an organic solar cell on the performance of the device. This section consists of two numerical models:

- Two dimensional optical model
- Three dimensional optical model

The two dimensional model uses the "Harmonic Propagation" package whereas the three dimensional model uses "PDE, coefficient form, Stationary analysis" package. The main reason

for choosing the second package to model the three dimensional optical problem is the low computational cost of this package compared to the Harmonic propagation package.

In the result and discussion part of the two dimensional model, after examining the validity of the model by comparison with TM results, the effect of 18 different two dimensional light focusing apertures or one dimensional photonic crystals is studied. The same pattern is repeated for the three dimensional model with one difference that, this time the result of 14 different three dimensional light focusing apertures (two dimensional photonic crystals) is studied. This concludes, chapter two.

The next chapter (chapter 3) is related to the electrical modeling of organic solar cells. The first section is related to analytical analysis of electrical modeling of bilayer heterojunction organic solar cells. The model is based on the diffusion of excitons. The result is presented in the form of “incident monochromatic photon to current collection efficiency” or shortly IPCE. Later, the calculated IPCE is compared to the measurements and a good agreement is observed.

The second section of chapter 3 is about numerical modeling of electrical properties of a bulk heterojunction solar cell. A self consistent loop of Poisson’s equation and two separate continuity equations for electrons and holes, and the multiphysical COMSOL model to solve them is described. The results of this section are followed by a comparison of the obtained numerical results with numerical results reported in the literature. Later, numerical results and measurement results are also compared and some dissimilarities are observed.

To address the observed dissimilarity issue, a theory based on tunneling current at the interface of metallic electrode is developed. Based on that, the best fit to the I-V curve of experimental and numerical results is found using trial and error and the optimal values of the parameters of the tunneling current are determined. Finally, the last chapter (chapter 4) is the conclusion and suggestions for future works.

CHAPTER 2

OPTICAL MODELING

2. OPTICAL MODELING

This chapter is dedicated to optical modeling of organic solar cell. The goal is to find the magnitude of electrical field inside a planar organic solar cell as a function of position and incoming light's frequency. Using the calculated electrical field's magnitude, the intensity of light is calculated as a function of position and frequency of the incoming beam. Then, the amount of absorbed power and based on that the total number of generated excitons is calculated.

Therefore, outputs of optical simulation are:

- 1- Profile of light intensity as a function of position and frequency
- 2- Amount of absorbed power as a function of position and frequency
- 3- Total number of generated excitons as a function of position

The following, models that have been used to calculate these results are described. This chapter is divided to two sections:

- 1- Analytical model
- 2- Numerical model

For the analytical section, the transfer matrix method (or shortly TM) was used. The TM method is a straight forward method that can calculate the distribution of electromagnetic waves in a one dimensional structure. It can be successfully used for the optical simulation of multilayered thin film solar cells. However, due to its analytical nature, it is difficult to develop a TM-based

optical simulator for complicate geometries, for an instance folded structures or planar solar cells with focusing structures.

For the numerical section, we used “COMSOL Multiphysics”. This software benefits from Finite Element Method’s (or shortly FEM) excellent compatibility with unorthodox boundary conditions. It is also equipped with advanced abilities in modeling capabilities such as adaptive meshing and controllable damping parameters. Moreover, it is possible to link COMSOL Multiphysics to other programming platforms such as MATLAB, in order to perform joint simulations. These make COMSOL Multiphysics a proper choice.

Prior to finalizing the decisions on using COMSOL as the numerical modeling environment, a few other packages were also examined. Among them were Finite-Difference Time-Domain (FDTD) Solutions (by Lumerical Solutions, Inc.) and OptiFDTD (by OptiWave system Inc.), that have a purchased license at McMaster University. Most of them use the FDTD method as their modeling strategy which makes them a good candidate for a time dependent or transient analyses, while we were interested in harmonic analyses.

On the other hand, incomplete libraries that lack organic material coefficients made it necessary to create new libraries that needed precise information about the development of the software. Obtaining this knowledge about each one of the softwares to decide which one is changeable was simply time consuming and it questioned the whole Idea of using software in the first place.

Moreover, finite difference is not the best numerical method to model problems with peculiar geometry. All of the mentioned advantages for COMSOL plus the ability of modeling the electrical section of the simulation in COMSOL at the same time and linking two sections of the simulation (electrical and optical), made the software COMSOL multiphysics the ultimate choice for this research.

The optical numerical model is also divided into two separate sections:

- 1- Two dimensional model
- 2- Three dimensional model

For the two dimensional section, the “Harmonic propagation” package was used. But because of the high computational cost of Harmonic propagation package for the three dimensional model, the three dimensional simulation was performed by using a less complicated package: “PDE coefficient form, stationary analysis”.

2.1. OPTICAL MODEL, ANALYTICAL ANALYSIS

2.1.1. TRANSFER MATRIX METHOD (TM)

Transfer Matrix approach (TM) is one dimensional modeling of light propagation through the different layers of a planar solar cell, which can be attributed as a one dimensional layered stack of different materials (Figure13).

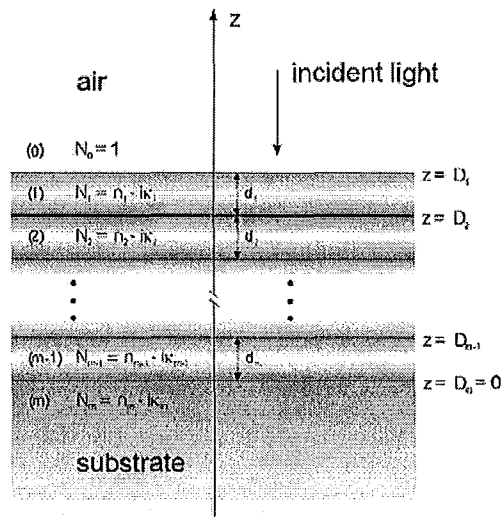


Figure13: A planar solar cell in the presence of ambient incident light [20]

2.1.1.1. Description of the TM Model

In this method, the solar cell is modeled by using two types of matrices:

- 1- Layer's matrix, which models the effect of each layer's material on transporting beam of light.

- 2- Interface's matrices, which model the phenomena of transportation and reflection of incoming beam of light at the interface of two adjoining layers.

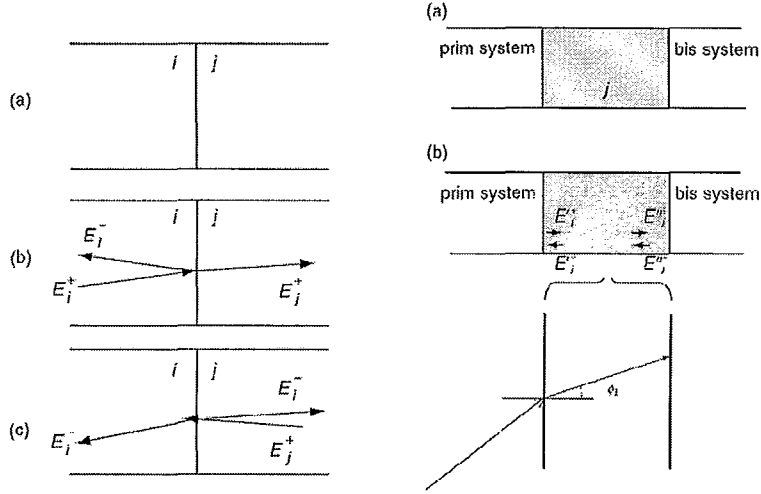


Figure 14: Demonstration of the layer and interface matrices, the left side is the interface of two layers and the picture on the right side shows the propagation of light inside a layer [16]

The picture *a* at the left side of Figure 14 shows the interface of two layers. In the picture below that, which is marked by word *b*, the traveling beam of light from layer *i* into layer *j* is shown by E_i^+ . At the interface of two layers, this beam is divided into two elements:

- Transported ray, which is shown by E_j^+ .
- Reflected ray, which is shown by E_i^- .

The relationship between these elements and the incoming beam of light is defined by the Fresnel complex transmission and reflection coefficients as:

$$t = \frac{E_1^+}{E_0^+} \quad \text{Equation 1}$$

$$r = \frac{E_0^-}{E_0^+} \quad \text{Equation 2}$$

The electrical element of the electromagnetic field E for a single wavelength and stationary source in a passive environment creates a standing wave. Let E^+ and E^- be forward and reverse components of standing wave E . For one dimensional light propagation, we have:

$$E(z) = E^+(z) + E^-(z) \quad \text{Equation 3}$$

The transfer matrix is a matrix that defines the amplitude of electromagnetic wave at any point based on the amplitude of the incoming beam:

$$\begin{pmatrix} E^+ \\ E^- \end{pmatrix}_{z_1} = M \begin{pmatrix} E^+ \\ E^- \end{pmatrix}_{z_2} \quad \text{Equation 4}$$

In essence, the transfer matrix itself represents the response of the system (*i. e.* a stack of organic material) to the incoming beam of light. As mentioned above, the transfer matrix has two constructing elements; the layer and interface matrices. Having these matrices, the transfer matrix can be defined as:

$$M = I_{01}L_1I_{12}L_2\cdots L_mI_{m,m+1} = \left(\prod_{v=1}^m I_{v-1,v}L_v \right) I_{m,m+1} \quad \text{Equation 5}$$

where matrix I (the interface matrices) is defined below:

$$I_{ij} = \frac{1}{t_{ij}} \begin{pmatrix} 1 & r_{ij} \\ r_{ij} & 1 \end{pmatrix} \quad \text{Equation 6}$$

t_{ij} and r_{ij} are respectively the Fresnel's complex coefficient of refraction and transmission between layer i_{th} and j_{th} , which were defined in Equation 1 and Equation 2. The right picture in Figure 14 shows the passage of light inside of layer j . The effect of this layer on the beam of light can be defined as an exponential function:

$$e^{-i\frac{2\pi d}{\lambda}n_j\cos\phi_1} \quad \text{Equation 7}$$

where d denotes the layers thickness, ϕ is the angel of refraction, n is the index of refraction and λ is the wavelength of the incoming light. Therefore, by passing through layer j , the electrical

component of the electromagnetic field has a phase change equal to the argument of the exponential function in Equation 7 which depends on the refractive index, wavelength and width of layer j . Having all of the variables, layer's matrix is described as:

$$L_j = \begin{pmatrix} e^{-i\frac{2\pi d}{\lambda}n_j \cos \phi_1} & 0 \\ 0 & e^{i\frac{2\pi d}{\lambda}n_j \cos \phi_1} \end{pmatrix} \quad \text{Equation 8}$$

As Sun *et.al.* noted in [16], the transfer matrix can be divided into bis-system and prim-system as:

$$M = M'_j L_j M''_j \quad \text{Equation 9}$$

M' (prim-system) and M'' (bis-system) are defined as:

$$M'_j = \left(\prod_{v=1}^{j-1} I_{v-1,v} L_v \right) I_{j-1,j} \quad \text{Equation 10}$$

$$M''_j = \left(\prod_{v=j+1}^m I_{v-1,v} L_v \right) I_{m,m+1} \quad \text{Equation 11}$$

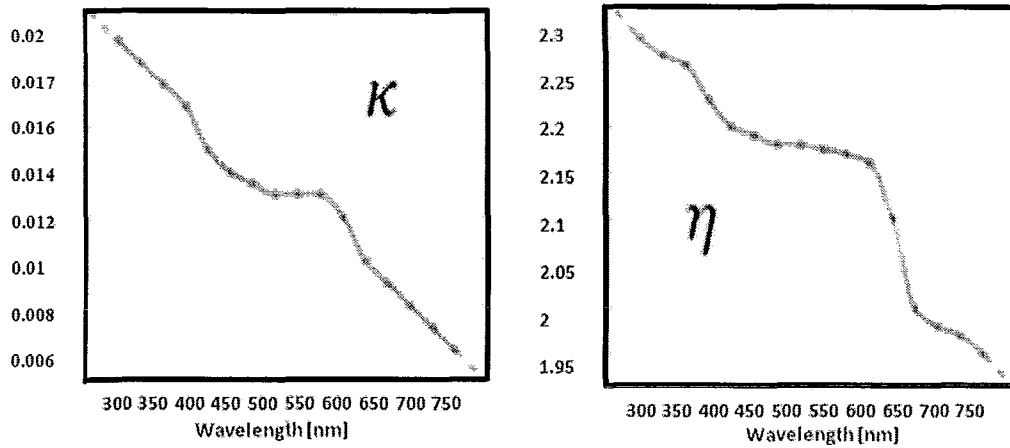
The electrical field in any layer of the device can be described by bis-system and prim-system matrices, respectively for upstream and downstream systems, as:

$$\begin{pmatrix} E_0^+ \\ E_0^- \end{pmatrix} = \begin{pmatrix} M'_{j,11} & M'_{j,12} \\ M'_{j,21} & M'_{j,22} \end{pmatrix} \begin{pmatrix} E_j^+ \\ E_j^- \end{pmatrix} \quad \text{Equation 12}$$

In Equation 12, if the transparent end of the solar cell is identified by layer $m+1$, the electrical field in layer j based on the sun radiation, which is shown by E_{m+1} , will become:

$$\begin{pmatrix} E_j^{''+} \\ E_j^{''-} \end{pmatrix} = \begin{pmatrix} M''_{j,11} & M''_{j,12} \\ M''_{j,21} & M''_{j,22} \end{pmatrix} \begin{pmatrix} E_{m+1}^+ \\ 0 \end{pmatrix} \quad \text{Equation 13}$$

ITO refractive index



PEOPT refractive index

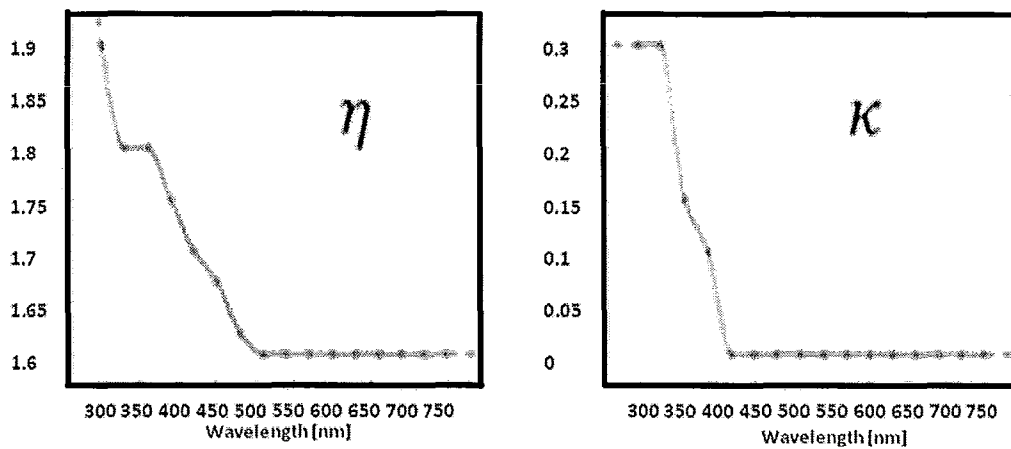


Figure 16: Refractive indices as a function of wavelength. For the following material with their references Al refractive indices [34], PEOPT refractive indices [35], PtEOP refractive indices [36], C60 refractive indices [37], ITO refractive indices [38]

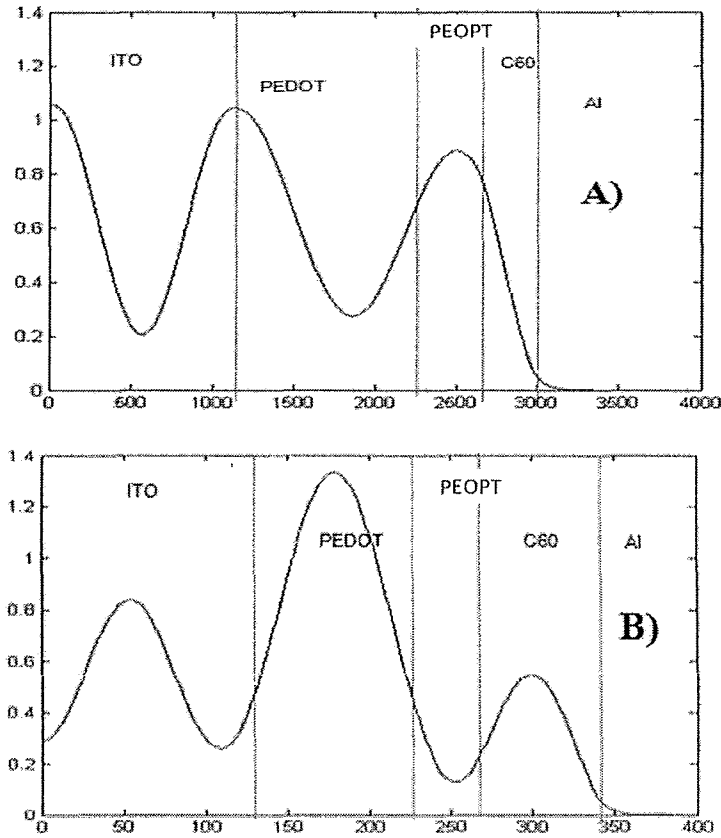


Figure 17: Pattern of the electromagnetic wave amplitude in the six layer solar cell for $\lambda=470\text{nm}$: (A) shows the pattern for a device for C60 layer thickness equal to 35nm, (B) shows the situation for a 80nm thick C60 layer.

Two simulations were performed for two different C60 layer thicknesses (35nm and 80nm). Results are in complete agreement with the results from Pettersson *et.al.* [28]. As Figure 17 shows, they testify that changes in the C60 layer thickness has a dramatic effect on the pattern of light intensity inside an organic solar cell.

Another set of simulations for a 60nm PEOPT thick layer with sixty different C60 layer's thicknesses ranging from 5nm to 300nm was performed. The simulation result shows that for both thicknesses of the PEOPT layer, the highest amplitude of light at the interface can be obtained at a C60 layer thickness of 35nm (Figure 18).

The parameters, which have been used so far, are as below:

- Absorption coefficient, refractive indices (optical coefficients)
- Thicknesses of the layers and their orders
- Amplitude, angel and frequency of the incident beam

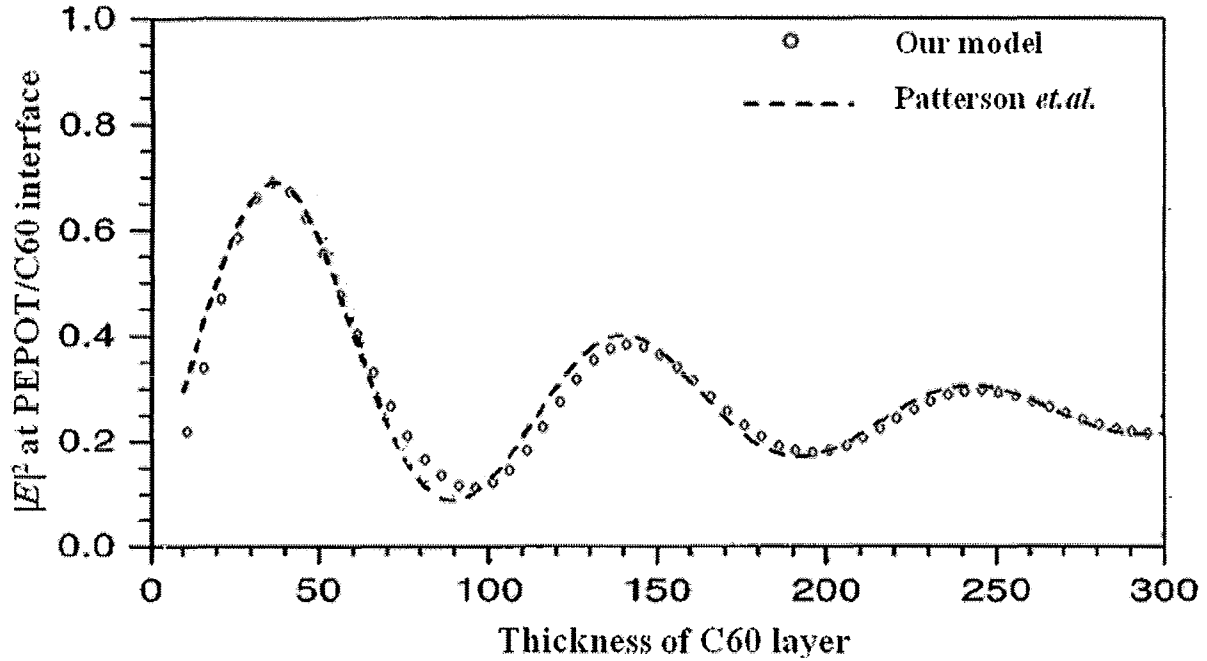


Figure 18: Amplitude of the electromagnetic wave at the active area interface for a 60nm thick PEPOT layer and 60 different thicknesses of C60 layer, ranging from 5nm to 300nm. The result is compared the literature [28].

All of the simulations up to this point were established for a single wavelength of incident light ($\lambda=470\text{nm}$), but the sun light has a vast spectrum. To better understand the behavior of the device, the simulation was repeated for a range of wavelength from 300 to 800nm, where the incident light has an acceptable intensity. The optical modeling was also performed for another device with different materials (ITO 120 nm, PedotPSS 110 nm, PFDTBT 40nm, C60 49nm, Al 30nm).

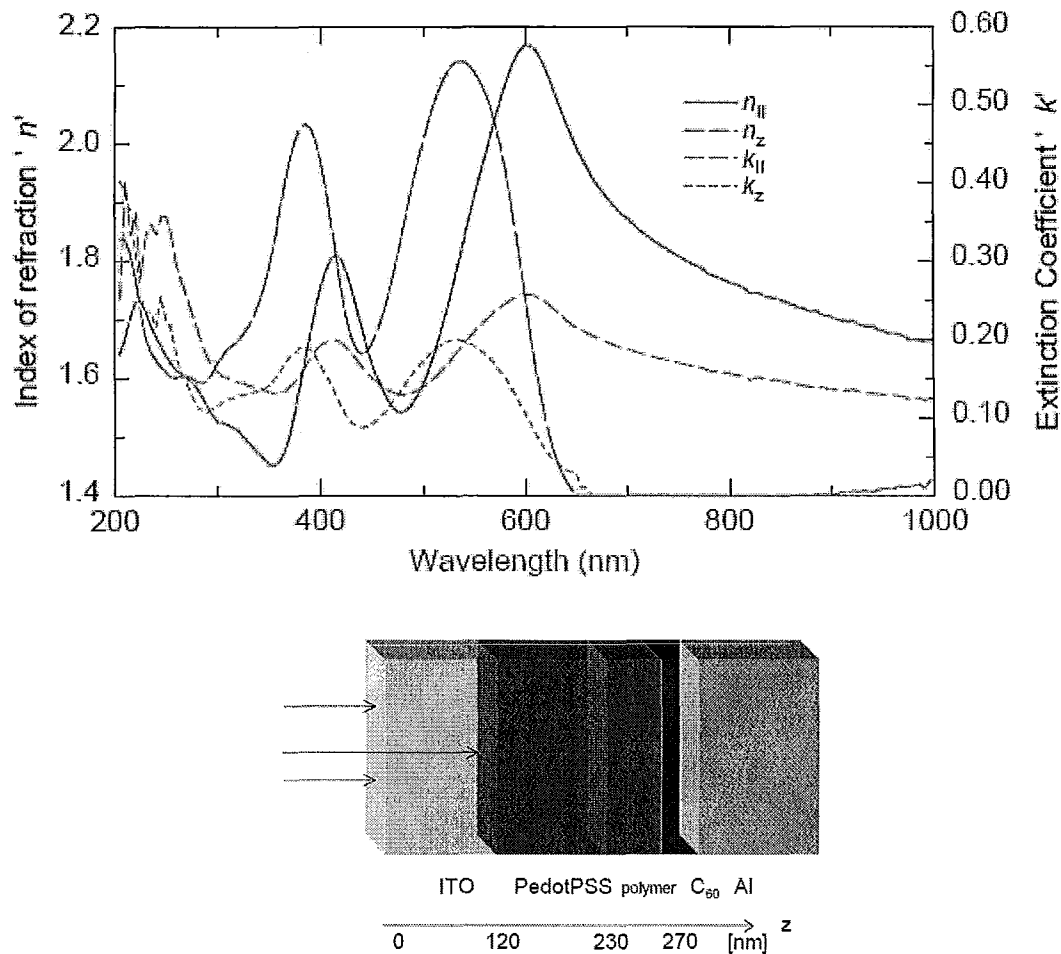


Figure 19: The second device configuration (shown below) and the refractive index of the polymer [poly(2,7-(9-(2'-ethylhexyl)-9-hexylfluorene)-alt-5,5-(4',7'-di-2thienyl-2',1',3'-benzothiadiazole))] [31]

This part of the simulation seeks the best design of a device with the most amount of light absorption close to the active layer interface. Therefore, a set of 400 different solar cell configurations consisting of different combinations of C60 and PFDTBT layers thicknesses (ranging from 5nm to 100nm for each layer) with 17 different frequencies (from 300nm to 700nm) were tried. It is equivalent to conducting the simulation that had been performed to obtain Figure 17, being repeatedly for 6800 different runs. Then, a double integration (an integration over wavelength and another over position) over the absorbed power formula was executed. The formula for the total absorbed power is as:

$$\text{Total absorbed power} = \int \int_{f, z} Q(z, \omega) \quad \text{Equation 15}$$

$Q(z, \omega)$ is the average flow of optical energy dissipation at the point z (z axis begins from the ITO-glass's interface and continues through the device) at the wavelength " ω ". The domain of integration is from 10nm inside PFDTBT layer to 10nm inside C60 layer at the both sides of the active layer's interface for position and from 300nm to 700nm for wavelength. Figure 20 shows the result of the simulation, which is in a good agreement with the results reported in literature [31].

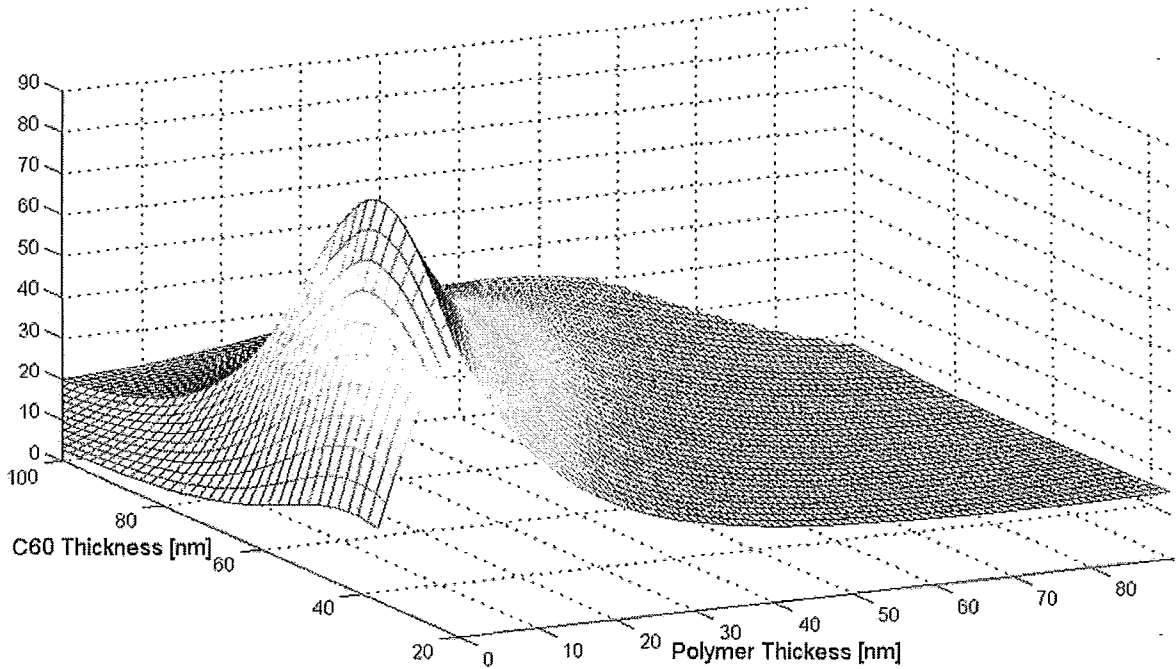


Figure 20: Light absorption as a function of polymer thickness and C60 thickness. The thickness of Pedot:PSS is 100nm and of ITO 120 nm

The Poynting theorem was used to calculate the absorbed power formula used in Equation 15. Based on the Poynting theorem, "*the amount of power dissipation at any point in a conservative environment is equal to the divergence of the Poynting vector at that point multiplied by -1*":

$$Q(z) = -\nabla \cdot S \quad \text{Equation 16}$$

S denotes the Poynting vector. For an electromagnetic wave, it is equal to:

$$S = \frac{1}{\mu} E \times B \quad \text{Equation 17}$$

The electrical field E is calculated by using Equation 14. For an electromagnetic field, we have:

$$\frac{E}{B} = c \quad \text{Equation 18}$$

where B is the magnetic field and c is the speed of light. Using Equation 16, Equation 17 and Equation 18, $Q(z)$ can be written as:

$$Q(z, \omega) = \frac{1}{2} c \varepsilon_0 \alpha n |E(z, \omega)|^2 \quad \text{Equation 19}$$

As Figure 20 shows the best design is achieved for a polymer thickness of 10nm and a C60 layer thickness of 50nm, which confirms the reported results in reference [31]. However, a change in the thicknesses affects not only the light absorption of the device but also its electrical properties such as internal resistances and as a result the I-V curve and therefore, the efficiency of the solar cell. Another way to change the pattern of light intensity inside a solar cell is to have a focusing mechanism at the top layer. In order to model such structures, analytical models such as TM are not helpful and therefore, numerical methods are needed to be used. The next two sections are dedicated to optical modeling of such structures using COMSOL multiphysics.

2.2. OPTICAL MODEL, NUMERICAL ANALYSIS

In this section, first basics of modeling a two dimensional Helmholtz's equation of light propagation in a planar structure using COMSOL multiphysics is described. Then, similar to the previous section, it is explained how the propagation of light can be modeled by calculating the magnitude of the electrical component of the light wave (assuming transversal electric (TE) polarization) inside a planar solar cell.

Finally, building on the framework developed in the previous section, Equation 15 is used to calculate the amount of optical power that is absorbed close to the interface of the active layers. Then, the power is compared for different light focusing deformities at the top layer.

In the developed modeling framework, the magnitude of the electrical field is computed and used to calculate the amount of absorbed optical power and then the number of optically induced excitons.

As mentioned before, we take a beam of light as an electromagnetic wave that travels through different environments. Equation 20 shows the plane wave formula that is being used to characterize the electrical field:

$$E(x, t) = Ae^{i(k \cdot x - \omega t)} \quad \text{Equation 20}$$

2.2.1. TWO DIMENSIONAL OPTICAL MODEL

2.2.1.1. Description of the Two Dimensional Model

This section presents the COMSOL-based model that was developed to capture the physical essence of the optical phenomena under study. Also, extensive simulations were conducted to validate the theory. It was tried to address the basic issues involved in building a COMSOL model [33].

For building models in COMSOL, we benefited from the “Harmonic Propagation” modeling package, from the TE branch of the “In-plane wave” folder of the “RF” module. Figure 21 shows how this package can be found in the opening window of the COMSOL Multiphysics software.

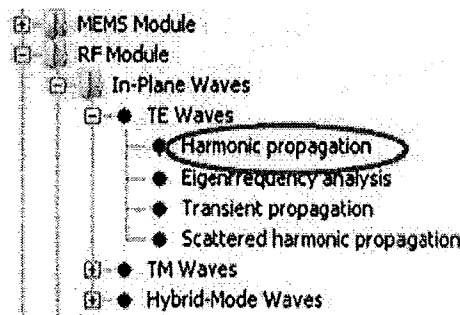


Figure 21: Accessing the Harmonic propagation package at the opening window of the COMSOL Multiphysics

In order to generate a model in this package, one needs to precisely define the boundary conditions, subdomain expressions, type of the sources (planar, polar, *etc.*), material properties

and the policy of the modeling (via writing scrip commands inside COMSOL or controlling the whole COMSOL simulation from an external programming platform such as MATLAB).

After clicking on the “Harmonic propagation” in the opening window, which is shown in Figure 21, from the “Draw” option on the top toolbar one can draw the device geometries. At first a very basic planar device is modeled for two reasons:

- The ease of explanation
- To compare the results with the existing TM results

The next part of the modeling is definition of proper meshing. By clicking on “free mesh parameters” from the “Mesh” section of the top toolbar, maximum mesh dimension for solar cell’s subdomains and the environment that solar cell is in it are chosen to be 10^{-7} m and 4×10^{-6} m, respectively. This arrangement of meshing parameters allows an accurate and yet efficient simulation set up. Boundary meshing parameters can be used to improve the accuracy of the model by providing more information on the active junction (the interface of n-type and p-type materials).

Figure 22 is produced by using the mentioned values for the parameters for the subdomains and setting the maximum of mesh distances on the active interface equal to 1×10^{-8} [m]. After importing all of the parameters for meshing, COMSOL creates the mesh for the planar solar cell as depicted in Figure 22 using an adoptive algorithm for triangular meshing.

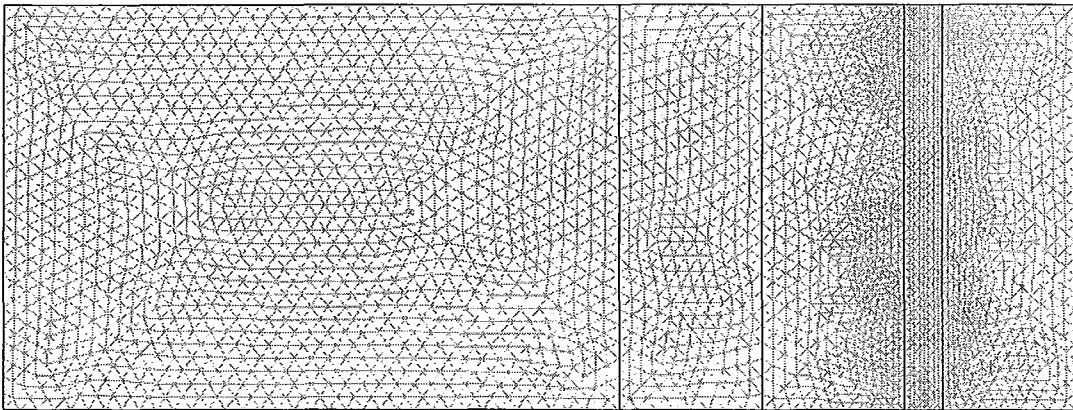


Figure 22: Meshing of a planar solar cell via adaptive meshing.

The next section explains the boundary conditions and we begin with the optical source as the first boundary condition. Figure 23 shows the power spectrum of sunlight for AM 1.5 (“AM” stands for air mass and 1.5 is the coefficient that characterizes the solar spectrum for an absolute air mass of radiation at zenith angle of 48.19° s standardized by ASTM (American Society for Testing and Materials). As is shown in Figure 23, the important part of the solar spectrum (300-700 nm) is given to COMSOL by defining a function named sunlight. Later, it will be explained how a MATLAB or script based model can be run for each given wavelength in Figure 23.

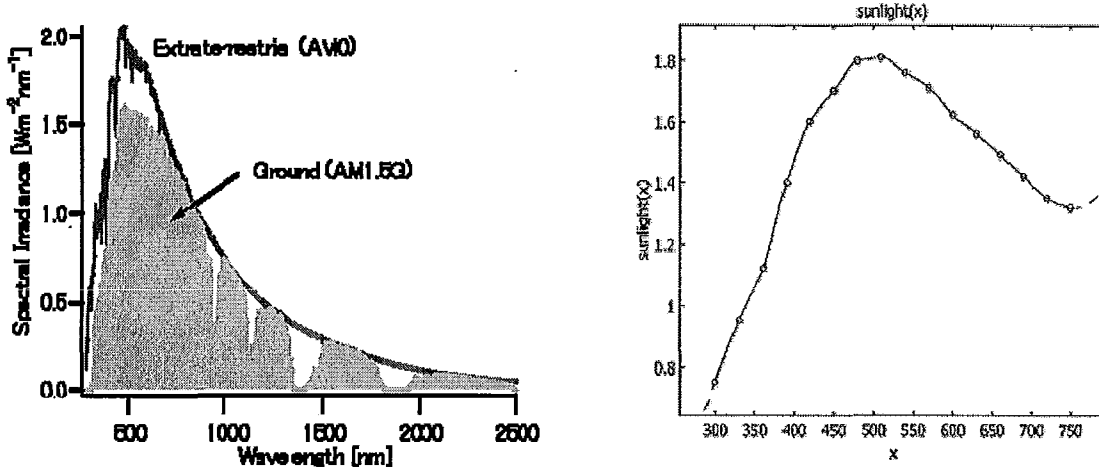


Figure 23: Spectrum of the sun (left) [32], Solar spectrum given to COMSOL (right).

Sunlight is modeled by a planar TE wave source which is described by a planar wave in Equation 20. The organic solar cell that we are going to model can be considered as a lossy object in the middle of a waveguide, which has an even excitation at one of its ports. Consequently, the optical source is an excitation at one end of the environment with different magnitudes for different wavelengths to model the sunlight’s spectrum in Figure 23.

The boundary conditions can be selected as shown in Table 1. These boundary conditions are provided by the “Harmonic Propagation” package and there is no need to add any new conditions. The next section answers the following question: “What is the equivalent physical and mathematical contributes of these boundary conditions?” Also, the boundary conditions for a three dimensional optical model will be described.

Table 1: Boundary conditions for the Harmonic propagation package

Source of light	Energy port with rectangular mode, transverse electric (TE), mode number of 10 and energy equal to sunlight's energy at that wavelength
Interface of two materials with different refractive indices	Continuity (this is the default boundary condition in any interface)
Boundary facing the source of light (the other port of waveguide)	Energy port with rectangular mode, transverse electric (TE), mode number of 10 and zero energy at that wavelength

To define the subdomain, the refractive index is chosen as shown in Figure 24. Later, the refractive indices can be defined as a function of wavelength as shown in Figure 16. As Figure 16 shows refractive indices are composed of two parts: real and imaginary refractive indices (or exciton coefficients):

$$n = \eta + i\kappa$$

Equation.21

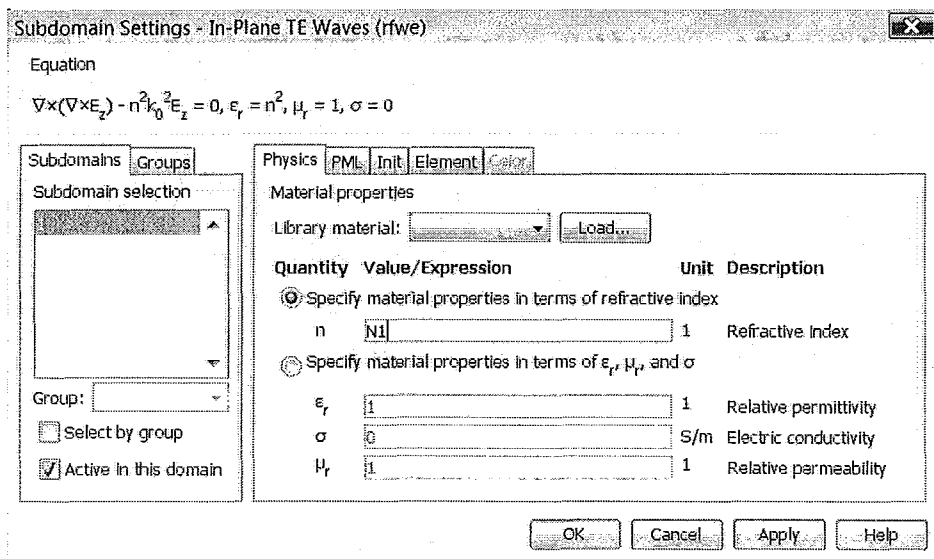


Figure 24: Subdomain settings for the Harmonic propagation package

In this figure, refractive indices of five different materials (Al, PtEOP, PEOPT, ITO and C60) are presented and the refractive index of the environment was assumed to be equal to the refractive index of air ($n=1$).

2.2.1.2. Two Dimensional Model, Results and Discussion

By applying the mentioned coefficients and boundary conditions, the result for the planar solar cell can be obtained. To make sure that the COMSOL model is reliable, the same device was modeled once again, using the TM method and the results were compared to make sure that they are compatible [28]. As shown in Figure 25, the results of two dimensional models and the TM method are in good agreement.

As mentioned before, studying the effect of the focusing aperture was the main reason for developing a numerical method to model the propagation of light inside an organic solar cell. These focusing apertures are also called “capping layers” [29] or “light trapping aperture” [30]. They can also be attributed as one dimensional photonic crystals. Figure 26 shows the result of samples of focusing structures. In Figure 26 the magnitude of electrical field is shown by the color of the pictures. In places with higher magnitude of electrical field, which is directly related to the intensity of light, the color of the picture is red and in places with lower magnitude of light, the color is blue.

Up to this point, the magnitude of the electrical component of the light electromagnetic wave for a two dimensional structure is calculated. Similar to the previous section (TM modeling), the next step is to find which structure will lead to a better efficiency. Therefore, the amount of optical absorbed power close to the active layer interface for different light focusing structures should be calculated and compared.

Transfer Matrix Method Result

ELECTRICAL FIELD'S MAGNITUDE INSIDE OF THE SOLAR CELL

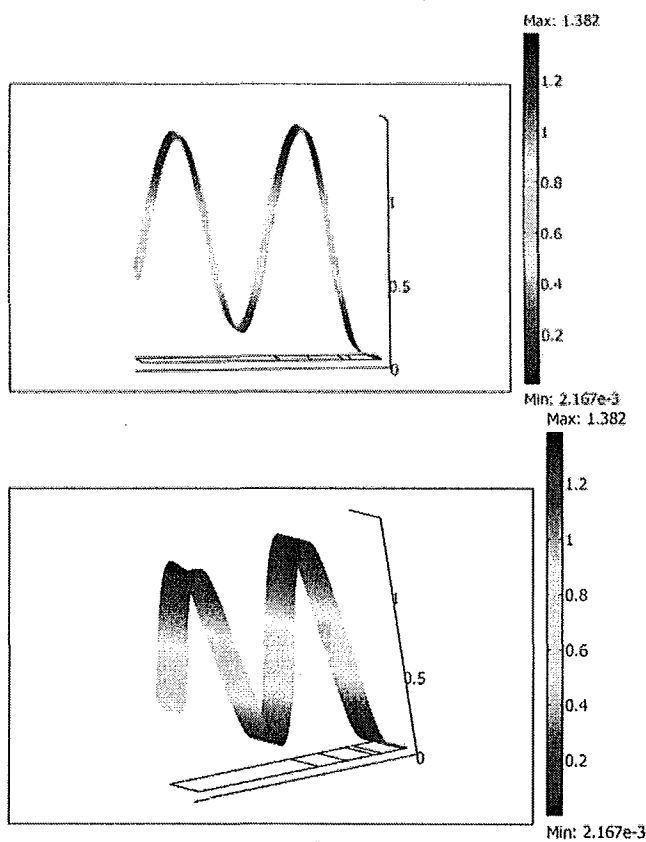
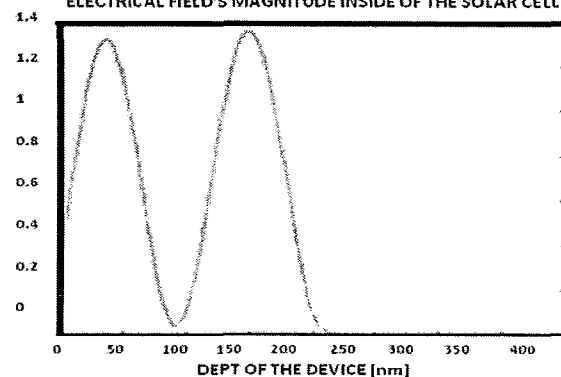


Figure 25: Comparison of TM and COMSOL results.

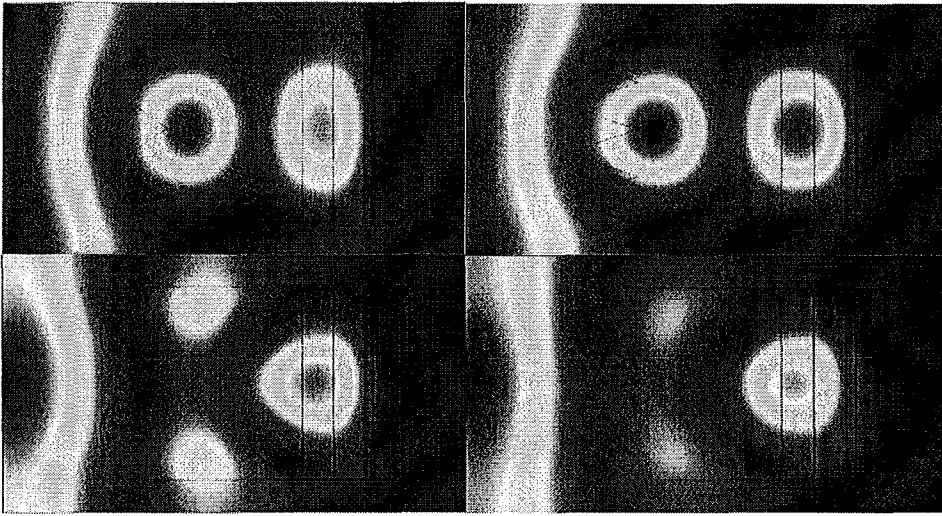


Figure 26: Some capping structure and their effect on profile of light on the device.

To do so, all of the material refractive indices (Figure 16) were given to the software as a function of wavelength. Then, parametric analysis of COMSOL was used with wavelength as the changing parameter, ranging from 325nm to 700nm by 25nm steps. Finally, by using Equation 15 to Equation 19 and integration over frequency and position, total absorbed power was calculated.

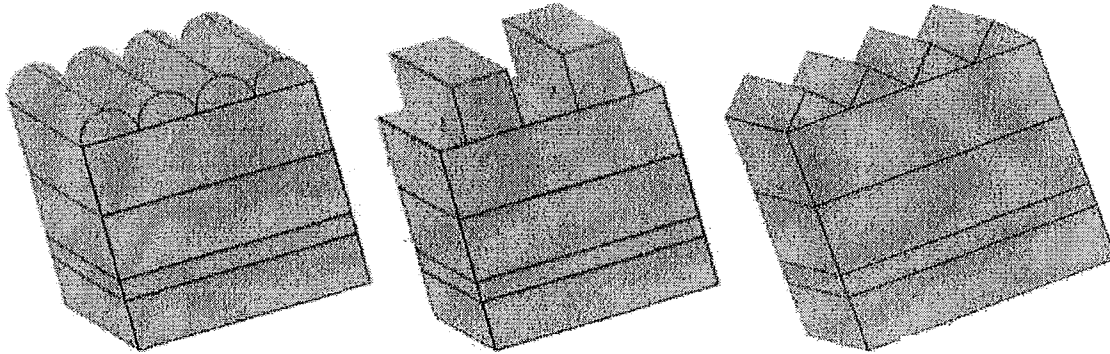


Figure 27: Three dimensional equivalent geometries of the modeled solar cells with three different forms of light trapping structure at the first layer.

The schematic of the geometry of solar cell with three different types of light focusing apertures (triangular, rectangular and semispherical) are shown in Figure 27. This figure shows the three dimensional counterpart of our former two dimensional models.

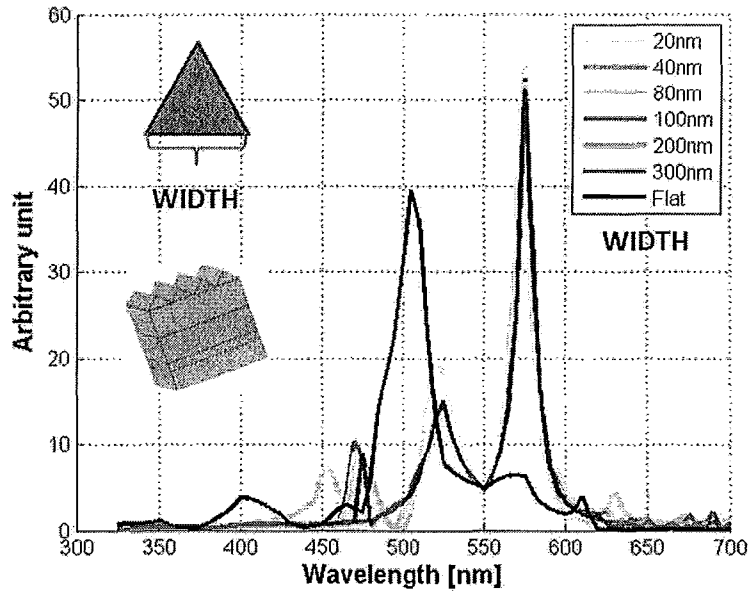


Figure 28: The intensity of light at the interface of C60 and PEOPT for wavelength between 300nm to 700nm, using triangular arrays at the first layer.

Figure 28 shows the magnitude of the electrical field at the active layer interface as a function of wavelength for the same solar cell structure that is shown in Figure 25 with an extra triangular light focusing layer at the top. The triangular light focusing aperture is made of equilateral triangles that are repeated without any distance. Different colors in Figure 28 represent different base width of the triangular light focusing aperture (20nm, 40nm, 80nm, 100nm, 200nm and 300nm) while the height of the triangles are the same and is equal to 40nm. The refractive indices are reported in Figure 16. The color black in this figure shows the amplitude of electrical field in the absence of light focusing layer or a solar cell with a flat surface.

The same type of calculation that have been performed to produce Figure 28 is repeated for Figure 29, with one difference that the light focusing layer used to create Figure 29 is made of rectangular light focusing apertures. A rectangular light focusing layer consists of an array of rectangular cubes repeated by a distance equal to their bases. An example of rectangular light focusing layer can be seen in Figure 27 (the middle picture).

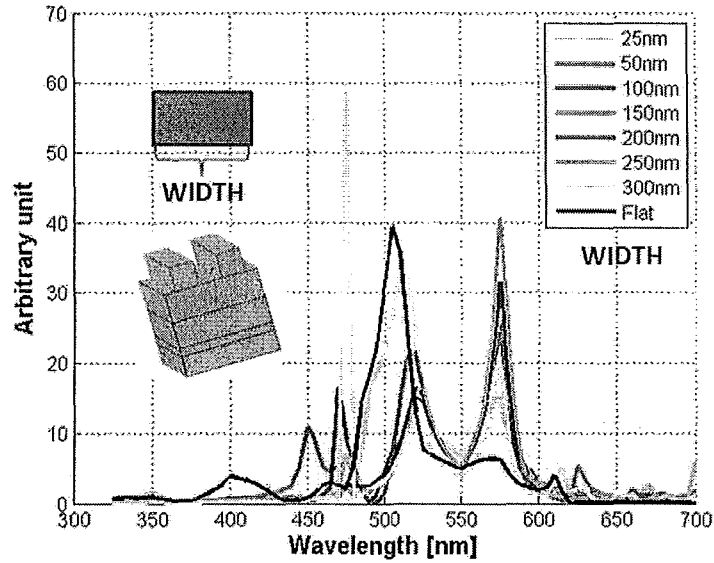


Figure 29: The intensity of light at the interface of C60 and PEOPT for wavelength between 300nm to 700nm, using rectangular arrays at the first layer.

Similar to the previous picture, different colors denote different structures. For different designs of the rectangular light focusing aperture, the height of the repeating structure is equal to 50nm but the width of the rectangle, which is also equal to the distance between two rectangles, varies.

The first column is simply the area under the curves in Figure 28, Figure 29 and Figure 30 divided by the area under the $E-\omega$ curve of the flat surface case presented in all three of the mentioned figures. This column shows the total delivered optical power at the interface of the active layers in all of the cases divided by the amount of total optical power delivered to the interface of the active layers in the case with no focusing aperture.

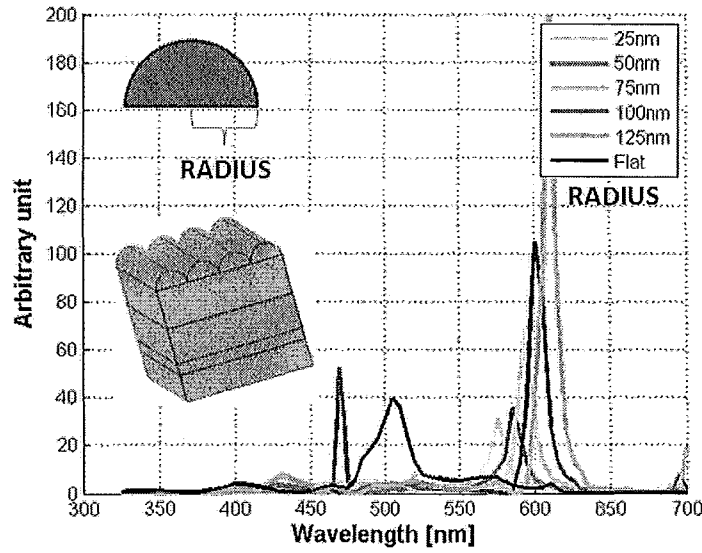


Figure 30: The intensity of light at the interface of C60 and PEOPT for wavelength between 300nm to 700nm, using semicircular arrays at the first layer.

The calculation is the same for Figure 30 with this difference that the repeating structure is made of an array of semicylinders with five different radiuses (25nm, 50nm, 75nm, 100nm and 125nm).

In order to find the best structure, four different parameters were calculated for all of the eighteen light focusing apertures. All of them were normalized by the case that there was no light focusing mechanism (*i.e.* by dividing the result to the result of flat surface simulation). All of the results are shown in Table 2.

The second column is the result of integration of Equation 19 over the frequency and position domains using PEOPT's absorption coefficient as α and calculating $|E|^2$ using the magnitude of E that can be found in Figure 28, Figure 29 and Figure 30, divided by the result from the flat surface case. Therefore, this column shows the ratio of absorbed power close to the active layer interface divided by the result of flat surface organic solar cell.

Table 2: Results of the simulation for the focusing apertures normalized to the flat surface results.

	Total optical Power	absorption in PEOPT	absorption in C60	Total absorption
Triangle 20nm	0.52345	0.39855	0.8689	0.8481
Triangle 40nm	0.4369	0.3932	0.72625	0.71045
Triangle 80nm	0.45695	0.38835	0.702	0.6881
Triangle 100nm	0.45175	0.3891	0.64975	0.63815
Triangle 200nm	0.43175	0.3777	0.60495	0.5948
Triangle 300nm	0.434	0.39075	0.60845	0.5987
Square 25nm	0.58955	0.96445	1.0256	1.02245
Square 50nm	0.46205	0.4397	0.83025	0.81475
Square 100nm	0.4944	0.46895	0.66725	0.65835
Square 150nm	0.3985	0.4790	0.59145	0.5853
Square 200nm	0.3964	0.4188	0.57815	0.57095
Square 250nm	0.406	0.47995	0.54645	0.5303
Square 300nm	0.356	0.41995	0.65335	0.62995
Semicircle 25nm	0.6116	0.9205	1.01535	0.98565
Semicircle 50nm	0.67775	0.25845	1.31055	1.26435
Semicircle 75nm	0.7728	0.22405	1.21075	1.16745
Semicircle 100nm	1.12155	0.49155	1.7	1.63385
Semicircle 125 nm	1.7478	0.28555	2.00945	1.93385

The third column is similar to the second column with the difference that for this column, absorption coefficient of the C60 is used.

Finally, the fourth column presents the total absorbed power for each one of the focusing apertures over the total absorbed power in the case of flat surface.

As can be seen from the table, the best design is related to the semicircular deformities with a radius equal to 125nm that has a 98% increase in optical power absorption at the interface of active layers compare to the flat surface case.

In the next section, the effect of different types of focusing aperture that need a three dimensional model is studied and at the end of the chapter, all of the cases are compared together in order to find the best design.

2.2.2. THREE DIMENSIONAL OPTICAL MODEL

For the two dimensional problems the “Harmonic propagation” package worked perfectly. However, because of extra precaution that have been taken in the package, the simulation cost and memory usage were beyond what an ordinary computer can offer (In this case: Dell inspiron (1526) with 3Gb RAM and 2 AMD CPU’s with 2 GHz operation per second for each). The main problem with FEM-based software is the vast usage of memory, which itself depends on the size of the stiffness matrix. The size of the stiffness matrix depends on the number of the mesh points. Equation 22 and Equation 23 show an estimate for the number of mesh grids as a function of division points at the boundaries in two and three dimensions (Figure 31 depicts the generated meshes).

$$N \times N \times \frac{6}{4} = (N^2)1.5 \quad \text{Two dimensional} \quad \text{Equation 22}$$

$$N \times N \times N \times \frac{25}{6} = (N^3)4.2 \quad \text{Three dimensional} \quad \text{Equation 23}$$

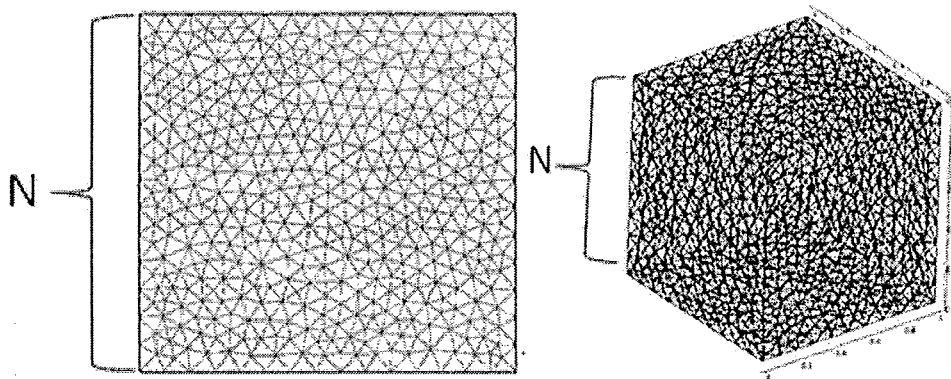


Figure 31: Meshing in COMSOL in two and three dimensions

2.2.2.1. Description of the Three Dimensional Model

It is a well-known fact that an electromagnetic wave follows Maxwell's equations. Maxwell's third and fourth equations are:

$$\nabla \times E = -\frac{\partial B}{\partial t} \quad \text{Equation 24}$$

$$\nabla \times H = J + \frac{\partial D}{\partial t} \quad \text{Equation 25}$$

If we replace $B=\mu H$ in Equation 25 and takes a time derivative and replace the time derivative of B with its equivalent from Equation 24, we have:

$$\nabla \times \frac{-\nabla \times E}{\mu} = -\frac{\partial}{\partial t} J + \frac{\partial^2 D}{\partial t^2} \quad \text{Equation 26}$$

Then from $D=\epsilon E$ and the assumption that there is no current regarding the electromagnetic wave, we have:

$$\frac{1}{\mu} \nabla \times \nabla \times E + \epsilon \frac{\partial^2 E}{\partial t^2} = 0 \quad \text{Equation 27}$$

To simplify Equation 27 one can use:

$$\nabla \times (\nabla \times E) = \nabla (\nabla \cdot E) - \nabla^2 E \quad \text{Equation 28}$$

This will result in:

$$-\nabla^2 E + \epsilon \mu \frac{\partial^2 E}{\partial t^2} = 0 \quad \text{Equation 29}$$

Finally, replacing the plane wave formula of the electric field from Equation 20, leads to the harmonic equation of light propagation:

$$\nabla^2 E + \epsilon \mu \omega^2 E = 0 \quad \text{Equation 30}$$

where ω denotes frequency of the propagating light. To model the three dimensional problem, the ordinary harmonic analyzer is not computationally efficient. Therefore, Equation 30 is directly solved by using stationary analysis of PDE coefficient form of classical PDEs package (Figure 32 shows its passage in the opening window of COMSOL).

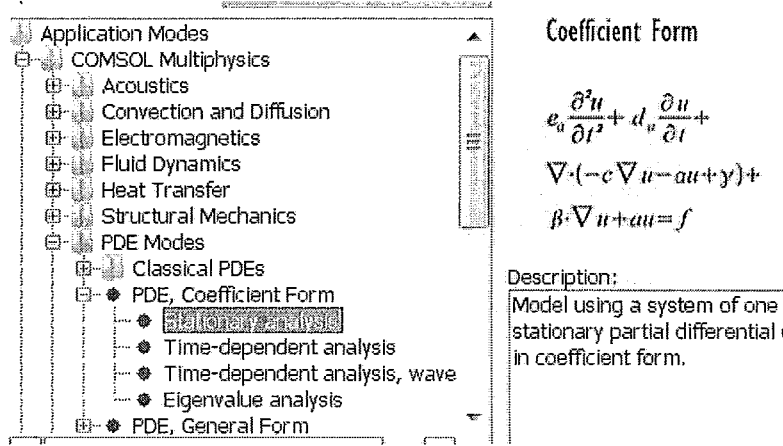


Figure 32: Stationary analysis of PDE coefficient form of classical PDEs package.

The general form of stationary analysis is shown in the right hand side of Figure 32 (Equation 31). Proper values are assigned to the corresponding coefficients in the following formula:

$$\begin{cases} e_a \frac{\partial^2 u}{\partial t^2} + d_a \frac{\partial u}{\partial t} + \nabla \cdot (-c \nabla u - au + \gamma) + \beta \cdot \nabla u + au = f & \text{in } \Omega \\ n \cdot (c \nabla u + \nabla u + \alpha u - \gamma) + qu = g - h^T \mu & \text{on } \partial\Omega \\ hu = r & \text{on } \Omega \end{cases} \quad \text{Equation 31}$$

As Table 3 shows, this package can be used to model the Laplace equation, The Poisson equation, heat equation, wave equation, Schrodinger's equation, convection-diffusion equation and finally the Helmholtz equation, which is the same equation for harmonic analysis of TE wave (Equation 29). In Equation 29, Ω refers to the inside of the three dimensional environment, in which the problem is solved, and $\partial\Omega$ refers to the boundary conditions.

Table 3: The Plethora of equations that can be modeled via PDE coefficient form (stationary analysis).

EQUATION	COMPACT NOTATION	STANDARD NOTATION
Laplace equation	$-\nabla \cdot (\nabla u) = 0$	$-\frac{\partial^2 u}{\partial x^2} - \frac{\partial^2 u}{\partial y^2} - \frac{\partial^2 u}{\partial z^2} = 0$
Poisson equation	$-\nabla \cdot (c \nabla u) = 0$	$-\frac{\partial}{\partial x} \left(c \frac{\partial u}{\partial x} \right) - \frac{\partial}{\partial y} \left(c \frac{\partial u}{\partial y} \right) - \frac{\partial}{\partial z} \left(c \frac{\partial u}{\partial z} \right) = f$
Helmholtz equation	$-\nabla \cdot (c \nabla u) + \alpha u = f$	$-\frac{\partial}{\partial x} \left(c \frac{\partial u}{\partial x} \right) - \frac{\partial}{\partial y} \left(c \frac{\partial u}{\partial y} \right) - \frac{\partial}{\partial z} \left(c \frac{\partial u}{\partial z} \right) + \alpha u = f$
Heat equation	$d_a \frac{\partial u}{\partial t} - \nabla \cdot (c \nabla u) = f$	$d_a \frac{\partial u}{\partial t} - \frac{\partial}{\partial x} \left(c \frac{\partial u}{\partial x} \right) - \frac{\partial}{\partial y} \left(c \frac{\partial u}{\partial y} \right) - \frac{\partial}{\partial z} \left(c \frac{\partial u}{\partial z} \right) = f$
Wave equation	$d_a \frac{\partial^2 u}{\partial t^2} - \nabla \cdot (c \nabla u) = f$	$d_a \frac{\partial^2 u}{\partial t^2} - \frac{\partial}{\partial x} \left(c \frac{\partial u}{\partial x} \right) - \frac{\partial}{\partial y} \left(c \frac{\partial u}{\partial y} \right) - \frac{\partial}{\partial z} \left(c \frac{\partial u}{\partial z} \right) = f$
Schrodinger equation	$-\nabla \cdot (c \nabla u) + \alpha u = \lambda u$	$-\frac{\partial}{\partial x} \left(c \frac{\partial u}{\partial x} \right) - \frac{\partial}{\partial y} \left(c \frac{\partial u}{\partial y} \right) - \frac{\partial}{\partial z} \left(c \frac{\partial u}{\partial z} \right) + \alpha u = \lambda u$
Convection-diffusion equation	$d_a \frac{\partial u}{\partial t} - \nabla \cdot (c \nabla u) + \beta \cdot \nabla u = f$	$d_a \frac{\partial u}{\partial t} - \frac{\partial}{\partial x} \left(c \frac{\partial u}{\partial x} \right) - \frac{\partial}{\partial y} \left(c \frac{\partial u}{\partial y} \right) - \frac{\partial}{\partial z} \left(c \frac{\partial u}{\partial z} \right) + \beta_x \frac{\partial u}{\partial x} + \beta_y \frac{\partial u}{\partial y} = f$

Table 4 shows how to choose values of the corresponding coefficient to model the Helmholtz problem.

Table 4: Parameters values for generating Helmholtz's equation.

Parameter	Quantity
β	0
γ	0
α	0
a	$\epsilon \mu \omega^2$
e_a	0
d_a	0
f	0
c	-1

After assigning proper values to the parameters, the next step is to take care of the boundary conditions. The general equations of boundary conditions for an electromagnetic wave in all sorts of environments are shown in Table 5.

Two types of boundary conditions are included in the PDE package: Dirichlet boundary condition and Neumann boundary condition.

$$n \cdot (c \nabla u + au - \gamma) + qu = g \quad \text{Equation 32}$$

$$n \cdot (c \nabla u + au - \gamma) + qu = g - h^T \mu; \quad hu = r \quad \text{Equation 33}$$

Equation 32 shows the Neumann boundary conditions at the border. The only undefined parameters in this equation are q and g . The rest of the parameters have already been defined by defining the model of the Helmholtz's equation. Consequently, Equation 33 shows the Dirichlet boundary conditions. Similar to Equation 32, parameters in Equation 33 are all defined except for q , g , h , r and μ which denotes the magnetic permeability.

Table 5: General boundary conditions, for electromagnetic waves

	General	Finite conductivity media, no source or charges $\sigma_1, \sigma_2 \neq \infty$ $J_s = M_s = 0; q_{es} = q_{ms} = 0$	Medium of infinite electric conductivity $\sigma_1 = \infty; \sigma_2 \neq \infty; M_s = 0; q_{ms} = 0$	Medium of infinite Magnetic conductivity $(H_{1t} = 0) J_s = 0; q_{es} = 0$
Tangential electric field intensity	$\hat{n} \times (E_2 - E_1) = -M$	$\hat{n} \times (E_2 - E_1) = 0$	$\hat{n} \times E_2 = 0$	$\hat{n} \times E_2 = -M$
Tangential magnetic field intensity	$\hat{n} \times (H_2 - H_1) = -J_s$	$\hat{n} \times (H_2 - H_1) = 0$	$\hat{n} \times H_2 = J_s$	$\hat{n} \times H_2 = 0$
Normal electric flux density	$\hat{n} \cdot (D_2 - D_1) = -q_{es}$	$\hat{n} \cdot (D_2 - D_1) = 0$	$\hat{n} \cdot D_2 = q_{es}$	$\hat{n} \cdot D_2 = 0$
Normal electric magnetic flux density	$\hat{n} \cdot (B_2 - B_1) = -q_{ms}$	$\hat{n} \cdot (B_2 - B_1) = 0$	$\hat{n} \cdot B_2 = 0$	$\hat{n} \cdot B_2 = q_{ms}$

Table 6 shows the mentioned boundary conditions and the proper definition of coefficients. Now that everything is completed the next step is to properly run the described model. There are two ways to do this:

- Using equivalent M-file for the model by connecting to MATLAB server (by following this path: File/Client-server/MATLAB) and then saving the model as an M-file. Next, by defining a for-loop on wavelength and changing all the parameters based on their wavelength equivalents and then getting an integral on electric field magnitude, the model will be completed.
- Instead of stationary analysis and then use of MATLAB platform, parametric analysis can also be used by defining wavelength as the changing parameter, just like the two dimensional section.

Table 6: Choosing of parameters to generate the needed boundary conditions.

	Finite conductivity media, no source or charges $\sigma_1, \sigma_2 \neq \infty$ $J_s = M_s = 0; q_{es} = q_{ms} = 0$	Medium of infinite electric conductivity $\sigma_1 = \infty; \sigma_2 \neq \infty; M_s = 0; q_{ms} = 0$	Source
Dirichlet boundary condition	$g = 0, q = 0, h = 0, r = 0$	$g = 1, q = 0, h = 1, r = 0$	$g = 1, q = 0, h = 1, r = 1$
Neumann boundary condition	$g = 0, q = 0$	$g = 1, q = 0$	$g = 1, q = 0$

In a typical solar cell, the required electromagnetic boundary conditions are:

- the boundary condition between two layers with finite electrical conductivity with no charge and source of light
- interface of semiconductor and metal (or medium with close to infinite electric conductivity)
- source of light

2.2.2.2. Three Dimensional Model, Results and Discussion

In both of the mentioned methods, all of the changing parameters such as complex refractive indices and the source of light should be considered as a function of wavelength (by following this path: Options/Functions). Figure 33 shows the result of a simple two layered device inside a bigger box that models the environment (air condition with electrical permittivity and magnetic permeability equal to one).

Using parameters in Table 6 the top face of the outer box is designed to be the source of light with magnitude one, which is represented by the red color at the top of the box. The blue color in the middle of the picture has the largest light intensity, which is calculated as $|E^2|$. This is the inverse of quantum well concept for electron wave in Schrödinger's equation. In the case of quantum well, the electron wave has the highest magnitude inside the well. For solution of light propagation in an environment with different refractive indices, light will be trapped inside the materials with higher refractive indices. Figure 34 shows a quantum well besides a light trapping specimen (this technique of light trapping is extensively used in fiber optics [39, 40])

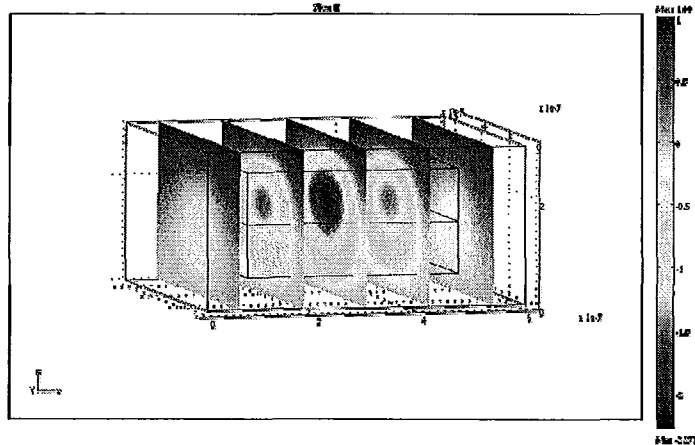


Figure 33: results of a simple three dimensional two layered structure

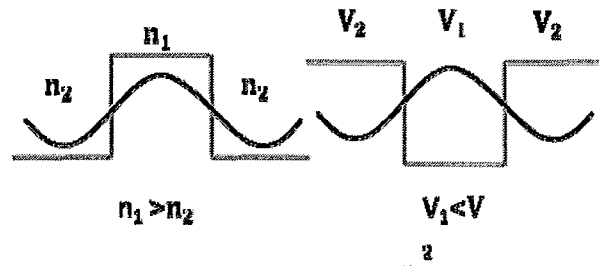


Figure 34: Quantum well and a structure with different refractive indices.

Similar to the pervious chapter, we examine the effect of light focusing deformation at the first layer of the solar cell. To keep the consistency of the thesis and to provide an overall comparison, in the following we study the effect of deformity at the top layer of the solar cell with the same structure of Figure 19 on the intensity of light in the interface of PEOPT and C60. Three types of deformities are considered: semisphere, cones and blocks as Figure 35 shows.

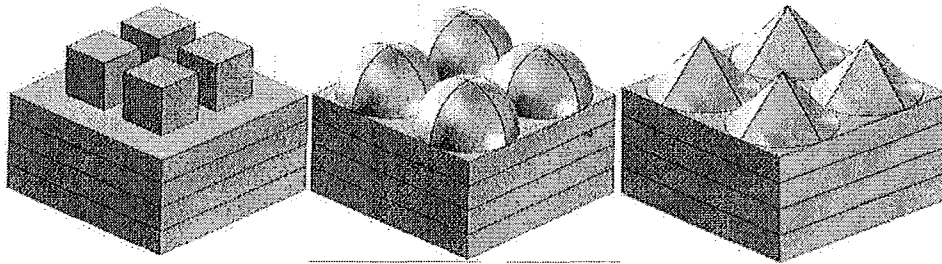


Figure 35: Three different light focusing first layer structure: cones, semisphere and blocks

Unlike the two dimensional model, due to the computational complexity, the three dimensional model cannot be solved for a large structure that can be used to estimate all the back reflections reliably. However, by using an interesting trick in the definition of the boundary conditions in the sides of a device, the effect of periodicity can be included. Figure 36 shows the effect of boundary conditions. It is similar to a room with mirrors on each wall.

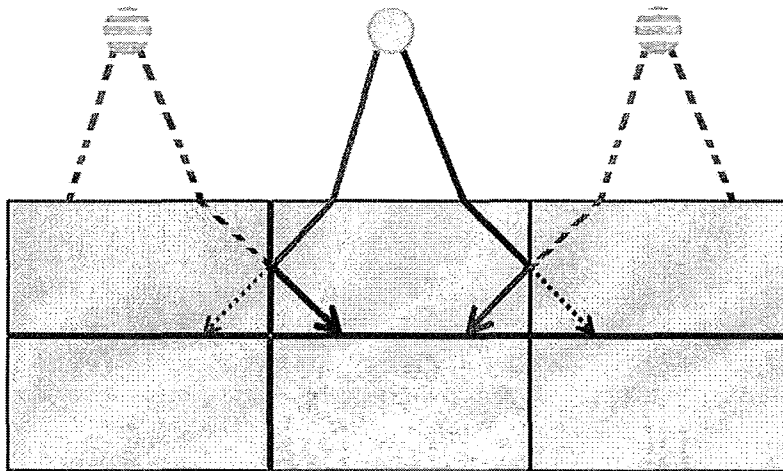


Figure 36: Concept of mirror boundary condition with a real source of light in the middle and two imaginary sources of light in its right and left. (imaginary rays are represented by dotted lines).

This type of boundary condition is similar to the situation that two mirrors are facing each other. In Figure 36, two beams of light are depicted by two lines (blue line in the left and red line in the right). As shown in the picture, there is one real source of light with real beams of light (solid lines) and two imaginary sources of light in the left and right of the real source (dotted lines). As it is shown in the picture, if everything is symmetric inside and outside of the solar cell, mirror boundary will model the effect of a device with infinite width.

Similar to the previous section, the magnitude of electrical field for different designs by using the model described in here with all of the refractive indices from Figure 16, is calculated and depicted in Figure 37, Figure 38 and Figure 39.

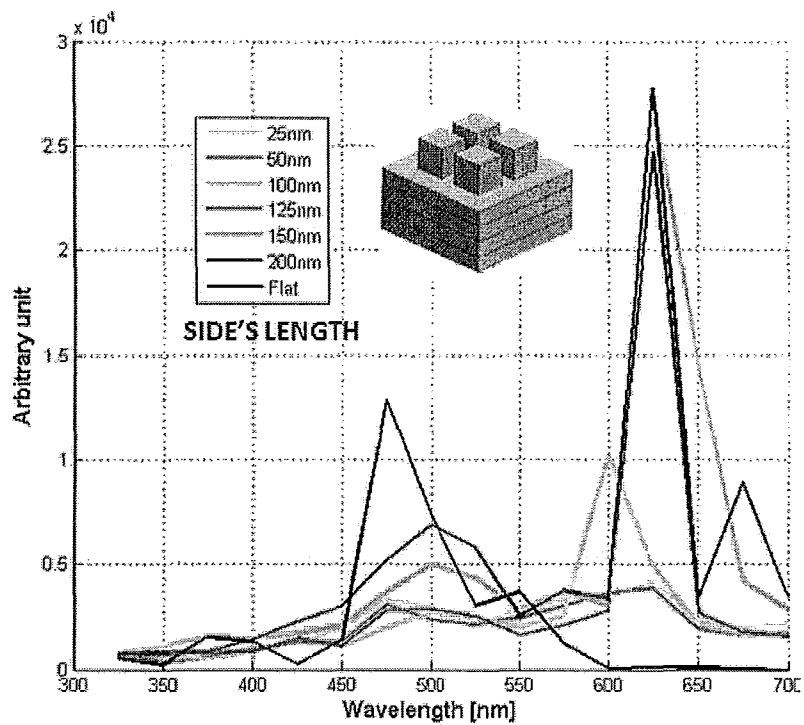


Figure 37: The intensity of light at the interface of C60 and PEOPT for wavelengths between 325nm and 700nm, using blocks at the first layer.

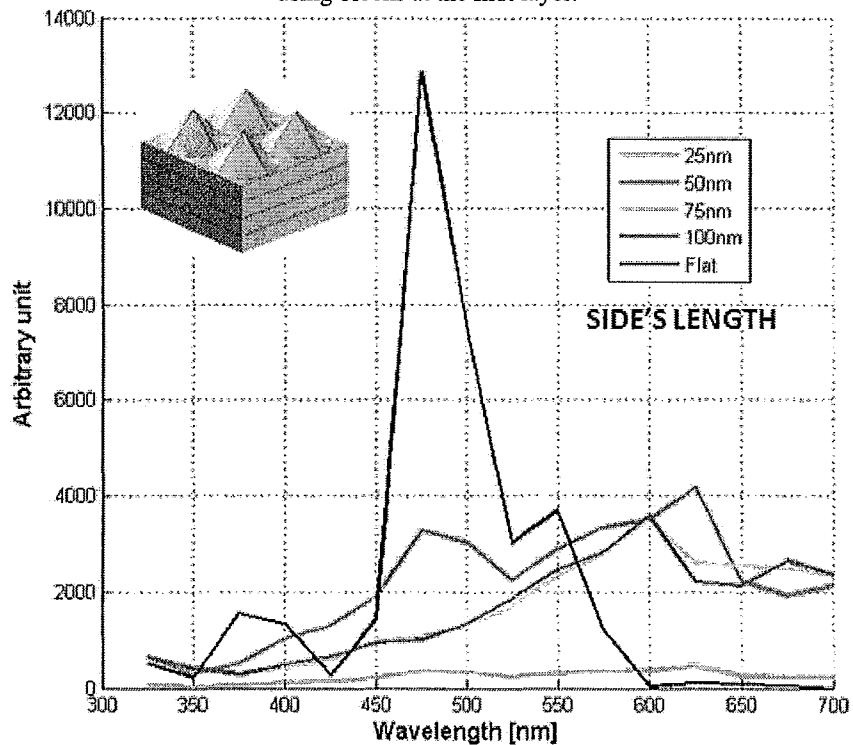


Figure 38: The intensity of light at the interface of C60 and PEOPT for wavelengths between 300nm and 700nm, using cones at the first layer.

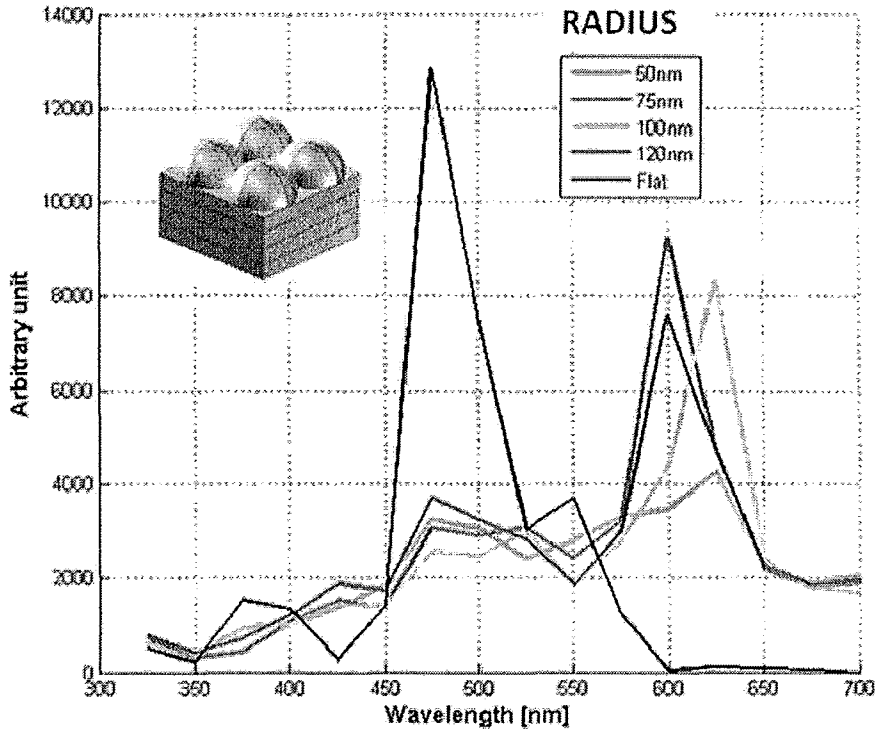


Figure 39: The intensity of light at the interface of C60 and PEOPT for wavelengths between 300nm and 700nm, using spheres at the first layer.

Finally, all of the results are summarized in Table 7. Description of each column is the same as Table 6. It can be concluded that the best design is for the case of usage of blocks with the scale of 150nm. In general comparison with the results of two dimensional light focusing apertures reveals that the best design is the semicylindricals with radius equal to 125nm increases the amount of absorbed power compared to the flat surface case by 98%.

The next step in modeling is to use the calculated amount of absorbed power to find the density of generated excitons. To do so, we assumed that for the wavelengths larger than the active layers' bandgap, (for the exchange efficiency=1), the number of excitons for each wavelength can be calculated using the following formula:

$$\#excitons = \frac{Q(x, \omega)}{\hbar \omega} \Big|_{\text{for } \hbar \omega > E_g} \quad \text{Equation 34}$$

Having the number of excitons, the amount of generated electrical current can be obtained. This topic is explained in details in the next chapter.

Table 7: Results of the simulation for the focusing apertures normalized to the flat surface results

	Total optical Power	absorption in PEOPT	absorption in C60	Total absorption
Block 25nm	1.0162	1.2113	0.7519	0.9816
Block 50nm	0.9100	1.3458	0.6905	1.0181
Block 100nm	1.1022	1.7177	0.7360	1.2269
Block 125nm	1.5090	1.6952	0.8603	1.2777
Block 150nm	2.3622	2.3061	1.3106	1.8084
Block 200nm	2.3729	2.0033	1.3321	1.6677
cone 25nm	1.0085	1.3002	0.7444	1.0223
cone 50nm	1.0189	1.3126	0.7534	1.0330
cone 75nm	0.7688	1.4043	0.4808	0.9425
cone 100nm	0.7644	1.4151	0.4890	0.9521
Sphere 50nm	1.0155	1.2992	0.7470	1.0231
Sphere 75nm	1.1845	1.4449	0.7958	1.1203
Sphere 100nm	1.1008	1.6196	0.8021	1.2108
Sphere 120nm	1.1769	1.6494	0.8867	1.2681

CHAPTER 3

ELECTRICAL MODELING

3. ELECTRICAL MODELING

In this section, the electrical model for two types of organic solar cells (bilayer heterojunction and bulk heterojunction organic solar cells) is described. One of the important characteristics of organic materials is their extremely small mobility, which makes modeling of their electrical properties difficult. However, as was mentioned before, we used COMSOL multiphysics that employs FEM as its discretization method, which is a stable numerical method. Benefiting adaptive feedback and adaptive meshing properties of COMSOL the modeling becomes more stable and efficient.

Another problem in the electrical modeling of organic thin film devices (*e. g.* planar organic solar cells) was the lack of unique and precise electrical parameters for very thin layers of materials and occasionally lack of any information. For instance, Indium Thin Oxide's (ITO) parameters which are reported below (ITO is one of the usual materials in most of planar solar cells and especially organic solar cells) is a perfect example. Table 8 shows the differences between the ITO parameters reported from different references.

The first section of this chapter is dedicated to the analytical solution of the exciton diffusion equation which is related to the bilayer heterojunctions. In this model, it is assumed that a fraction of excitons that can reach the interface of active layers, and get separated into pairs of electron and holes, will generate the short circuit current of the organic solar cell. Later, it will be described how IPCE of the organic solar cell can be calculated, using the calculated short circuit current.

In the next section, the electrical model of bulk heterojunction organic solar cell is described, using COMSOL multiphysics software. In this section, with the aid of a self consistent loop

between the Poisson equation and continuity equations for electrons and holes, the I-V curve of the device is calculated.

Table 8: Reported parameters of ITO.

Deposition Technique	Thickness [Å]	Hall Mobility [$\text{cm}^2.\text{V}^{-1}.\text{s}^{-1}$]	Carriers [cm^{-3}]	Resistivity [$\Omega.\text{cm}$]	Transmittance [%]	Ref. No.
r.f. Sputtering	7,000	35	6e20	3e-4	90	[45]
r.f. Sputtering	5,000	12	12e20	4e-4	95	[46]
r.f. Sputtering	4,000	25	3e20	8e-4	-	[47]
Magnetron Sputtering	800	26	6e20	4e-4	85	[48]
d.c. Sputtering	1,000	35	9e20	2e-4	85	[49]
Reactive Evaporation	2,500	30	5e20	4e-4	91	[50]
Ion Beam Sputtering	600	26	2e20	12e-4	-	[51]
Spray Pyrolysis	3,000	45	5e20	3e-4	85	[52]

Finally, comparing numerical and experimental result, it is concluded that there should be a tunneling current besides the thermionic emission, which can be calculated by the COMSOL model. The tunneling current is the direct result of connection between a metallic contact and a layer of organic material. Therefore, by fitting an I-V curve of a tunneling current to the difference of experimental and numerical result, the electrical characteristics of the connection interface is calculated and reported.

3.1. ELECTRICAL MODEL, ANALYTICAL ANALYSES

The next part of the modeling is to calculate the optical current generated in the solar cell. To do so, the excitons distribution equation as a function of position and light intensity will be found by assuming that the exciton separation into electron-hole pair only happens in the interface of n-type and p-type materials, the short-circuit current can be calculated, and from there, IPCE can be found.

3.1.1. EXCITON DIFFUSION EQUATION

3.1.1.1. Description of the Exciton Diffusion Model

Number of references solved the problem of exciton diffusion (assuming that after excitation the number of excitons follows the profile of light distribution) as [21-26]:

$$S(x) = \alpha I_0 e^{-\alpha x} \quad \text{Equation 35}$$

Equation 35 implies that $S(x)$ (the number of excitons) will decay by an exponential function of distance (x) from the incident point. However, the reality is that the excitons, like any other particle, diffuse into their neighbourhood. Therefore, assuming that the total change in the number of excitons ($n(x)$) at the point x (distance from the sight of the excitation), is due to diffusion and decay, the equation for exciton density become:

$$\frac{\partial n}{\partial t} = D \frac{\partial^2 n}{\partial x^2} - \frac{n}{\tau} + \frac{\theta_1}{h\nu} Q(x) \quad \text{Equation 36}$$

In this equation, $Q(x)$ is the absorbed energy which has been calculated in the previous section, D is the diffusion constant, τ is the mean lifetime of the exciton, θ_1 is the exciton exchange efficiency and $h\nu$ is the creation energy of an exciton where ν stands for the frequency of the absorbed light.

Knowing the classical PDE equation, one can conclude that Equation 36 is the diffusion equation for excitons (where excitons are taken as the diffusive particles inside the device), and like any diffusion equation, it consists of three terms:

- The diffusion term (due to uneven absorption of light)
- The dissipation term (due to dissociated excitons)
- The generation term (due to optical generation of excitons).

For the steady state situation (Where the time derivative of n is zero), Equation 36 can be rewritten as:

$$\frac{d^2 n}{dx^2} = \beta^2 n(x) - \frac{\theta_1}{D h \nu} Q(x) \quad \text{Equation 37}$$

In the above equation β is the inverse of the exciton diffusion length:

$$\beta = 1/L = 1/\sqrt{D\tau} \quad \text{Equation 38}$$

Using analytical solution of the Equation 37, $n(x)$ would have an exponential form as:

$$n(x) = \frac{\theta_1 \alpha T N}{D(\beta^2 - \alpha^2)} \left[A.e^{-\beta x} + B.e^{\beta x} + C_1.e^{\alpha x} + C_2.\cos\left(\frac{4\pi\eta}{\lambda}(d-x) + \delta''\right) \right] \quad \text{Equation 39}$$

In the above equation N stands for the number of photons per unit area, the coefficient (δ'') is the argument of the complex reflection coefficient that have been calculated in the TM section and C_1 and C_2 are defined as below:

$$C_1 = \rho''^2 e^{-2\alpha d} \quad \text{Equation 40}$$

$$C_2 = \frac{(\beta^2 - \alpha^2)}{(\beta^2 + (4\pi/\lambda)^2)} 2\rho'' e^{-\alpha d} \quad \text{Equation 41}$$

Therefore, only A and B from Equation 39 are unknown. To find these two unknowns, the boundary conditions should be applied. Assuming that excitons either decay during the diffusion or totally dissociate at the interface, the total number of excitons at the boundaries should be equal to zero ($n(x) = 0$ at the boundaries). Therefore, substituting the boundary conditions in

Equation 39, and solving a system of two unknowns in two equations, terms A and B can be calculated as:

$$A = \frac{(e^{\beta d} - e^{-\alpha d}) + C_1(e^{\beta d} - e^{\alpha d}) + C_2 \left[e^{\beta d} \cdot \cos\left(\frac{4\pi\eta}{\lambda}d + \delta''\right) - \cos(\delta'') \right]}{(e^{-\beta d} - e^{\beta d})} \quad \text{Equation 42}$$

$$B = - \frac{(e^{-\beta d} - e^{-\alpha d}) + C_1(e^{-\beta d} - e^{\alpha d}) + C_2 \left[e^{-\beta d} \cdot \cos\left(\frac{4\pi\eta}{\lambda}d + \delta''\right) - \cos(\delta'') \right]}{(e^{-\beta d} - e^{\beta d})} \quad \text{Equation 43}$$

Having the distribution of excitons as a function of position, the density of excitons' diffusive current at the interface of active layers can be written as the derivative of the exciton distribution:

$$J_{Exc} = D \frac{dn}{dx} \Big|_{x=0} \quad \text{Equation 44}$$

$$J_{Exc} = -D \frac{dn}{dx} \Big|_{x=d} \quad \text{Equation 45}$$

By assuming that every with an exchange rate of θ for exciton density to carrier density ($\theta=2$ for an ideal condition and $\theta < 2$ by assuming electron-hole recombination at the surface of the electrodes). Therefore, by using Equation 45 and θ , the photocurrent can be calculated as

$$J_{Photo} = q\theta J_{Exc} \quad \text{Equation 46}$$

For a bilayer structure, the calculated current at both ends of the device should be equal and should have opposite directions in the short circuit condition. Therefore, using either one of Equation 44 or Equation 45 the short circuit photocurrent of the organic solar cell can be calculated:

$$J_{Photo}|_{x=d} = \frac{q\theta\alpha TN}{(\beta^2 - \alpha^2)} \left(\beta A \cdot e^{-\beta d} - \beta B \cdot e^{\beta d} + \alpha \cdot e^{-\alpha d} + \alpha C_1 \cdot e^{\alpha d} - \frac{4\pi\eta}{\lambda} C_2 \cdot \sin[\delta''] \right) \quad \text{Equation 47}$$

3.1.1.2. Exciton Diffusion Equation Results and Discussion:

One way of finding efficiency of a solar cell is to divide the calculated current by the incident of monochromatic photon stream which (or shortly IPCE) [28]:

$$IPCE(\%) = 1240 \times \frac{J_{Photo}}{\lambda I_0} \quad \text{Equation 48}$$

In the above equation, J_{Photo} ($\mu\text{A}/\text{cm}^2$) is the calculated photocurrent, λ is the wavelength (nm) and I_0 is the light intensity (W/m^2). The IPCE for the first device was calculated for 16 different wavelengths (400nm-7000nm). A schematic model of the organic solar cell's structure shown in Figure 40 and has the following characteristics: 1 mm thick layer of glass, 120nm ITO, 110 nm PEDOT, 40 nm PEOPT and 31 nm C60. Using trial and error, the best fit with the measurement is obtained for diffusion lengths equal to 6nm and 7nm for PEOPT and C60 respectively (Figure 41).

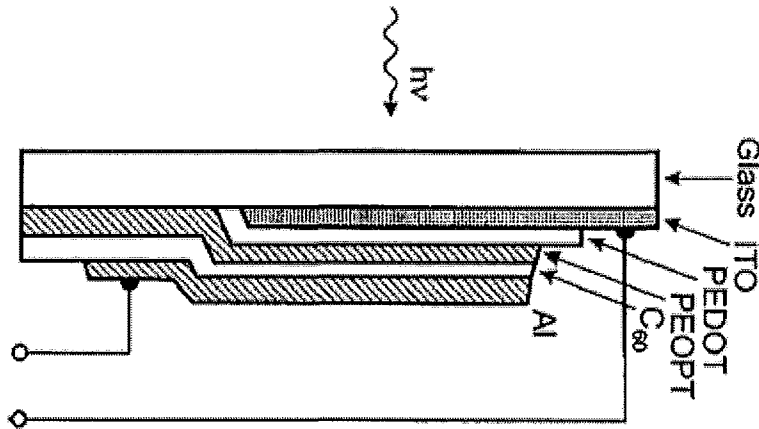


Figure 40: The structure of the solar cell that has been modeled in this section [28].

The results show that the best IPCE of 21% can be obtained at 457 nm. The result has a good agreement with the experimental result reported in [28]. In summary, all of the simulations that had been completed in this section are as follows:

- Electrical modeling of a bilayer heterojunction solar cell by solving the exciton diffusion equation
- Calculating the optical current at the electrodes
- Finding the IPCE ratio

The next section is on numerical modeling of bulk heterojunction organic solar cells. This is done by solving the Poisson equation and the continuity equation in a self consistent loop by using COMSOL multiphysics software.

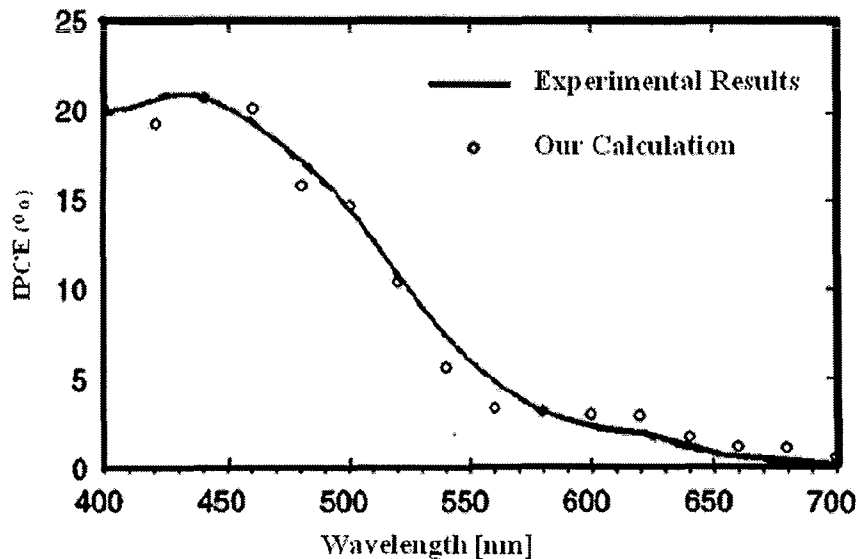


Figure 41: The IPCE (Incident monochromatic Photon to Current collection Efficiency) calculated for the first solar cell compared to the experimental result reported in [28].

3.2. NUMERICAL ANALYSIS, ELECTRICAL MODEL

Since through the previous sections, the optical modeling for both analytical (transfer matrix method) and numerical analyses (modeling of the wave propagation by solving the Maxwell equations for the harmonic analyses in two and three dimensions), as well as the electrical model

of bilayer heterojunction organic solar cells were discussed, this section deals with electrical modeling of bulk heterojunction organic solar cells to complete the modeling of solar cells.

It is assumed that the electrical current is due to the drift-diffusion transport of carrier. Consequently, in order to model the drift diffusion equations, a self consistent loop between the solutions of Poisson's equation and two separate continuity equations for electrons and holes is needed. The design of the loop should be in a way such that the solution of each equation can be used as the initial conditions for the others, to generate a self correcting mechanism.

In order to check the accuracy of the model, results are compared with the numerical results reported in [41] for different doping concentration in the active region. Later, at the end of this section, results are also been compared to the experimental result. It will be shown that the numerical and experimental results have dissimilarity. In order to describe this difference, the tunneling correction is introduced in the next section.

3.2.1. DRIFT-DIFFUSION MODEL

3.2.1.1. Description of the Drift-Diffusion Model

In this section, a bulk heterojunction organic solar cell (OSC) is chosen to be modeled. The bulk heterojunction OSC is a solar cell that has both n- and p-type materials as a mixture in the same layer. From this point, we will call this layer the "active layer" or "active region".

As was described before, the bulk heterojunction structure and the fact that mixing n-type and p-type materials in the same layer would dramatically increase the chance of converting an exciton into a pair of a free electron and hole, leading to a 5 to 7% increase in the efficiency of the device. Figure 42 shows the band diagram of a bulk heterojunction organic solar cell (BHOSC).

The properties of a planar BHOSC with its band diagram shown in Figure 42 are as follows: a standard ITO substrate covered by glass, covered by a 40nm thick layer of poly (3, 4 ethylenedioxythiophene) mixed with poly (styrenesulfonate) which also can be called by the abbreviation "PEDOT: PSS". PEDOT: PSS layer is the spacer which is located between the active region to prevent excitons from clinching in the interface of electrode and the active layer.

In the case of the active layer interface with the metallic electrode a very thin layer of the active layer will be depleted due to electrochemical phenomena happening at the metal-organic interface (this will be discussed in more details in the final section) which can act as a spacer [42].

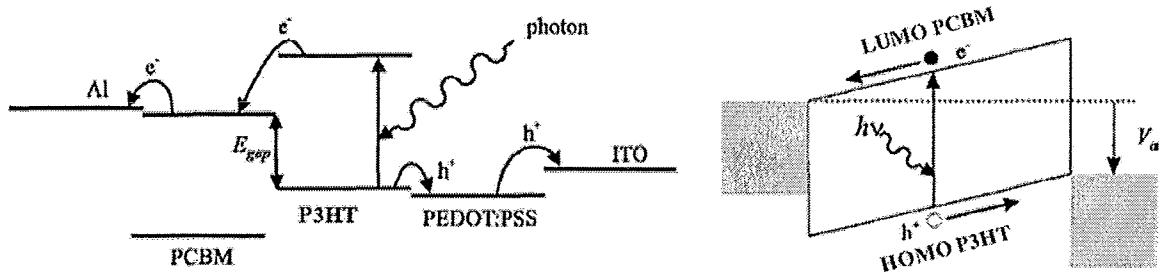


Figure 42: The band diagram of a bulk heterojunction OSC.

The next layer is called the active layer and is composed of Poly(3-hexylthiophene) (P3HT) and [6,6]-phenyl C61-butyric acid methyl ester (PCBM) with a ratio of 3:2wt. The reason to choose these materials is that using them, some of the most efficient organic solar cells can be fabricated [43].

In this combination P3HT, has the most absorption of light (because of bigger imaginary components in its refractive indices for the higher wavelengths) and therefore higher rate of exciton generation, but PCBM have a higher mobility. Therefore while the P3HT islands are absorbing most of the light and generating excitons, the PCBM around them act as an electron collecting network. This device is fabricated by M. Glatthaar et al. [41]. They used spin coating of 3:2wt solution of P3HT and PCBM from o-dichlorobenzene solution to deposit an 80nm thick layer. Finally, the last layer is a 100nm thick layer of Aluminum (Al), which is deposited with a rate of 2 nm/s, under 1×10^{-3} Pa via vapour deposition.

For the electrical model, because of simplicity in the geometry which represents a one-dimensional (1D) electrical problem, a 1D model would be sufficient. Therefore, the following is a description of a 1D COMSOL multiphysics model for a self consistent loop between a 1D Poisson equation and two sets of a 1D continuity equations for electrons and holes separately, as:

$$-\nabla \cdot \epsilon \nabla V = q(p - n) \quad \text{Equation 49}$$

$$\nabla \cdot (-D_n \nabla n + n \mu_n E) = G - R \quad \text{Equation 50}$$

$$\nabla \cdot (D_p \nabla p + p \mu_p E) = G - R \quad \text{Equation 51}$$

The model that is used is based on the following assumptions:

- The generated excitons are separated right after absorption inside the active region and the numbers of the generated electron-hole pairs are directly imported into the continuity equations as the generation rate (G in Equation 50 and Equation 51).
- The transport properties of the organic materials can be totally modeled by mobility, DOS, bimolecular recombination term and doping levels.
- The connections between different layers follow the physical rules of heterojunction connections between conventional semiconductors interfaces.

In the first step, the Poisson equation (Equation 49) is solved. For the first iteration, the distribution of charges can be found from the equations:

$$n = n_i e^{\frac{q\psi + \chi + \frac{E_G}{2}}{kT}} \quad \text{Equation 52}$$

$$p = n_i e^{-\frac{q\psi + \chi + \frac{E_G}{2}}{kT}} \quad \text{Equation 53}$$

The boundary conditions for the Poisson equation are:

- Continuity in internal boundaries (organic layers interfaces with each other)
- Fixed potentials at the interface of organic materials and electrodes, follow the ohmic connection condition:

$$\psi = V_a - \chi - \frac{E_G}{2} + \frac{kT}{q} \ln \left(\frac{\frac{N_{doping}}{2} + \sqrt{\left(\frac{N_{doping}}{2}\right)^2 + n_i^2}}{n_i} \right) \quad \text{Equation 54}$$

In Equation 54, V_a is the applied voltage at the contacts, E_G is the active layer's bandgap, N_{doping} is the dopands density and n_i is the intrinsic carrier density.

Two different COMSOL's packages were used to solve the Poisson equation:

- PDE coefficient form, stationary analyses package (the one that have been used for the three dimensional solution of wave propagation)
- Classical PDE, Direct Poisson solver

Both of the mentioned packages have the same result, and for our case none of them has any processing advantage over the other one (Figure 43).

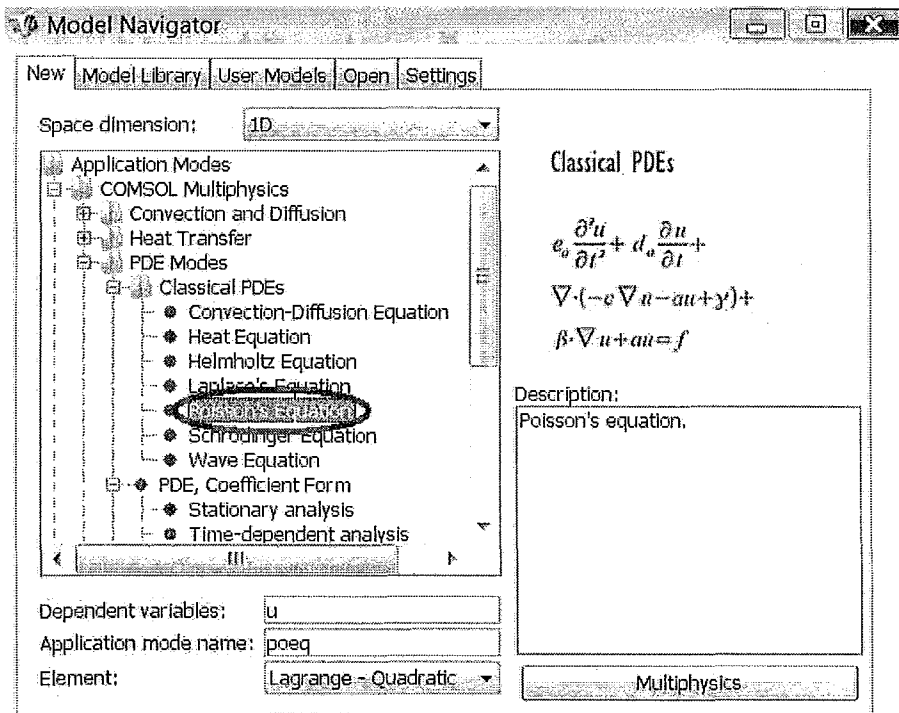


Figure 43: Depiction of the Poisson equation package root in the first window of the COMSOL simulator for the one

dimensional model.

In the previous sections (two and three dimensional optical simulation) COMSOL software could have been used in the single phenomenon mode. But for the electrical modeling, due to the calculation in two separate physical phenomena (the Poisson equation and the continuity equations), COMSOL should be used in its multiphysical mode. Therefore, at the beginning and in the model definition procedure, the Multiphysics option (which can be seen in the right-bottom corner of Figure 43) should be selected. In the case of the Multiphysics simulation, all of the packages that are supposed to be used in a multiphysical interaction with each other, should also be chosen at the beginning. Unfortunately, COMSOL's model doesn't have the modification ability after their generation. Therefore, all of the mentioned steps should be followed precisely or the whole model should be redefined.

The other two equations, which are solved in a closed loop with the mentioned Poisson equation, are two separate continuity equations (Equation 50 and Equation 51), one for the electrons and one for the holes. The flowchart of the electrical model using the mentioned equations can be seen in Figure 44.

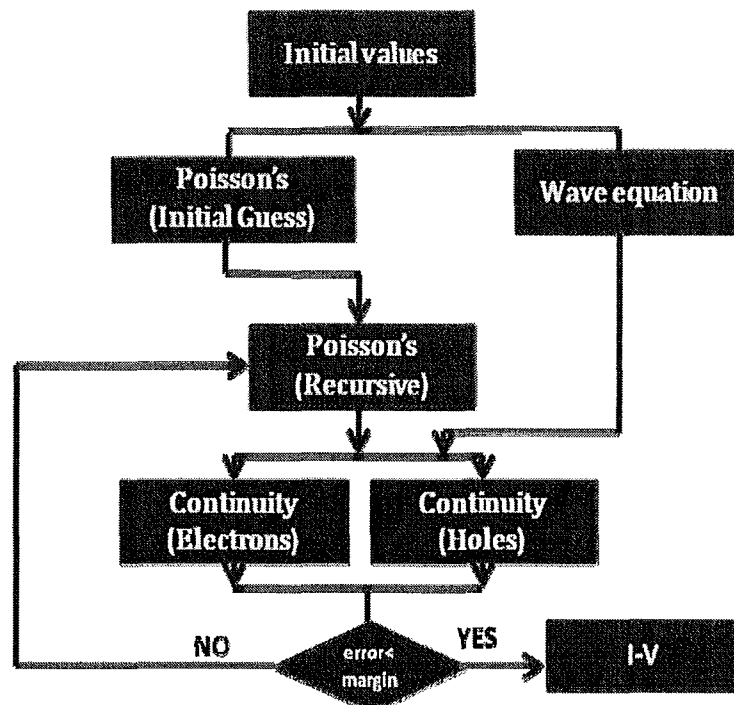


Figure 44: Flowchart of the electrical model.

As it can be seen in Figure 44, there are two Poisson equation solvers. The only difference between these Poisson solvers is their initial conditions. As was mentioned before, getting convergence in a closed loop of the Poisson equation and continuity equation, when the modeled semiconductor has characteristics similar to the characteristics of organic materials, is really hard and needs lots of iterations. Therefore, having a correct initial value will reduce the number of iterations.

The goal of having the first Poisson equation is to provide an efficient guess for initial value of voltage at any point in the device for the second Poisson solver. However, its own initial value is assumed to be defined by the following equation:

$$V_{init} = V_t(-\log(p_{init}/n_i) \times (N_{doping} < 0) \dots + \log(n_{init}/n_i) \times (N_{doping} \geq 0)) - X - 0.5 \times E_g \quad \text{Equation 55}$$

In the Equation 55, $V_t = (q/kT)$ is the thermal voltage, E_g is the bandgap, X is the electron affinity and N_{doping} is the doping concentration. Also, p_{init} and n_{init} stand for charge concentrations at the interfaces of the active layer and the electrodes, which can be calculated from the following equations:

$$n_{init} = \left(|N_{doping}| / 2 + \sqrt{(N_{doping}^2 / 4 + n_i^2)} \right) \times (N_{doping} \geq 0) \dots + n_i^2 / \left(|N_{doping}| / 2 + \sqrt{(N_{doping}^2 / 4 + n_i^2)} \right) \times (N_{doping} < 0) \quad \text{Equation 56}$$

$$p_{init} = \left(|N_{doping}| / 2 + \sqrt{(N_{doping}^2 / 4 + n_i^2)} \right) \times (N_{doping} < 0) \dots + n_i^2 / \left(|N_{doping}| / 2 + \sqrt{(N_{doping}^2 / 4 + n_i^2)} \right) \times (N_{doping} \geq 0) \quad \text{Equation 57}$$

Here, the doping concentration concept is slightly different than conventional semiconductors. In both cases the doping concentration and the Fermi level have a close relationship. In conventional semiconductors, the Fermi's level moves up or down by increasing or decreasing the number of electrons. The same rule is true for organic semiconductors, except that instead of adding a new material as the dopant to change the intrinsic balance of carriers, this change can be

obtained by change in the weight ratio [53] or in the synthesis temperature [54] or the annealing time [55, 56].

The next section is to model the continuity equations (Equation 50 and Equation 51). The package that is going to be used for this section is the steady-state analysis of convection and diffusion, shown in Figure 45.

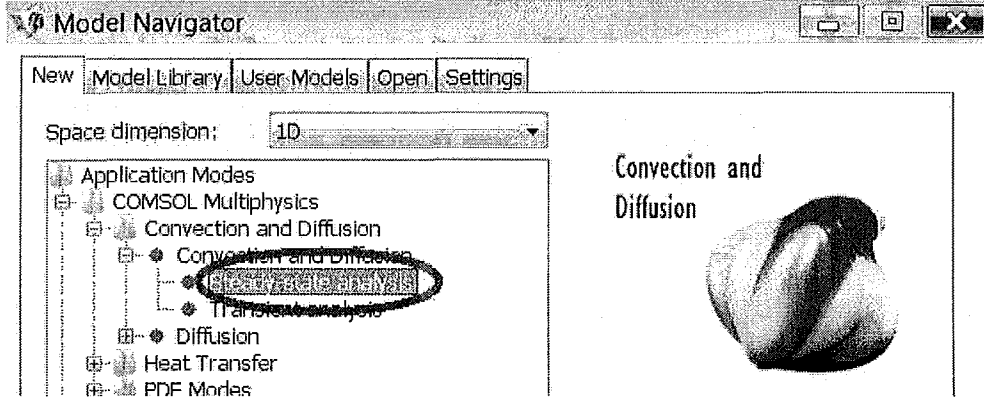


Figure 45: Picture of Steady-state analysis of convection and diffusion at the opening window of COMSOL.

It was assumed that the electrons and holes have separate continuity equations with the same generation (G) and recombination rate (R). G comes from the optical section and R is calculated via bimolecular recombination term [41]:

$$R = \beta n(x) p(x) \quad \text{Equation 58}$$

In Equation 50 and Equation 51, μ_n and μ_p stand for the electron and hole mobilities. Also D_n and D_p refer to carrier diffusivities which can be defined as below:

$$D_{n/p} = V_t \times \mu_{n/p} \quad \text{Equation 59}$$

The boundary conditions for the continuity equations are defined by Equation 56 and Equation 57. Charge densities initial values are also defined by Equation 52 and Equation 53. Having defined all of the mentioned in the scalar expression window in COMSOL Multiphysics, it is time to define the rest of the required coefficients (Table 9).

Having all of the parameters and boundary conditions properly defined, it is necessary to define the modeling algorithm using MATLAB coding or solving script inside the COMSOL Solver Manager. The algorithm shown in Figure 44 can be seen through the following script:

```

“ init = asseminit(fem);
fem.sol=femstatic(fem, ...
    'init',init, ...
    'solcomp',{ 'phi0' }, ...
    'outcomp',{ 'phi0' }, ...
    'maxiter',250000000);
fem0=fem;

init = asseminit(fem,fem0.sol);
fem.sol=femstatic(fem, ...
    'init',init, ...
    fem0.sol, ...
    'solcomp',{ 'lm3', 'phi', 'pc', 'nc', 'lm4' }, ...
    'outcomp',{ 'lm3', 'phi', 'pc', 'lm4', 'nc' }, ...
    'pname', 'Vd', ...
    'plist',[-1.3:0.005:-1.2  -1.19:0.01:0  0.02:0.02:0.6  0.65:0.05:1.6], ...
    'maxiter',250000000, ...
    'hnlin', 'on');
fem0=fem”;

```

In the first part of the above script (*fem0=fem*), the first line:

```
“ init = asseminit(fem);”
```

assigns the initial values to the information that have been already provided through the constant window and the scalar expression window. The second line is the beginning of static analyses. The third line calls the initial values and the fourth line defines set of equations that should be

solved. At this point, it will solve “*phi0*”, which stands for the name of the first Poisson’s equation variable. The first Poisson equation is going to be solved to give an adequate first guess for the second Poisson equation’s initial value.

Table 9: Parameters that have been used in Figure 46.

Models Parameters	Our COMSOL Model	Glatthaar & et. al. [41]
Density of states	$4 \times 10^{20} \text{ cm}^{-3}$	$5 \times 10^{20} \text{ cm}^{-3}$
Electron and hole mobility	$1 \times 10^{-4} \text{ cm}^2/(\text{V.s})$	$1 \times 10^{-4} \text{ cm}^2/(\text{V.s})$
p-doping level	$2 \times 10^{16} \text{ cm}^{-3}$, $8 \times 10^{16} \text{ cm}^{-3}$, $2.4 \times 10^{17} \text{ cm}^{-3}$	$1 \times 10^{16} \text{ cm}^{-3}$, $4 \times 10^{16} \text{ cm}^{-3}$, $1.6 \times 10^{17} \text{ cm}^{-3}$
Dielectric constant	3.8	3.8
active region’s LUMO (PCBM’s LUMO)	4.3 eV	4.3 eV
active region’s HOMO (P3HT’s HOMO)	5.2 eV	5.2 eV
Contact work function for the n-contact (Cathode)	4.1 eV	4.1 eV
Contact work function for the p-contact (Anode)	5.0 eV	5.0 eV

The next line stands for the variable that is going to be reported in the output. The sixth line shows the maximum number of iterations before reaching convergence with the default error smaller than 10^{-16} . Finally, the last line of this part, stores all of the reported variables in all of the mesh points.

The second part is related to the closed loop of the Poisson equation and the continuity equation. For the second part, term “*init = asseminit(fem,fem0.sol),*” indicates that for this section the

initial value is assigned by the value provided in the constant window, the scalar expression window and the previous section output.

As is indicated in the following two lines of script, the variables that are going to be solved in this section are *'lm3','phi','pc','nc','lm4'*. *'phi'*, *'pc'* and *'nc'* refer to main variables of the second Poisson equation (*phi*=voltage in each point of mesh), the continuity equation for holes (*pc*=concentration of holes) and the continuity equation for electrons (*nc*=concentration of electron).

The next line (*'pname','Vd', etc.*), indicates that parameter V_d which is the applied voltage at the anode is a variable with different values which are assigned in the next line by:

'plist',[-1.3:0.005:-1.2 -1.19:0.01:0 0.02:0.02:0.6 0.65:0.05:1.6], ...

This line of script says, COMSOL should be solved for different values of V_d that are started from -1.3eV and increased by steps of 0.005eV up to -1.2eV, then the steps will change to a higher value of 0.01eV from -1.19eV to 0eV and so on. The reason of choosing the parameter value like that is to have smaller steps at the beginning of the first couple of iterations. It will also decrease the time of simulation by increasing the steps comparing to a simple ramp.

The final line *"'hnlm','on'"*, turns on the highly nonlinear solver. This will reduce the time of simulation and also changes the method of guessing the next damping coefficients from a Newton method to an adaptive algorithm.

For the described model, the following assumptions are implied:

- The generated excitons are separated right after absorption inside the active region and the numbers of the generated electron-hole pairs are directly imported into the continuity equation as the generation part (G in Equation 50 and Equation 51).
- The transport properties of the organic materials can be completely modeled by mobility, DOS and bimolecular recombination rate.
- The connections between different layers follow the physical rules of heterojunction connection between conventional semiconductors interface.

3.2.1.2. Drift-Diffusion Model, Results and Discussion

One way to make sure that the developed model is working perfectly is to find a reported data with a similar approach to the described model (one dimensional recursive loop of the Poisson and continuity equations). Figure 46 shows the comparison of the described model and Glatthaar & et. al. [41].

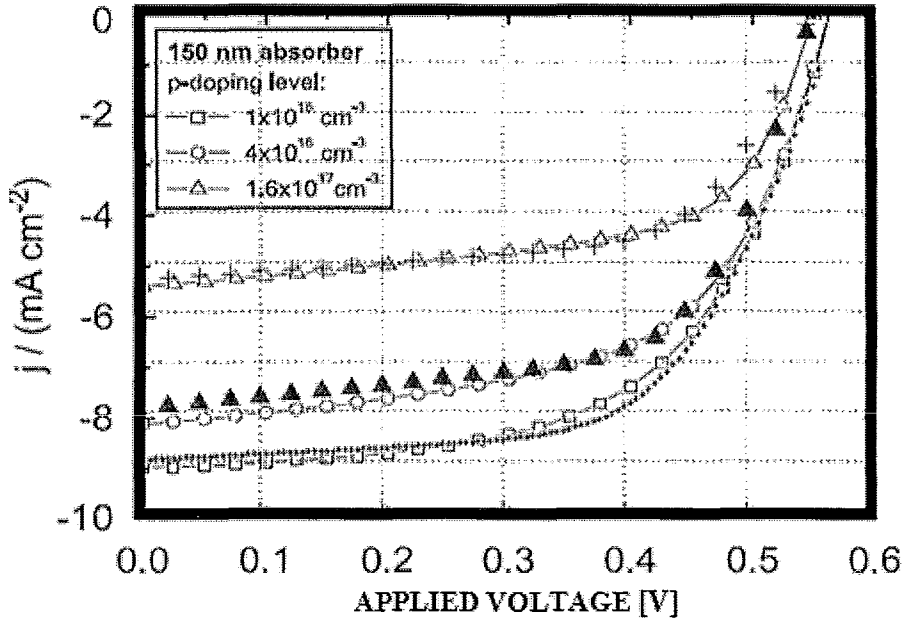


Figure 46: Comparison of my COMSOL simulation and simulation results from [41]. The curves with (+, ., Δ) are the result of my simulation and the ones with (Δ, o, □) at the background are the result of Glatthaar & et. al. [41]. The parameters for both of the cases are demonstrated in Table 9.

Assuming the mentioned considerations, we have a simple model of a one dimensional device depicted in the right side of the Figure 42. Comparing the simulation result and experimental data a clear difference in the form of I-V curve can be observed. This dissimilarity is in the form of a kink in the middle of I-V curve which decreases the filling factor of the organic solar cell and decreases the open circuit voltage. As a possible suggestion from [41] which is supported by experimental data by Pandey et. al. [56], this phenomenon is named the counter diode.

Figure 47 shows a comparison between experimental results of a planar organic solar cell (Left) and the results from numerical modeling of the forward biases (Right). As it can be seen, the real I-V curve shows lower open circuit voltage as well as lower fill factor. It should be noted that this difference is not due to the flaws inside the drift-diffusion modeling (because as Figure 46

suggest for a similar case, the result of our simulation has a very good match with the reported I-V curve by Glatthaar & *et.al.* [27]).

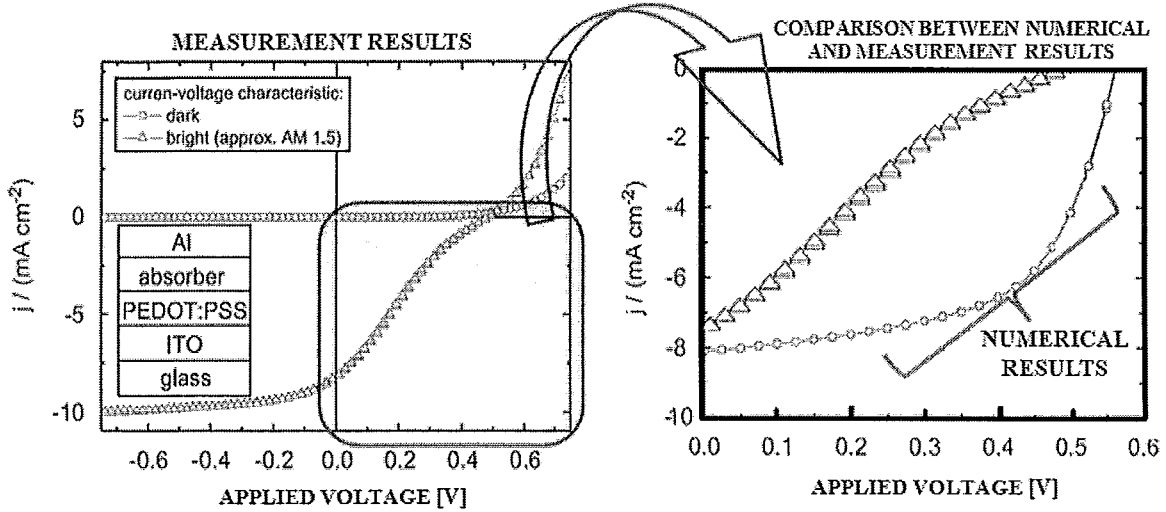


Figure 47: Measurement result of I-V curve from [41] (left) compared to the numerical results (right).

The experimental result of [41] shows a strange shape for an I-V curve of a solar cell. The I-V curve of an ordinary solar cell should be like what is reported in Figure 46, which is an exponentially increasing curve not an S-shape (counter S) curve. As it is described by Ahlswede & *et.al.* in [59] and by Hanisch & *et. Al.* in [60] and also mentioned by Glatthaar & *et. al.* in [41], this peculiarity in form is due to a phenomenon which is called counterdiode effect. Counterdiode effect is a result of introduction of a depletion layer created at the interface of metallic electrode and active layer. The counterdiode effect can be reduced by using a less destructive method of metal deposition (such as thermal evaporation instead of sputtering [60]) during the process of fabrication.

In the following section the effect of counterdiode is discussed in more details, and a numerical model based on quantum tunneling analyses is introduced to be added to the COMSOL model, so that, it creates a more accurate numerical model.

3.3. THE CORRECTION OF ELECTRICAL MODEL USING TUNNELING CURRENT

In this section, it is tried to find a proper explanation for the difference between experimental and numerical results. The I-V curve of a diode and ordinary solar cells and their equivalent circuits are shown in Figure 48. Also Figure 49 shows how an I-V curve similar to the experimental result (shown in Figure 47), can be made by adding the current of an ideal solar cell to the output current of a shunt diode.

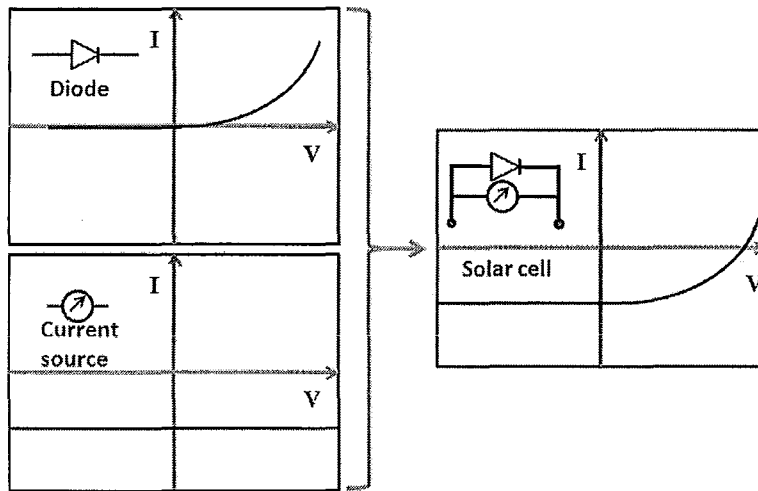


Figure 48: I-V curve of a diode, a current source and their parallel combination that makes a solar cell.

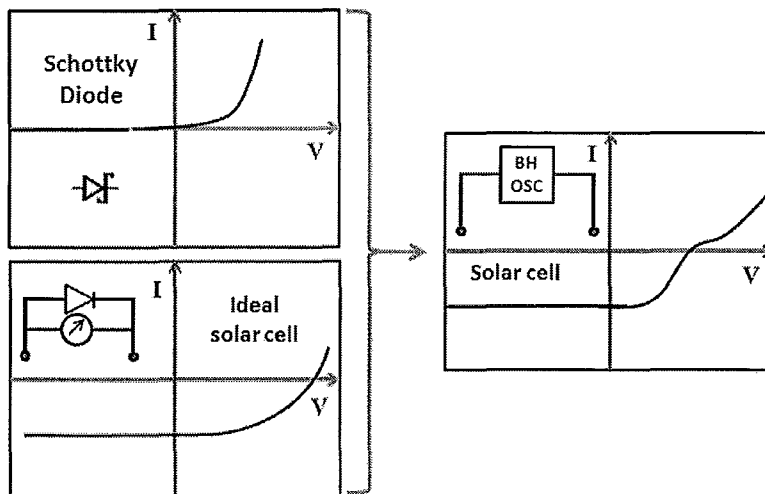


Figure 49: The result of an ordinary solar cell and a parallel diode which will result into a I-V curve of a device similar to a BH-OSC by including the effect of tunneling current (the counterdiode effect).

The term “counterdiode” was originally used for light emitting diodes (LEDs) that were used in high frequency (which are mostly used in fiber optics). In this case, to increase the frequency of the optical pulse generated by LED or simply shrinking the width of the pulses, the Zener diode would be used to discharge the inside capacitance of LED to make it ready for the next pulse. In the case of no counterdiode, this capacitance will be discharged through the leakage that will take a long time [61].

In the case of organic solar cells, the counterdiode phenomenon is also due to a shunt diode which is connected in parallel to the solar cell, with the following major differences:

- Despite the name, as can be seen in the schematic model that is shown in Figure 49, the shunt diode has the same direction of the solar cell’s diode.
- Unlike the LED circuit, in the case of BH-OSC, there is actually no real shunt diode connected in parallel with the device and this is just the equivalent model.

Here, physical phenomenon behind this “counterdiode” effect must be described. Prior to this description, we should take a closer look at the junction of the metallic electrode and active layer. While the metallic electrode is getting deposited on top of the organic blend (in our case Aluminum), because of the high rate of activity in freshly deposited aluminum atoms, the weak Vanderwall’s bound between the first couple of layers of organic material, will break and this will results in surface states in the middle of the active layer’s bandgap [31,64].

On the other hand, in an organic-metal junction the first couple of molecular layers at the interface lose their charges, just like a conventional semiconductor-metal junction. For the conventional junction those charges will be replaced by the charges nearby, because of the electrical connection in the semiconductor’s lattice. However, in organic material, apart from very high or very low energies, most of the energy states are local. Therefore, if they get depleted by the metallic electrode at the junction, there will be no flow of nearby charges to replace them. This will result in a very thin layer that has a wider bandgap, similar to an insulator. Thus, as shown in Figure 50, the band diagram of an organic solar cell should be modified by adding an insulator layer at the junction [66].

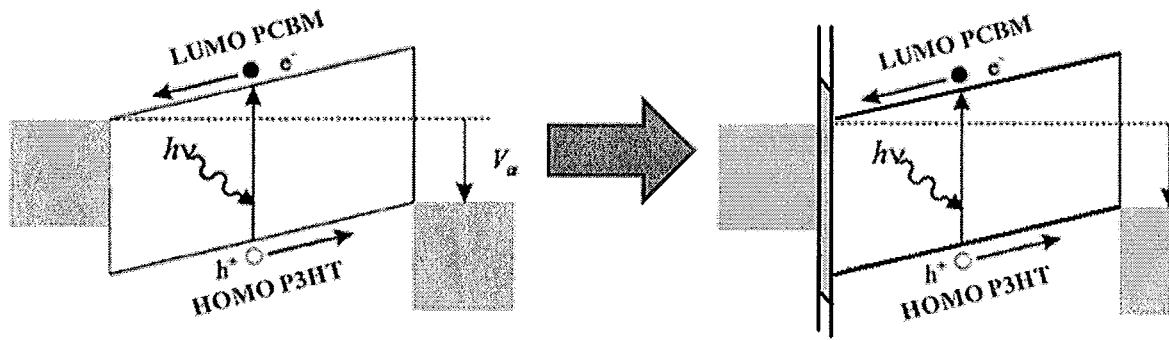


Figure 50: Difference in the band diagram of the solar cell with (Right) and without taking the counterdiode effect into account (Left).

Figure 51 shows the band diagram of the device in different biases and the direction of the current. The red arrows show the direction of tunneling of electron through the barrier between cathode and active regions, while the blue arrows stand for the direction of carrier flow in the drift diffusion process. Four regions of I-V curve in the picture are as below:

- A) High reverse biases: In this region the major transport process is the thermionic emission
- B) Low reverse biases and the onset of forward bias: In this case by increasing the biasing voltage, the barrier starts to prevent electrons to easily pass through the junction and a small chance of tunneling for electrons from the organic side to the electrode
- C) In the forward bias but still less than the open circuit voltage: In this region, we still have the photogenerated current, but the tunneling current really starts to kick in. This region can be attributed to the I-V curve after the Schottky diode in Figure 48 turns on.
- D) After the open circuit voltage: both of diodes in Figure 48 (Schottky and solar cell diode) are turned on in this condition.

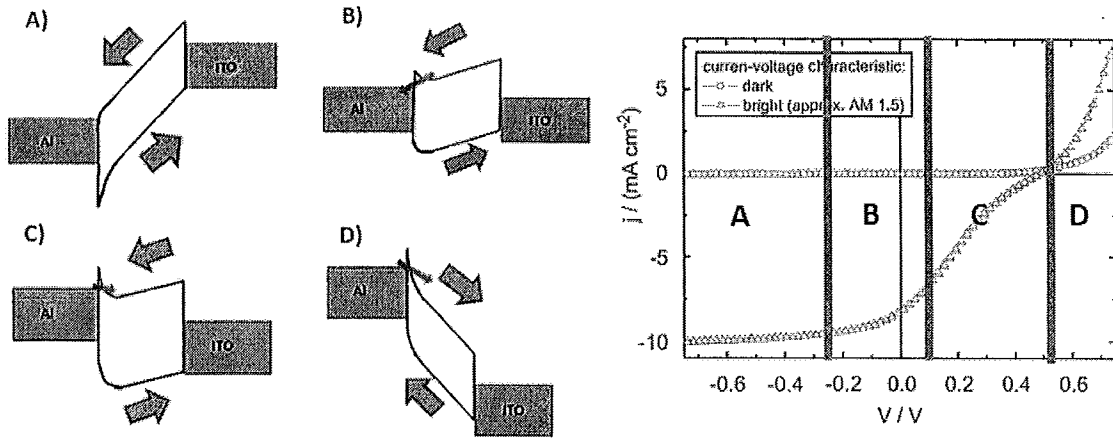


Figure 51: Band diagram of a solar cell for different biasing and the direction of the current. Blue arrows stand for the direction of the carrier due to the thermionic emission and the red arrows show the direction of electron tunneling the barrier at the interface (at the left). The experimental result from [41] with separated region in the bias for each one of the four conditions at the left.

Consequently, the total current can be divided into the following sections:

- 1- Thermionic emission current
- 2- Tunneling from the organic layer to the metallic contact
- 3- Tunneling from the metallic contact to the organic layer

The first part was calculated in the previous section. The second current is mostly in the reverse biases that are important for us. The most important parameters for organic solar cells' fill factor (fill factor or FF is the ratio of maximum generated power to product of short-circuit current and open circuit voltage) and efficiency, can be calculated by the information that is provided in the region C of Figure 51, which is the same region that the third current exists.

The current density passes through a thin barrier can be calculated by the following equation [66]:

$$J = q \iint \rho(E, p_x) f(E, p_x) T(p_x, V) dE dp_x \quad \text{Equation 60}$$

In this equation, q stands for electron charge, ρ is the distribution of charges, f is the Fermi's function, p_x is the momentum of electron in the direction of x and T is the transport coefficient.

In 1998, Schuegraf and Hu solved this equation for thin barriers between two different materials and they came up with the following formula for direct tunneling [67]:

$$J = \frac{q^3 m_{eff}}{8\pi m_{diel} h q \Phi_B B_1} E_{diel}^2 \exp\left(-\frac{4\sqrt{2m_{diel}} (q\Phi_B)^3 B_2}{3\hbar q E_{diel}}\right) \quad \text{Equation 61}$$

where B_1 and B_2 are defined as:

$$B_1 = \left(1 - \left(1 - \frac{qE_{diel}t_{diel}}{q\Phi_B}\right)^{1/2}\right)^2 \quad \text{Equation 62}$$

$$B_2 = \left(1 - \left(1 - \frac{qE_{diel}t_{diel}}{q\Phi_B}\right)^{3/2}\right) \quad \text{Equation 63}$$

For triangular barriers, we have $B_1=B_2=1$ [65]. In the above equations m_{eff} is the effective mass of the electron inside the metallic electrode, m_{diel} is the effective mass of electron inside the dielectric, h is the Planck constant, Φ_B is the difference between the work function of metal and the LUMO of the organic layer, t_{diel} stands for the width of the barrier layer and E_{diel} is the electrical field inside the barrier which can be calculated as below:

$$E_{diel} = \frac{(\phi_m - V_{LUMO} + V_a)}{t_{diel}} \quad \text{Equation 64}$$

Where Φ_m is the work function of the metal, V_{LUMO} is the location of the organic layer's LUMO and V_a stands for the applied voltage.

Subtracting the experimental and numerical results and assuming that the difference is due to the tunneling current, the characteristics of the barrier can be extracted. Figure 52 shows the difference between the experimental and numerical results. In the beginning of I-V curve represented in Figure 52, the current's curve has an exponential form.

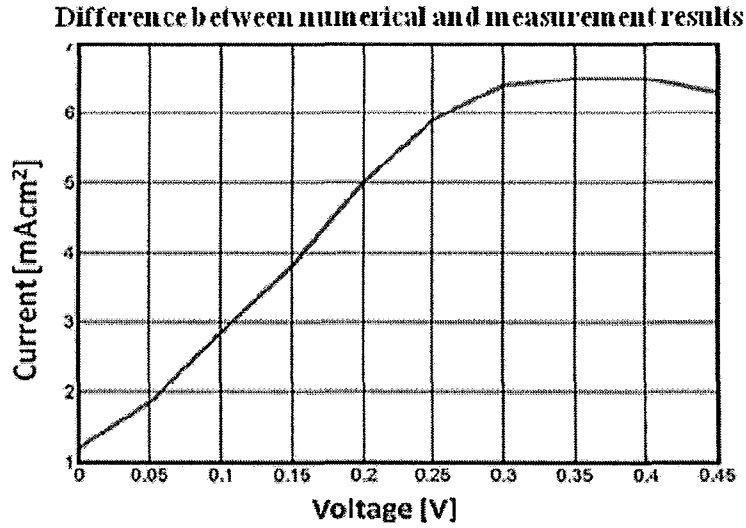


Figure 52: The difference between the experimental I-V curve and numerical result that are shown in Figure 47

Based on the above, the tunneling current formula as a function of applied voltage on Al becomes as below:

$$J_{tunneling} = \begin{cases} \frac{q^3 m_{eff}}{8\pi m_{diel} \hbar q \Phi_B B_1} E_{diel}^2 \exp\left(-\frac{4\sqrt{2m_{diel} (q\Phi_B)^3 B_2}}{3\hbar q E_{diel}}\right) & \text{for } 0 < V < X \\ J_{tunneling}(0.3) & \text{for } X < V \end{cases} \quad \text{Equation 65}$$

To find the best fit with the curve in Figure 52, two parameters can be used:

- The barrier height
- The barrier width

By changing the barrier's width, the resistance of the interface layer changes which leads to changes in slope of the I-V curve (by increasing the thickness I-V curve becomes more nonlinear). By increasing/decreasing the barrier's height, the magnitude of the current, dramatically decreases/increases. Figure 53, shows the curves of the modified tunneling current for three different barrier thicknesses (10nm, 7nm and 3nm) with forty different heights of the barrier distributed from 1eV to 2eV.

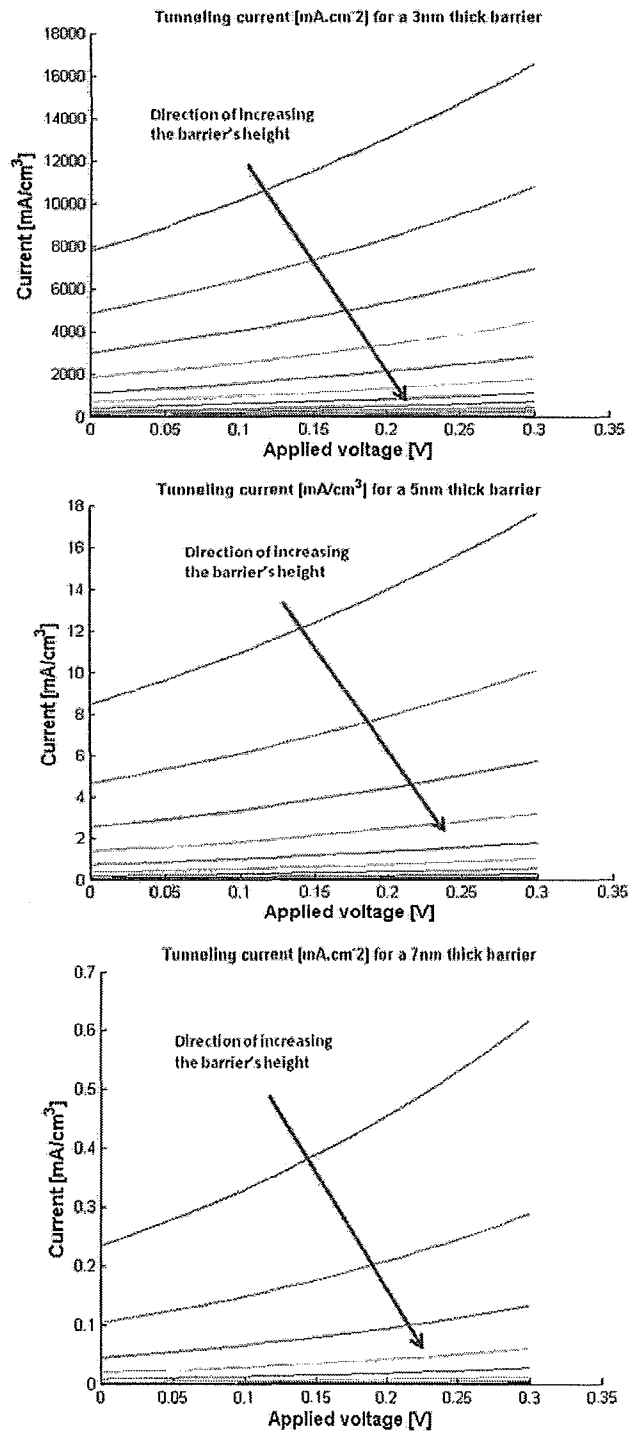


Figure 53: Modified tunneling current for three different barrier widths (3nm, 7nm and 10nm) with forty different barrier heights from 1eV to 2eV. The direction of the red arrows in the pictures indicates the increase in the barrier height.

Finally by comparing different results of the modified tunneling current, the best match can be found with the parameters that are shown in Table 10. Figure 54 shows comparison between the experimental and the best matches in the first and the second (modified) tunneling current model.

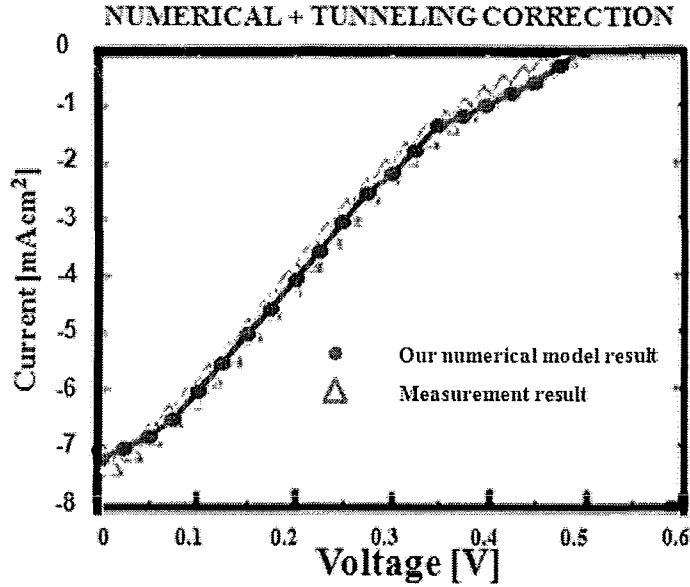


Figure 54: Comparison of calculated I-V corrected by tunneling current (circles) with measurement results reported by Glatthaar *et. al.* [41] (triangles).

As Figure 54 shows, the comparison of numerical result (which is modified by the tunneling current correction) have a good agreement with the experimental result.

Table 10: Parameters that are used in Figure 54

Parameter's symbol	Parameter's quantity	Equation
m_{eff}/m_{diel}	1.6	Equation 65
Φ_B	1.89eV	Equation 65
t_{diel}	5.56nm	Equation 64

After finding the proper fit for the tunneling current, the question come into mind that “how should the two of the current be combined to produce the final result? “. By taking a look at Figure 51, it becomes clear that tunneling current is injecting electrons into the active region (in section *C* and *D*) or taking out electrons from the active region (in section *B*). Therefore, tunneling current acts as the generation or recombination in Equation 50 and Equation 51 and we can rewrite them as:

$$\nabla \cdot (-D_n \nabla n + n \mu_n E) = G - R \pm J_{tunnelling} / q \quad \text{Equation 66}$$

Therefore, it seems that the whole COMSOL model should be done again. On the other hand, the generation and recombination quantities are in order of 10^{25} while the maximum number of tunneling current's number of electron is close to 10^{16} . Consequently, the tunneling current term can be ignored and the total current can be calculated by the simple summation of the tunneling and the COMSOL modeling results.

CHAPTER 4

CONCLUSION AND RECOMMENDATION

4. CONCLUSION AND RECOMMENDATION FOR FUTURE WORK

4.1. CONCLUSION

In this thesis, the mechanism of conversion of optical power to electrical power for two types of organic solar cells (bilayer and bulk heterojunction solar cells) was studied.

In order to model organic solar cells, the thesis was divided into two separate sections:

- Optical section (Chapter 2)
- Electrical section (Chapter 3)

In the optical section, the following mechanisms were studied:

- In-coupling of the photons
- Absorption of the photons
- Formation of the excitons

In Chapter 2, it was discussed that COMSOL software can be successfully used to model the propagation of light inside an organic solar cell. Also, it was shown that by adding an extra layer focusing apertures at the top of planar bilayer heterojunction organic solar cells, the absorption of light around the active layers' junction, which is a vital area for power conversion inside such solar cells, can be increased up to 98%.

In the next section of the thesis, the electrical performance of the organic solar cell for the following mechanisms was studied:

- Diffusion of the excitons

- Dissociation of the excitons into electrons and holes and the transportation of the charges
- Collection of the charges at the electrodes

By a comparison between experimental and electrical model results, it was concluded that a simple drift diffusion model that only considers the thermionic emission mechanism as the only component of generated photocurrent in a bulk heterojunction organic solar cell is not sufficient by itself. Thus there is a need for a new model to include the effect of charge injection at the electrodes' interfaces. Therefore, a tunneling current correction was introduced. By finding the best fit using trial and error, connection of organic material and metallic electrode was characterised.

It should be noted that the mentioned tunneling current or the so called “counterdiode effect” in the field of organic devices had been studied only for organic LEDs in the literature and by modeling the counterdiode effect via tunneling current model for the organic solar cells the last section can be attributed as a contribution to the literature.

4.2. RECOMMENDATION

For the future work, on the optical modeling of organic solar cells, two different approaches are suggested:

- Modeling new applications using the presented models
- Developing new models based on the present work

In the case of new applications, new types of focusing deformities or new designs of organic solar cells (for instance, changing the order of the layers or adding new layers with new types of organic or inorganic materials) can be proposed. Another interesting structure is an organic solar cell with two metallic electrodes, where one of the sides has some holes in it to allowing the sunlight into the device and to be trapped there. To increase the intensity of light inside of the solar cell, some focusing deformities at the top layer can be used.

Also, studying the effect of a photonic crystal at the first layer of organic solar cells to increase the absorption and reduce the back reflection of light by the existing three dimensional optical model is possible.

For developing new models, upgrading the one dimensional analytical model into two and three dimensional models or creating a new numerical model for bulk heterojunction organic solar cells based on the existing numerical models, this time by including a detailed model, which consist of nanometeric islands of one type of organic material inside another type of organic material, is strongly suggested.

Similar to the optical recommendations, for the future electrical models suggestions can be divided into the two following group:

- Modeling new applications using the present models
- Developing new models based on the present work

For the first category (new applications), new types of planar organic solar cells such as folded structure or multistage planar organic solar cells can be modeled using the proposed electrical model. These types of organic solar cells have a better efficiency, because of their better light absorption ability, but because of their multilayer design the electrical properties of them is deteriorated. Therefore, modeling can be helpful for improving the electrical design to get even better performances for these multilayer OSCs.

For the second category, new methods of transport modeling for organic materials can be developed. These methods may include more complicated quantum mechanical analyses. For example, *ab initio* methods and the Hartree–Fock method for a very accurate molecular model and true modeling the orbital distribution of electron. These accurate methods can be used for the prediction of molecular scale (some nano meter) phenomena such as connections and interfaces. However, because of high computational cost to model larger devices, it is better to use other quantum mechanical analyses such as density functional theory (DFT), which is a good quantum mechanical method for devices around the ranges of planar organic solar cells (a few 100nm). DFT analysis is usually compound with Non-equilibrium Green's function (NEGF) method, which is a good computational approach to solve the Schrödinger's equation for similar devices.

REFERENCES

- 1- A. J. Waldau, *"PV Status Report 2003"*, European Commission, EUR 20850 EN, 2003.
- 2- *"Report on new trends in Solar cells"*, The U.S. National Renewable Energy Laboratory (NREL), 2010, Available: <http://www.nrel.gov/>.
- 3- Annual report, *"Next-Generation Organic Solar Cell Technology and Market Forecast"*, Displaybank Co. Ltd, Feb 2010.
- 4- L. Kazmerski, *"NREL compilation of best research solar cell efficiencies"*, National Renewable Energy Laboratory, National Renewable Energy Laboratory (NREL), 2010.
- 5- F. C. Krebs, *"Fabrication and processing of polymer solar cells: A review of printing and coating techniques"*, Solar Energy Materials & Solar Cells, Vol. 93, pp. 394–412, 2009.
- 6- M. Haeussler, *"Fabrication of organic photovoltaic devices"*, article in *"A to Z of nanotechnology"*, Oct 25, 2009.
- 7- E. Becquerel and L. Lumiere: *"Ses causes et ses effets"*, tome second, Paris, pp. 122. 1867.
- 8- H. Hertz, *"Uber eine Anfluss des ultravioletten Lichtes auf die elektrische Entladung"*, Annalen der Physik und Chemie, Vol. 31, pp. 983-1000, 1887.
- 9- *"The Nobel Prize in Physics 1921"*, Nobelprize.org, 26 Sep. 2010, Available: http://nobelprize.org/nobel_prizes/physics/laureates/1921/index.html.
- 10- J. Perlin, *"From space to earth: the story of solar electricity"*, Harvard University Press: Cambridge, MA, 2002.
- 11- P.M. Borsenberger and D.S. Weiss, *"Organic photoreceptors for imaging systems"*, Marcel Dekker, New York, 1993.
- 12- C. K. Chiang, C. R. Fincher, Y.W. Park, A. J. Heeger, H. Shirakawa, E. J. Louis, S. C. Gau and A. G. MacDiarmid, *"Electrical conductivity in doped polyacetylene"*, Physical Review Letters, Vol. 39, pp. 1098-1101, 1977.
- 13- H. Shirakawa, A. G. MacDiarmid and A. J. Heeger, *"Twenty-five years of conducting polymers"*, Chemical Communications, Vol. 1, pp. 1, 2003.
- 14- C. W. Tang, *"Two-layer organic photovoltaic cell"*, Applied Physics Letters, Vol. 48, pp. 183–185, 1986.
- 15- J. Li, *"Solarmer energy, Inc. breaks psychological barrier with 8.13% OPV efficiency"*, Solarmer Energy, Inc. 27 June 2010, Available: <http://www.forbes.com/feeds/businesswire/2010/07/27/businesswire142993163.html>.
- 16- S. S. Sun and N. Serdar Sariciftci, *"Organic Photovoltaics"*, Taylor & Francis Group LLC. 2005.
- 17- T. Kietzke, *"Recent advances in organic solar cells"*, Advances in OptoElectronics, Review Article, Hindawi Publishing Corporation, Vol. 2007, pp. 15, 2007.
- 18- T. L. Benanti, D. Venkataraman, *"Probing the chiroptical response of a single molecule: fluorescence detected circular dichroism from individual helicene molecules"*, Photosynthesis Research, 87, pp. 73–81, 2006.
- 19- H. Hoppea and N. S. Sariciftci, *"Organic solar cells: An overview"*, Journal of Materials Research, Vol. 19, pp. 7, 2004.

- 20- D. P. Grubera, G. Meinhardt and W. Papousek, "Modelling the light absorption in organic photovoltaic devices", *Solar Energy Materials and Solar Cells*, Vol. 87, pp. 215–223, 2005.
- 21- A. K. Ghosh and T. Feng, "Merocyanine organic solar cells", *Journal of Applied Physics*, Vol. 49, pp. 5982, 1978.
- 22- J. Wagner, T. Fritz, and H. Böttcher, "Computer modelling of organic thin film solar cells. I. exciton model of photocurrent generation", *Physica Status Solidi A*, Vol. 136, pp. 423, 1993.
- 23- A. De'sormeaux, J. J. Max, and R. M. Leblanc, "Photovoltaic and electrical properties of aluminum/Langmuir-Blodgett films/silver sandwich cells incorporating either chlorophyll a, chlorophyll b, or zinc porphyrin derivative", *Journal of Physical Chemistry*, Vol. 97, pp. 6670, 1993.
- 24- C. W. Tang and A. C. Albrecht, "Photovoltaic effects of metal-chlorophyll-a-metal sandwich cells", *Journal of Chemical Physics*, Vol. 62, pp. 2139, 1975.
- 25- A. K. Ghosh, D. L. Morel, T. Feng, R. F. Shaw, and C. A. Rowe, Jr., "Photovoltaic and rectification properties of Al/Mg phthalocyanine/Ag Schottky-barrier cells", *Journal of Applied Physics*, Vol. 45, pp. 230, 1974.
- 26- H. B. DeVore, "Spectral distribution of photoconductivity", *Physical Review*, Vol. 102, pp.86, 1956.
- 27- L. G. Yang, H. Z. Chen and M. Wang, "Improved method of determining exciton diffusion length from thickness-dependent photocurrent response of organic heterojunction", *Thin Solid Films*, Vol. 516, pp. 7701–7707, 2008.
- 28- L. A. A. Pettersson, Lucimara S. Roman, and Olle Inganäs, "Modeling photocurrent action spectra of photovoltaic devices based on organic thin films", *Journal of Applied Physics*, Vol. 86, pp. 487, 1999.
- 29- G. Z. Ran, W. Q. Zhao, G. L. Ma, L. Dai and G. G. Qin, "Role of the dielectric capping layer in enhancement of light outcoupling for semitransparent metal-cathode organic light-emitting devices", *Journal of Optics A: Pure and Applied Optics*, Vol. 8, pp. 733–736, 2006.
- 30- M. Niggemann, M. Riede, A. Gombert, and K. Leo, "Light trapping in organic solar cells", *Wiley-VCH - physica status solidi (a)*, Vol. 205, pp. 2862–2874, 2008.
- 31- N. K. Persson, M. S. and O. Inganäs, "Anomalous behaviour of the photoacoustic signal near the phase transition in the thallium blue bronze($Tl_{0.3}MoO_3$)", *Solar Energy Materials & Solar Cells*, Vol. 83, pp. 169–186, 2004.
- 32- R. J. Matson, K. A. Emery and R. E. Brid, "Solar Cells, Terrestrial solar spectra, solar simulation and solar cell short-circuit current calibration: A review", *Solar Cells*, Vol. 11, pp. 105–145, 1984.
- 33- COMCOL Inc. Available: <http://www.comsol.com/>.
- 34- M. Abkowitz et.al. "Springer Handbook of electronic and photonic materials", Springer, 2006.
- 35- Z.T. Liu, C.Y. Kwong, C.H. Cheung and A.B. Djurisi, "The characterization of the optical functions of BCP and CBP thin films by spectroscopic ellipsometry", *Synthetic Metals*, Vol. 150, pp. 159–163, 2005.
- 36- "Isotropic organic semiconductor for OPVs and OLEDs", Aldrich Chemical Co., Inc. Sigma-Aldrich Corporation, "Your Materials Matter." Data sheet, 2008.
- 37- J. D. Lindberg, R. E. Douglass and D. M. Garvey, "Carbon and the optical properties of atmospheric dust", *Journal of Applied Optics*, Vol. 32, pp. 21, 1993.
- 38- S. Laux, N. Kaiser, A. Zoëller, R. Goëtzmann, H. Lauth and H. Bernitzki, "Room-temperature deposition of indium tin oxide thin films with plasma ion-assisted evaporation", *Thin Solid Films* Vol. 335, pp.1–5, 1998.

- 39- R. Kashyap, *"Theory of fiber bragg gratings"*, Academic Press, London, 1999.
- 40- R. Loudon, *"The quantum theory of light"*, Oxford U. Press, Oxford, 1994.
- 41- M. Glatthaar, M. Riede, N. Keegan, K. Sylvester-Hvid, B. Zimmermann, M. Niggemann, A. Hinsch and A. Gombert, *"ITO-free wrap through organic solar cells—a module concept for cost-efficient reel-to-reel production"*, Solar Energy Materials and Solar Cells, Vol. 91, pp. 390–393, 2007.
- 42- A. Kahn, W. Zhao, W. Gao, H. Va'zquez and F. Flores, *"Doping-induced realignment of molecular levels at organic–organic heterojunctions"*, Chemical Physics, Vol. 325, pp. 129–137, 2006.
- 43- V. Dyakonov, *"Mechanisms controlling the efficiency of polymer solar cells"*, Applied Physics A, Vol. 79, pp. 21, 2004.
- 44- L. J. A. Koster, E. C. P. Smits, V. D. Mihailetschi, and P. W. M. Blom, *"Device model for the operation of polymer/fullerene bulk heterojunction solar cells"*, Physical Review B, Vol. 72, pp. 085205, 2005.
- 45- J. C. C. Fan, F. J. Bachner and G. H. Foley, *"Effect of O₂ pressure during deposition on properties of rf-sputtered Sn-doped In₂O₃ films"*, Applied Physics Letters, Vol. 31, pp. 773–775, 1977.
- 46- K. Sreenivas, T. Sundarsen Rao, A. Mansnigh and S. Chandr, *"Preparation and characterization of r.f. sputtered indium Tin oxide films"*, Journal of Applied Physics, Vol. 57, pp. 384–392, 1985.
- 47- J. Szczyrbowski, A. Dietrich and H. Hoffmann, *"Optical and electrical properties of r.f. sputtered indium-tin oxide films"*, Physica Status Solidi A, Vol. 78, pp. 243–252, 1983.
- 48- M. Buchanan, J. B. Webb and D. F. Williams, Thin Solid Films, *"The influence of target oxidation and growth related effects on the electrical properties of reactively sputtered films of tin-doped indium oxide"*, Thin Solid Films, Vol. 80, pp. 373–382, 1981.
- 49- M. Higuchi, S. Uekusa, R. Nakano and K. Yokogawa, *"Post-deposition annealing influence on sputtered indium tin oxide film characteristics"*, Japanese Journal of Applied Physics, Vol. 33, pp. 302–306, 1994.
- 50- N. Balasubramanian and A. Subrahmanyam, *"Effect of substrate temperature on the electrical and optical properties of reactively evaporated indium tin oxide films"*, Materials Science and Engineering, B1 pp. 279–281, 1988.
- 51- J. Bregman, Y. Shapira and H. Aharoni, *"Effects of oxygen partial pressure during deposition on the properties of ion-beam-sputtered indium-tin oxide thin films"*, Journal of Applied Physics, Vol. 67, pp. 3750–3753, 1990.
- 52- H. Haitjema and J. J. Ph. Elich, *"Physical properties of pyrolytically sprayed tin-doped indium oxide coatings"*, Thin Solid Films, Vol. 205, pp. 93–100, 1991.
- 53- C. C. Yap, M. Yahaya and M. M. Salleh, *"Influence of tetrabutylammonium hexafluorophosphate (TBAPF₆) doping level on the performance of organic light emitting diodes based on PVK: PBD blend films"*, Current Applied Physics, Vol. 9, pp. 722–726, 2009.
- 54- A. K. Narula, R. Singh, K. L. Yadav and K. B. Ravat, Subhas Chandra, *"Effect of synthesis temperature and doping level on conductivity and structure of poly(3-methyl thiophene)"*, Applied Biochemistry and Biotechnology, Vol. 96, pp. 109–117, 2001.
- 55- M. Glatthaar, N. Mingirulli, B. Zimmermann, T. Ziegler, R. Kern, M. Niggemann, A. Hinsch and A. Gombert, *"Impedance spectroscopy on organic bulk-heterojunction solar cells"*, Physica Status Solidi (A) Applications and Materials, pp. 202–125, 2005.
- 56- A. K. Pandey, J. M. Nunzi, H. Wang, C. C. Oey, A.B. Djuricic, M. H. Xie, Y. H. Leung, K. K. Y. Man and W. K. Chan, *"Reverse Biased Annealing: Effective post treatment tool for polymer/nano-compositesolar cells"*, Organic Electronics 8, pp. 396–400, 2007.

- 57- "COMSOL Multiphysics Modeling Guide (COMSOL 3.5a)", COMSOL AB, Burlington MA USA, November 2008.
- 58- "Reference Guide (COMSOL 3.5a)", COMSOL AB, Burlington, MA USA, November 2008.
- 59- E. Ahlswede, J. Hanisch, and M. Powalla, "*Influence of cathode sputter deposition on organic solar cells*", Applied Physics Letters, Vol. 90, No. 063513, 2007.
- 60- J. Hanisch, E. Ahlswede, M. Powalla, "*All-sputtered contacts for organic solar cells*", Thin Solid Films Vol. 516, pp. 7241–7244, 2008.
- 61- C. J. Schneider, N. Engelberts and J. D. P. van Dijk, "*Characteristics of a passive RF field probe with fibre-optic link for measurements in liquid hyperthermia phantoms*", Physics in Medicine and Biology, Vol. 36, pp. 46-474, 1991.
- 62- M. Martin, J.-J. André, and J. Simon, "*Influence of dioxygen on the junction properties of metallophthalocyanine based devices*", Journal of Applied Physics, Vol. 54, pp. 2792, 1983.
- 63- M. Whalley, "*Absorption spectra of tetrazaporphins and phthalocyanines. Formation of pyridine salts*", Conjugated macrocycles. Part XXXII. Journal of the Chemical Society, Vol. 1, pp. 866-869, 1961.
- 64- R. Koeppe and N. Serdar Sariciftci, "*Complexation of pyrrolidinofullerenes and zinc-phthalocyanine in a bilayer organic solar cell structure*", Applied Physics Letters, Vol. 87, No. 244102, 2005.
- 65- A. Gehring and S. Selberherr, "*Modeling of tunneling current and gate dielectric reliability for nonvolatile memory devices*", IEEE Trans. On Device & Materials Reliability, Vol. 4, Issue 3, 2004.
- 66- S. M. Sze, "*Physics of Semiconductor Devices*", 2nd Edition, John Wiley & Sons, Inc. 1981.
- 67- K. F. Schuegraf, C. C. King, and C. Hu, "*Ultrathin silicon dioxide leakage current and scaling limit*", Symp. VLSI Technol. Tech. Dig., pp. 18–19, 1992.
- 68- A. B. Walker, A. Kambili and S. J. Martin, "*Modelling temperature-dependent current voltage characteristics of an MEH-PPV organic light emitting device*", Journal of Physics: Condensed Matter, Vol. 14, pp. 9825–9876, 2002.